Multimaterial Acoustic Fibers

by

Noémie Chocat

B.Sc., Mathematics and Physics
École Polytechnique, France, 2006

M.Sc., Physics
École Polytechnique, France, 2007
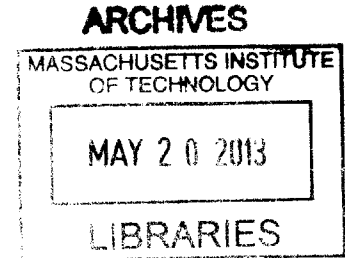
Submitted to the Department of Materials Science and Engineering
in partial fulfillment of the requirements for the degree of

Doctor of Philosophy in Materials Science and Engineering

at the

MASSACHUSETTS INSTITUTE OF TECHNOLOGY

September 2012

© Massachusetts Institute of Technology 2012. All rights reserved.

Author...
Department of Materials Science and Engineering
August 31, 2012

Certified by...
Yoel Fink
Professor of Materials Science
Professor of Electrical Engineering and Computer Science
Thesis Supervisor

Accepted by...
Gerbrand Ceder
Chairman, Departmental Committee on Graduate Students

Multimaterial Acoustic Fibers

by

Noémie Chocat

Abstract

The emergence of multimaterial fibers that combine a multiplicity of solid materials with disparate electrical, optical, and mechanical properties into a single fiber presents new opportunities for extending fiber applications well beyond optical transmission. Fiber reflectors, thermal detectors, photodetectors, chemical sensors, surface-emitting fiber lasers, fiber diodes, and other functional fiber devices have been demonstrated with this approach. Yet, throughout this development and indeed the development of fibers in general, a key premise has remained unchanged : that fibers are essentially static devices incapable of controllably changing their properties at high frequencies. Unique opportunities would arise if a rapid, electrically-driven mechanism for changing fiber properties existed. A wide spectrum of hitherto passive fiber devices could at once become active with applications spanning electronics, mechanics, acoustics, and optics, with the benefits of large surface-area, structural robustness, and mechanical flexibility. This thesis addresses the challenges and opportunities associated with the realization of electromechanical transduction in fibers through the integration of internal piezoelectric and electrostrictive domains. The fundamental challenges related to the fabrication of piezoelectric devices in fiber form are analyzed from a materials perspective, and candidate materials and geometries are selected that are compatible with the thermal drawing process. The first realization of a thermally drawn piezoelectric fiber device is reported and its piezoelectric response is established over a wide range of frequencies. The acoustic properties of piezoelectric fiber devices are characterized and related to their mechanical and geometric properties. Collective effects in multi-fiber constructs are discussed and demonstrated by the realization of a linear phased array of piezoelectric fibers capable of acoustic beam steering. High strain actuation capabilities in a

3

fiber are demonstrated based on the integration of a highly electrostrictive relaxor ferroelectric polymer. The potential of this approach to realize integrated micro-electromechanical systems in fibers is illustrated by the fabrication of a hybrid fiber comprising an electrostrictive device and an adjacent Fabry-Perot optical filter. Amplitude modulation of the light reflected from the Fabry-Perot cavity is demonstrated through electric field induced tuning of the cavity resonance.

Thesis Supervisor: Yoel Fink
Title: Professor of Materials Science
Professor of Electrical Engineering and Computer Science

Acknowledgments

This thesis would not have been possible without the help, support, and friendship of many people. First and foremost, I would like to express my immense gratitude to Professor Yoel Fink, to whom I owe this PhD. His vision and contagious enthusiasm have inspired me to do research in the emerging field of functional fibers. His profound knowledge and rigorous thinking have deeply influenced me as a scientist; equally formative was his rare ability to motivate and guide people. He has been an exceptional advisor throughout my time at MIT and will always be a mentor. I also thank my thesis committee members, Professor John Joannopoulos and Professor Michael Cima, for their availability, enthusiasm, and guidance on my work.

During my PhD I was fortunate to be surrounded by many talented people who contributed to the acoustic fiber project. I am indebted to Dr. Zheng Wang, who taught me many valuable skills in the lab and has played an inestimable role in the piezo fiber project. I would also like to thank Dr. Shunji Egusa, who introduced me to the project and gave me the opportunity to hone my communication and team working skills. It has been a total pleasure to work alongside Guillaume Lestoquoy, who has been both a terrific colleague and a friend. I am also grateful to Dr. Ofer Shapira who helped me with all things optics. Thanks to all the Fink group members for cultivating a friendly and collaborative atmosphere in the research group and for many fruitful discussions: Fabien, Sasha, Lei, Chong, Zach, Benjamin, Dana, Daosheng, Nick, Xiaoting, Alexander.

For helping me maintain a healthy balance in my life, I thank my friends both in Cambridge and in France. Thanks especially to Tiffany, Deborah, Jungmin, Yann, Stephanie, Adrien, Evelyne, and Vincent, with whom I shared many memorable moments around a cup of tea, a good meal, or a movie.

I am infinitely indebted to my parents, who have taught me the joy of learning and to whom I owe my presence at MIT. I am thankful to all my family for being a constant source of support, especially to my brother Eric and my grandmother.

I gained more than a PhD in Cambridge. To Arthur, my partner and best friend, whose daily encouragements, unmatched sense of humor, patience, and love were precious helps during this journey.

Contents

9

List of Figures

13

Chapter 1

Introduction

Recent archeological discoveries indicate that over 30,000 years ago, in the caves of the Caucasus mountains, paleolithic hunter-gatherers used wild flax fibers to make cords, weave baskets, and sew garments [1]. Far from being anecdotal, this fact illustrates the intimate role that fibers have played in the history of mankind since prehistoric times. From the development of global trade along the ancient Silk Road to the birth of the Industrial Revolution in 18$^{\text{th}}$ century British cotton spinning mills, fibers have been instrumental in key technological and economic revolutions, the most recent being the information revolution enabled by fiber-optic communications. Parallel to these changes, fiber materials have evolved from natural fibers extracted from mineral, plant, and animal sources, to synthetic fibers made of polymers or high-purity silica glass.

In the past decade, a new family of fibers, called *microstructured fibers*, has emerged

that vastly expands the range of fiber materials, geometries, and applications. One example of such microstructured fibers are *photonic crystal fibers* [2, 3], which comprise a periodic array of microscopic air holes in a silica or polymer matrix (figure 1-1b). Because of their ability to control and guide light in ways not obtainable using conventional step-index fibers, photonic crystal fibers have generated great scientific interest and have been commercialized for applications such as high-power laser transmission and supercontinuum sources.

(a)   (b)   (c)
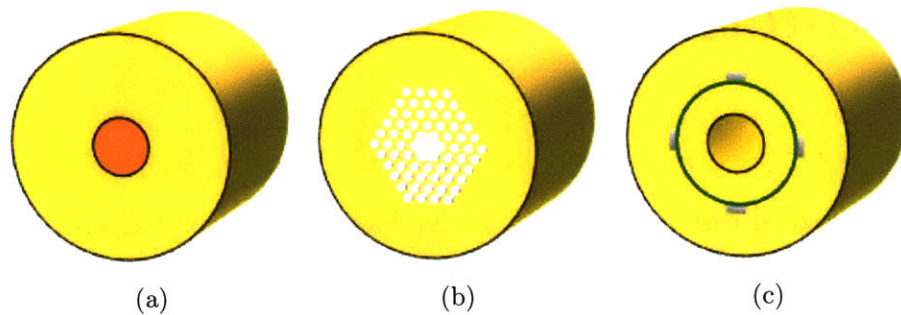
Figure 1-1: a) standard step-index silica glass optical fiber, with a high-refractive index core (orange) most commonly made of doped silica and a low-refractive index silica cladding (yellow). b) photonic crystal fiber, with a two-dimensionally periodic triangular lattice of air holes surrounding the core area. c) multimaterial fiber, with an amorphous semiconductor thin film (green) contacted by four metallic electrodes and surrounded by an insulating polymer cladding (yellow).

A different approach has been to create multimaterial composite fibers that combine a multiplicity of solid materials with disparate optical, electrical, and mechanical properties into a single fiber (figure 1-1c) [4]. Fiber reflectors, thermal detectors, photodetectors, chemical sensors, surface-emitting fiber lasers, fiber diodes, and other functional fiber devices have been demonstrated with this approach [5–11]. These kilometer-long thin fibers can in turn be assembled into flexible grids and fabrics

covering large surface areas, thus bringing the prospect of truly multifunctional fabrics [12, 13].

Yet despite these technological advances, a key premise has remained constant: fibers are essentially static devices, incapable of controllably changing their properties over a wide range of frequencies. This thesis addresses this issue through the integration of electric-field actuated electroactive polymers, specifically piezoelectric and electrostrictive polymers, in multimaterial fibers. These structures impart acoustic and electromechanical functionalities to fibers and provide new opportunities for the realization of electrically actuated fiber devices capable of high frequency operation. These results are expected to have a significant impact on fields such as acoustics, acousto-optics, microelectromechanical systems (MEMS), sensing technologies, and large-area flexible systems.

This thesis is organized as follows. In Chapter 2, we start by laying the general background for this work. We describe the new material processing paradigm underlying the field of multimaterial fibers, its tremendous possibilities as well as the constraints that it imposes on the choice of compatible materials. We also recapitulate the different physical mechanisms of electromechanical transduction and provide a brief theoretical background on piezoelectricity and electrostriction. In Chapter 3, we present the first multimaterial piezoelectric fiber. We expose the fundamental challenges related to the fabrication of a piezoelectric device in fiber form and explain how we have been able to select appropriate materials to overcome these challenges.

Chapter 4 focuses on a careful characterization of the piezoelectric fibers as acoustic wave sensors and emitters. We highlight some of the unique properties of the fiber fabrication process, and describe acoustic wave shaping applications enabled by the flexibility and versatile geometry of fiber devices. This study will also lead us to identify the limitations of piezoelectric fiber devices and consider how we can improve their performance by imagining new materials or fiber architectures. One of the attributes of fibers is their ease of assembly in multi-fiber constructs such as grids and fabrics. Chapter 5 presents the collective effects that emerge from multiple fiber assemblies and demonstrates acoustic beam steering using linear phased arrays of piezoelectric fibers. In Chapter 6, we demonstrate high strain actuation capabilities in a fiber based on the integration of a highly electrostrictive relaxor ferroelectric polymer. The potential of this approach to realize integrated microelectromechanical systems in fibers is illustrated by the fabrication of a hybrid electrostrictive Fabry-Perot fiber and its use for optical amplitude modulation. We conclude by outlining future research directions in Chapter 7.

Chapter 2

Background

2.1   Multimaterial functional fibers

The process of fiber drawing from a solid structured preform that is heated and deformed in the viscous state has been well established through the development of the fiber-optic telecommunications industry. It enables the rapid fabrication of kilometer-scale continuous lengths of fiber with precise dimensional tolerances and at low cost. Over the past decade, the Photonic Bandgap Fibers and Devices group at MIT has devised a method that extends the thermal drawing process beyond silica optical transmission fibers to polymer composite fibers combining multiple materials in arbitrary geometries [4]. This approach has led to the emergence of a new class of fibers with unique and unconventional functionalities. In this section, we first present the multimaterial fiber fabrication process. We then discuss the selection criteria for materials compatible with this approach and the range of materials that

19

have already been successfully incorporated in fibers, as well as the resulting fiber devices. Finally, we highlight two integration capabilities at the intra- and inter-fiber levels as paths to achieving higher level functionalities.

2.1.1   Fabrication process

The first step of our method is the fabrication of a multimaterial cylindrical object called a *preform*, which is identical in its geometry and composition to the final fiber, but is much larger in its cross-sectional dimensions and shorter in length (figure 2-1).

(a)   (b)   (c)
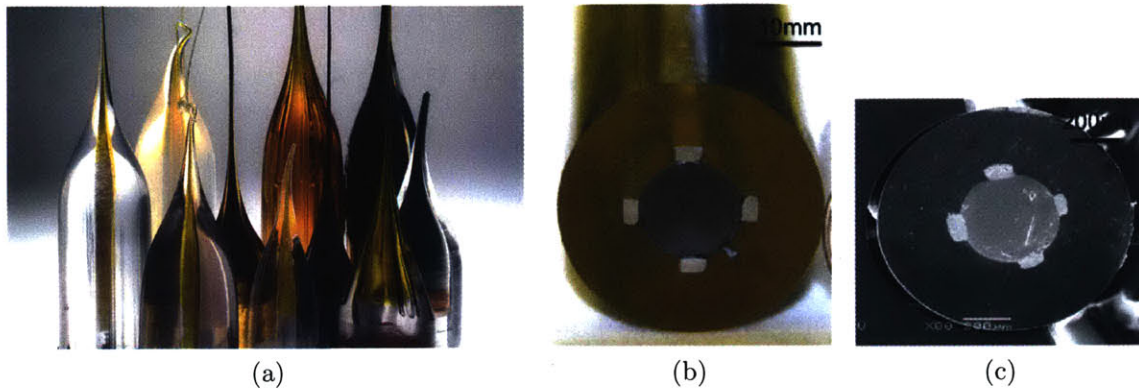
Figure 2-1: a) Photograph of preforms featuring the neck-down region character-istic of the draw process (courtesy of Greg Hren). b) Cross-section of a metal-semiconductor-insulator preform. c) Cross-section of the corresponding fiber featur-ing the same materials and geometry as the original preform (courtesy of Fabien Sorin).

Typical dimensions for a preform are $\sim$ 30 to 40 mm in diameter and $\sim$ 20 to 30 cm in length. The different materials composing the preform are assembled into a pre-cise geometry using various machining techniques such as milling, lathing, pressing,

20

thermal evaporation, etc. The preform is then consolidated in a vacuum oven at high temperature to remove trapped gas, fuse the different layers, and form high-quality interfaces. The resulting fiber preform is thermally drawn into extended lengths of fiber using a draw tower procedure.

Figure 2-2a shows a schematic of a fiber draw tower. The preform is attached to a holder and slowly fed into a three-zone furnace. There, it is slowly heated until it reaches a viscous fluid state and necks down under the effect of gravity. The preform is then continuously pulled into a fiber by a capstan. During this process, the internal and external geometry of the preform are maintained, while its cross-sectional dimensions are reduced by a factor of ~ 20 to 100 and its length is increased, resulting in hundreds of meters of fiber. By conservation of volume, the draw-down ratio r is related to the capstan speed $v_{capstan}$ and the downfeed speed $v_{downfeed}$ in the following way:

$$r = \sqrt{\frac{v_{capstan}}{v_{downfeed}}} \tag{2.1}$$

Typical numbers are $v_{capstan} = 1$ m.min^{-1}, $v_{downfeed} = 1$ mm.min^{-1}, and $r \approx 30$. The stability of the draw is monitored by a continuous in-line measurement of the external dimensions of the fiber by a laser micrometer, while a tensiometer enables real-time monitoring of the draw stress. The standard deviation is calculated over a 10 cm window in real-time and maintained at a level below 1% by controlling the draw stress through adjustments in the furnace temperature and capstan speed.

21
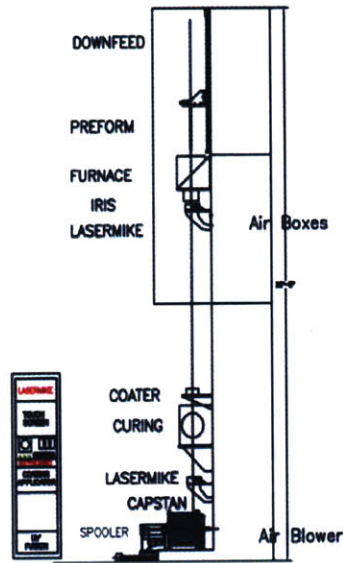
(a)

(b)
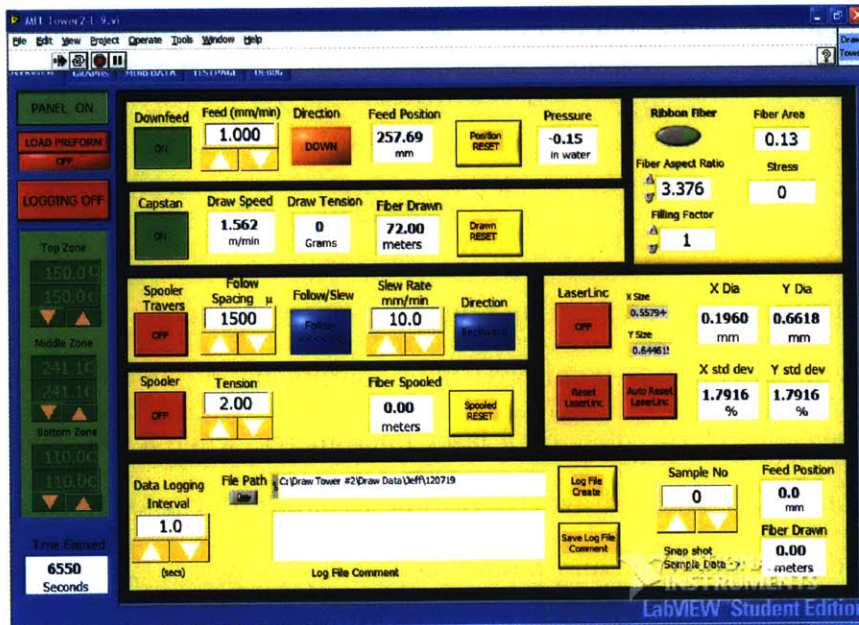
(c)

Figure 2-2: a) Schematic and b) photograph of a draw tower. c) Screenshot of the LabView fiber draw control panel.

2.1.2 Materials selection

Key to the draw process is the identification of a set of materials that can be co-drawn and are capable of maintaining the preform geometry in the fiber by preventing axial and cross-sectional capillary break-up. To achieve this objective, viscous forces are commonly used to oppose the interface-energy-driven capillary break-up mechanisms. The following general conditions are needed in the materials used in this process [4]:

1. At least one of the fiber materials needs to support the draw stress and yet continuously and controllably deform; thus at least one component should be amorphous in nature, and resist devitrification, allowing for fiber drawing at reasonable speeds in a furnace-tower process with self-maintaining structural regularity.

2. All the materials must flow (viscosity $< 10^7$ Pa.s) at a common temperature; if a crystalline material is incorporated it should have a melting temperature below the draw temperature.

3. The materials should exhibit good adhesion/wetting in the viscous and solid states without cracking even when subjected to thermal quenching. It is generally understood that the degree of intimate contact between the two surfaces at the molecular scale is a crucial factor in increasing the short-range Van der Waals interactions that promote solid-state adhesion. Thus, it is advantageous that both materials will be processed at a temperature where they are both quasi-molten so that this molecular surface interpenetration may be enhanced.

Over the years, a set of materials have been identified that fit these criteria and can be successfully co-drawn. High glass-transition temperature thermoplastics are used as the main supporting material (cladding material) because of their variety, availability in bulk and film form, and excellent thermo-mechanical properties. Several thermoplastic polymers have been shown to be suitable for draw temperatures between 200°C and 300°C, including polyether sulfone (PES), polysulfone (PSU), polycarbonate (PC), cyclic olefin copolymers (COC), and polyetherimide (PEI).

The achievement of different functionalities in fibers directly depends on the ability to incorporate materials with distinct properties in a precise geometry. By combining materials with different optical properties, for example a low refractive index thermoplastic with a high refractive index chalcogenide glass, we can create optical devices such as photonic bandgap fibers and fiber reflectors [5, 6]. Combining materials with disparate electrical properties like metals, amorphous semiconductors, and insulators opens the way for the realization of electronic and optoelectronic functionalities in fibers, for example photodetection and thermal detection [7, 8]. Adding crystalline semiconductors enables the fabrication of more sophisticated electronic fiber devices such as field-effect transistors and memory devices [10, 14]. By introducing fluids in fibers, further functionalities are made possible, such as radially-emitting fiber lasers [9] and laser modulators based on liquid crystals [11]. Therefore, in order to impart acoustic and electromechanical functionalities to fibers, one of the keys is to identify new materials that can be incorporated to our palette.
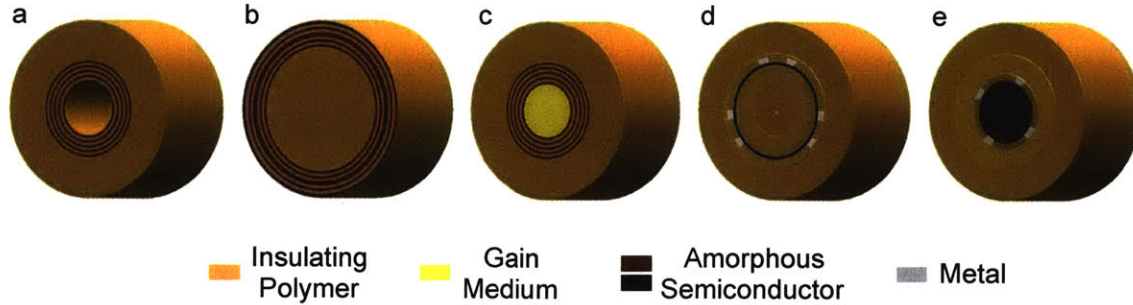
Figure 2-3: Schematics of multimaterial fibers with different functionalities. a) Photonic bandgap fiber for high power laser transmission. b) Fiber reflector. c) Radially emitting fiber laser. d) Thermal detector. e) Photodetecting fiber.

2.1.3 Fiber integration

A challenge in developing more sophisticated functional fibers has been the integration of multiple functional elements into a single fiber cross-section. This is in fact a common problem in nanotechnology where the drive towards smaller and smaller nanoscale devices complicates the ability to integrate and individually address many of them, especially over large-area coverage. Integration of multiple devices to work collectively is however the key to the delivery of complex functionality. Multimaterial fibers have been shown to be able to overcome this challenge by integration both at the intra-fiber and inter-fiber levels. At the intra-fiber level, multiple devices can be incorporated into a single fiber, resulting in integrated fiber devices with higher functionalities. This is demonstrated by work on optoelectronic fibers for optical detection: while a fiber containing a single photodetecting structure can sense the presence or absence of light, fibers integrating up to eight independent optical detectors can retrieve increasing amounts of information about an incoming radiation, such as its direction and wavelength [13]. Other examples of integrated fiber devices

25

include self-monitoring high-power optical transmission fibers combining an optical, electrical, and thermal element inside a single fiber [15], and surface fiber lasers with integrated liquid crystal channels dynamically controlling the direction of emission [11]. Another geometric degree of freedom is at the inter-fiber level, through the incorporation of multiple fibers into arrays. As the fibers are flexible and light-weight, they can be incorporated into pre-existing structures such as fabrics, and because they are produced uniformly in long lengths, arrays made from fibers may extend over large areas [12]. The interaction of multiple fibers may introduce functionalities not inherent in the single fibers, as was shown with the demonstration of lensless imaging using a grid of photodetecting fibers [13].

2.2 Electromechanical transduction mechanisms

There exists a large variety of mechanisms that induce or sense strain in a material. These mechanisms often couple the mechanical energy related to the strain change with another type of energy, and are therefore named transduction mechanisms. A common example is thermoelastic transduction, i.e. coupling between a strain change and a temperature change of the material. Most materials undergo a change in volume in response to a change in temperature; this effect is called thermal expansion and is used for example in thermometers. A more advanced form of thermoelastic transduction is shape-memory alloys, which undergo large deformations when heated above a specific temperature related to a phase transformation.

26

Electromechanical transduction mechanisms are a subset of these transduction mechanisms that specifically couple mechanical energy with electrical energy. They present two main advantages over other transduction mechanisms such as thermoelastic, magnetoelastic, and chemomechanical transduction. The first is their large bandwidth. Thermal and chemical mechanisms typically have long time constants and are not suited for operating frequencies above a few Hz. Electromechanical mechanisms, on the other hand, are routinely used for kHz and MHz applications, and can even be operated in the GHz range for certain piezoelectrics. The second advantage is that since they are electrically driven, they can easily be integrated with the operating electronics.

The electromechanical properties of a solid may be defined using the elastic Gibbs function G for the free energy of a material. In differential form, G can be written as

$$\mathrm{d}G = -S\,\mathrm{d}T - \mathbf{x}_{ij}\,\mathrm{d}\mathbf{X}_{ij} + \mathbf{E}_i\,\mathrm{d}\mathbf{P}_i \tag{2.2}$$

where S is the entropy, T the temperature, $\mathbf{x}_{ij}$ the strain tensor, $\mathbf{X}_{ij}$ the stress tensor, $\mathbf{E}_i$ the electric field, and $\mathbf{P}_i$ the polarization. By differentiating the elastic Gibbs function with respect to stress, one obtains the tensor properties associated with effects that introduce strain in the material, such as elasticity, thermal expansion, piezoelectricity, and electrostriction [16]. At constant stress and temperature, the strain can be expressed as a power series of the polarization:

$$\mathbf{x}_{ij} = \mathbf{g}_{ijm}\mathbf{P}_m + \mathbf{Q}_{ijmn}\mathbf{P}_m\mathbf{P}_n + \dots \tag{2.3}$$

27

with

$$g_{ijm} = \left(\frac{\partial^2 G}{\partial \mathbf{X}_{ij} \partial \mathbf{P}_m} \right)_{\mathbf{X},T} \tag{2.4}$$

and

$$\mathbf{Q}_{ijmn} = \left(\frac{\partial^3 G}{\partial \mathbf{X}_{ij} \partial \mathbf{P}_m \partial \mathbf{P}_n} \right)_{\mathbf{X},T} \tag{2.5}$$

The linear coefficient g_{ijm} is a third-rank tensor and is related to the piezoelectric effect, while the quadratic coefficient $\mathbf{Q}_{ijmn}$ is a fourth-rank tensor related to the electrostriction effect. The following sections describe these two effects in more detail.

2.2.1 Piezoelectricity

Theory of piezoelectricity

Piezoelectricity is described by a linear relationship between strain and polarization and can be separated into a direct and an indirect (or reverse) effect. The direct effect refers to the generation of an electrical polarization in a material under the action of a mechanical force. The indirect effect refers to the mechanical deformation of a material when an electric field is applied.

The discovery of the direct effect by Pierre and Jacques Curie in 1880 followed directly from the application of principles relating to the symmetry of causes and effects [17]. Curie's symmetry principle can be stated as follows :

A phenomenon can exist only in a system having a symmetry which

is a sub-group of the characteristic symmetry of the phenomenon

28

A consequence of this principle is that a homogeneous distortion of a centrosymmetric structure cannot result in an electrical polarization. Therefore, centrosymmetric crystals cannot be piezoelectric and piezoelectricity is only found in 20 crystal classes, these being the 21 non-centrosymmetric classes with the special case of class 432 excluded.

The direct and indirect piezoelectric couplings can be described by the following system of equations relating strain, stress, polarization, and electric field [18]:

$$\mathbf{E}_i = \boldsymbol{\beta}_{ij}\mathbf{P}_j - \mathbf{g}_{ijk}\mathbf{X}_{jk} \tag{2.6a}$$

$$\mathbf{x}_{jk} = \mathbf{s}_{jklm}\mathbf{X}_{lm} + \mathbf{g}_{ijk}\mathbf{P}_i \tag{2.6b}$$

These give the mechanical strain $\mathbf{x}_{ij}$ and electric field $\mathbf{E}_i$, in terms of the independent variables electrical polarization $\mathbf{P}_i$ and stress $\mathbf{X}_{ij}$. $\mathbf{s}_{jklm}$ is the compliance tensor and $\boldsymbol{\beta}_{ij}$ is the reciprocal of the permittivity $\boldsymbol{\epsilon}_{ij}$. $\mathbf{g}_{ijk}$ is called the *piezoelectric voltage constant*. Because it represents the electric field generated by a piezoelectric material per unit of applied mechanical stress, $\mathbf{g}_{ijk}$ is important for assessing a material's suitability for sensing applications. It is in units of (V.m)/N.

These equations of state are also commonly expressed as a function of independent variables stress and electric field. Using the matrix notation convention[1], this

---

[1]In the matrix notation, ij or kl in tensor form is replaced by α or β according to : 11→1, 22→2, 33→3, 23 or 32→4, 13 or 31→5, 12 or 21→6 [19]

29

gives:

$$\mathbf{x}_\alpha = \mathbf{s}_{\alpha\beta}\mathbf{X}_\beta + \mathbf{d}_{i\alpha}\mathbf{E}_i \qquad (2.7a)$$

$$\mathbf{P}_i = \epsilon_{ij}\mathbf{E}_j + \mathbf{d}_{i\alpha}\mathbf{X}_\alpha \qquad (2.7b)$$

The moduli $\mathbf{d}_{i\alpha}$ express the proportionality relation between the strain and the electric field components and are termed *piezoelectric strain constants*. Because they give the mechanical displacement when a voltage is applied between two electrodes, they are important in assessing a material's suitability for actuator applications. They are on the order of 10^{-12} m.V^{-1} (or, equivalently, 10^{-12} C.N^{-1}).

To measure the capability of a piezoelectric material to convert energy between the mechanical and electrical forms, one uses the *electromechanical coupling factor* k defined as :

$$k^2 = \frac{\text{converted mechanical energy}}{\text{input electric energy}} \qquad (2.8)$$

For a piezoelectric effect with electric field along direction i and associated strain along direction j, the coupling factor is :

$$k_{ij}^2 = \frac{\mathbf{d}_{ij}^2}{\epsilon_{ii}\mathbf{s}_{jj}} \qquad (2.9)$$

Coupling factors range from 0.1 - 0.3 for piezopolymers, to up to 0.8 for certain piezoceramic transducers.

30

Of the 20 non-centrosymmetric crystal classes that allow piezoelectricity, 10 have a unique polar axis responsible for the appearance of a permanent spontaneous electrical polarization and are termed *pyroelectric*. If this polarization can be reversed by the application of an electric field, the material is *ferroelectric*. Above a certain temperature T_C, termed the Curie point, the spontaneous polarization vanishes, and the ferroelectric material transforms into a paraelectric state. Many ferroelectrics lose their piezoelectric properties above T_C completely, because their paraelectric phase has centrosymmetric crystallographic structure. One advantage of ferroelectrics is that they have much higher piezoelectric activity than non-ferroelectric piezoelectrics, especially in the vicinity of the Curie point. For instance, for ceramics, d is 10^0-10^1 pC.N^{-1} for nonferroelectric piezoelectrics and 10^2-10^3 pC.N^{-1} for ferroelectrics; for polymers, d is 10^{-1}-10^0 pC.N^{-1} for nonferroelectric piezoelectrics and 10^0-10^1 pC.N^{-1} for ferroelectrics [20].

Applications of piezoelectricity

Piezoelectricity now has a wide range of technical applications, especially in the fields of information and communication, industrial automation, medical diagnostics, automation and traffic control, and in the defense industries. Piezoelectrics can sense and generate very small strains, and are therefore particularly useful in applications where a high degree of precision or sensitivity is required. Common examples include micro-positioning actuators for atomic force microscopes (AFM), scanning tunneling microscopes (STM), and laser mirror alignment; guided wave sensors; and quartz

31

resonator sensors that detect pressure, chemical effects, acceleration, or changes in temperature. Because of their large bandwidth, piezoelectric materials are also used as ultrasonic transducers for medical purposes and for industrial nondestructive testing (NDT), and acousto-optic components (acousto-optic modulators (AOM), deflectors, variable delay lines, spectrum analyzers and tunable optical filters). The main disadvantages of piezoelectrics are the limited set of available materials due to the symmetry requirements, the necessity of initial poling and high operating voltages, a large hysteresis, and creep.

2.2.2 Electrostriction

Electrostriction relates the quadratic dependence of strain on induced polarization and is described by the following equation:

$$\mathbf{x}_{ij} = \mathbf{Q}_{ijmn}\mathbf{P}_m\mathbf{P}_n \tag{2.10}$$

where $\mathbf{Q}_{ijmn}$ is the fourth-rank *polarization-related electrostriction tensor*. For linear dielectric materials, polarization is proportional to and aligned with the electric field:

$$\mathbf{P} = \epsilon_0\chi\mathbf{E} \tag{2.11}$$

where ϵ_0 is the vacuum permittivity and χ the electric susceptibility of the medium. Therefore, for these materials, electrostriction can also be defined as a quadratic

coupling between strain and electric field strength:

$$\mathbf{x}_{ij} = \mathbf{M}_{ijmn}\mathbf{E}_m\mathbf{E}_n \tag{2.12}$$

where $\mathbf{M}_{ijmn}$ is the fourth-rank *field-related electrostriction tensor*. However, some materials such as polycrystalline ferroelectrics exhibit large nonlinearities between polarization and electric field, due to domain-orientation processes. Therefore, electrostrictive strain is not always quadratic with applied electric field and is better defined in the general case using equation 2.10. The $\mathbf{Q}_{ijmn}$ coefficients are in units of $m^4.C^{-2}$ and range from 10^{-3} $m^4.C^{-2}$ in relaxor ferroelectrics to greater than 1 $m^4.C^{-2}$ in polymers. Because electrostrictive strain is quadratically related to polarization, it is also quadratically related to the dielectric constant of the material $\epsilon_r = 1 + \chi$. Therefore, materials with a high dielectric constant can exhibit relatively large strains even with a small $\mathbf{Q}_{ijmn}$ coefficient.

Unlike piezoelectricity, which is only present in non-centrosymmetric materials, electrostriction is a property of all dielectric materials. When an electric field is applied on a crystal structure, the anions and cations are displaced in opposite directions and attract each other, resulting in a contraction in the direction of the applied electric field. The reverse effect in which an electrical polarization would be produced under applied stress is impossible in centrosymmetric materials for symmetry reasons explained in section 2.2.1. This difference between applied electric field and stress results from the fact that applied electric field acts on charge points, while stress acts on mass points [21]. However, two other thermodynamically related effects have been

33

identified [22]: the first converse effect, which refers to the variation of reciprocal dielectric susceptibility with applied stress, and the second converse effect, which is the polarization dependence of the piezoelectric voltage constant g_{ijk}. Two other differences differentiate the quadratic electrostrictive effect from the linear piezoelectric effect: 1) the sign of electrostrictive strain is independent of the sign of the electric field, and 2) electrostriction occurs at double the frequency of the applied electric field.

Electrostrictive materials are sometimes used under a DC biasing field. The application of a biasing field produces an asymmetrical atomic arrangement, and this in turn will produce a linear distortion by subsequent fields [21]. Therefore, if a large DC field and a small AC field are applied to an electrostrictive material, it will behave as a piezoelectric material under an AC field. One advantage of using electric-field induced piezoelectricity in electrostrictive materials is the capability of adjusting the electromechanical coefficients by changing the biasing field.

While electrostriction was long considered a higher-order nonlinear effect requiring stronger fields in most materials than typical fields used in piezoelectric materials, the emergence of a new class of highly electrostrictive materials, known as relaxor ferroelectrics, has opened the way for the use of electrostriction as an alternative to piezoelectricity for large-strain actuation applications [23]. The study of relaxor ferroelectrics originated from work on perovskite structure electroceramics and has experienced an explosive growth of interest with the discovery of large, stable elec-

trostrictive strains in lead magnesium niobate (PMN) [24]. In addition to strain capabilities of several percent, a major advantage of electrostriction over ferroelectric mechanisms is that it enables a reproducible, non-hysteretic response, with high temperature stability and absence of aging [23]. This is particularly important for high-precision positioning devices. Furthermore, electrostrictors do not require high-field electrical poling, unlike ferroelectric piezoelectrics, and are more stable over time. Electrostrictive materials are now used in stacked actuator devices, oil pressure servovalves, active optical systems (bistable optical devices, interferometric dilatometers, and deformable mirrors), vibration-suppression systems, artificial muscles, and energy harvesting devices. Field-induced piezoelectric properties of electrostrictive materials have also been explored for ultrasonic medical imaging [25].

Chapter 3

Piezoelectric fiber fabrication

3.1 Is it possible to draw a piezoelectric material?

3.1.1 The challenge: non-centrosymmetry

One of the main requirements for fiber drawing is that the materials should be amorphous in nature, as well as glassy, i.e. not easily crystallized at high processing temperatures. The reason for this can be understood in terms of the fundamental properties of the glassy state. The atomic structure of an amorphous material can be described as a continuous random network, where the local environment of an atom is well-defined but there is no repeating unit cell or crystalline order. Therefore the viscosity of a glassy material varies quasi-continuously between the solid and liquid states, in contrast to a crystalline material, which experiences a first-order thermodynamic phase transformation at the melting temperature T_M, with associated discontinuous changes in volume, configurational entropy, and viscosity upon cooling

37

or heating through T_M (figure 3-1).
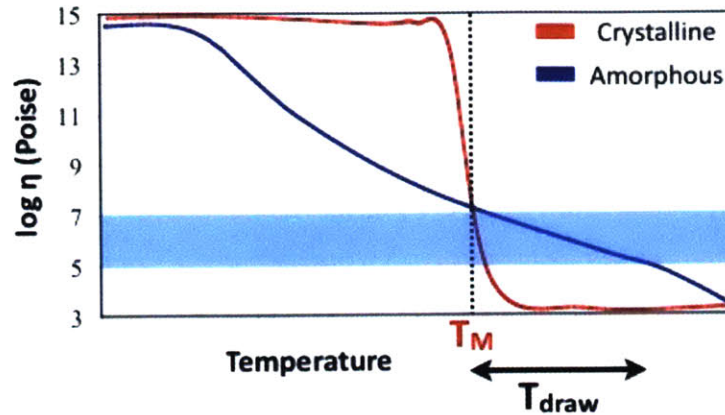
Figure 3-1: Viscosities of crystalline and amorphous materials

Thus, in general, materials should be glassy in order to be drawn at reasonable speeds in a furnace-tower process with self-maintaining structural regularity. Furthermore, they must not simply be amorphous when deposited or made into a preform, but must remain amorphous when cycled through their softening and drawing temperatures. This requirement makes it in principle impossible to draw a piezoelectric material, since piezoelectricity can only be present in non-centrosymmetric phases, which cannot be amorphous. It has been shown previously, however, that crystalline phases such as metals can be incorporated in fibers if two conditions are met: first, their melting temperature should be below the draw temperature, and second, they must be confined within viscous boundaries [7]. The challenge then is to identify a piezoelectric material that fulfills these criteria.

38

3.1.2 Piezoelectric material selection: P(VDF-TrFE)

The most commonly used piezoelectric materials today are perovskite ceramics, such as barium titanate ($BaTiO_3$), lead titanate ($PbTiO_3$), and lead zirconate titanate ($Pb(Zr_xTi_{1-x})O_3$, or PZT). Other common piezoceramics include lead scandium tantalate ($Pb(Sc_xTa_{1-x})O_3$, abbreviated PST) and barium strontium titanate ($Ba_xSr_{1-x}TiO_3$, abbreviated BST). However, these piezoceramics all have melting temperatures above $1000\,^{\circ}C$, making them unsuited for codrawing with thermoplastics.

The discovery of a strong piezoelectric effect in polymers, significantly large to be of interest for technical applications, dates back to the pioneering work of Kawai on poly(vinylidene fluoride) (PVDF) in 1969 [26], followed by the finding of pyroelectricity in the same polymer two years later by Bergman et al. [27] and Nakamura and Wada [28]. Later on, ferroelectricity was unambiguously confirmed in the PVDF polymer family [29]. Since then, the science and technology of piezoelectric polymers has been dominated by polymers from the PVDF family, especially the copolymers of vinylidene fluoride and trifluoroethylene P(VDF-TrFE). This material presents multiple advantages. It is mechanically flexible and inexpensive. Its nearly perfect impedance match with water and wide operating bandwidth makes it an excellent material for use in hydrophones and medical devices. PVDF-based piezopolymers have also been used in pressure sensors and shock wave sensors. The flexibility and the ease of production in any kind of form also allow for unusually shaped piezoelectric elements, such as piezoelectric cables for applications in traffic counting, physical

39

security, proximity sensing, and transducers for security fences. Lesser-known applications include tactile devices, energy conversion, porous polymers, and infra-red sensors [30]. The disadvantages of PVDF are that it has a low transmitting constant, its dielectric loss is large, and its dielectric constant is lower than piezoceramics (Table 3.1). Other classes of piezoelectric polymers include relaxor ferroelectric polymers and cellular polymer electrets. Relaxor ferroelectric polymers are based on electron-irradiated P(VDF-TrFE) copolymers or on terpolymers of vinylidene fluoride and trifluoroethylene with a third bulky monomer such as chlorofluoroethylene, and exhibit strong electrostriction and thus large piezoelectric coefficients when used under electric DC-bias fields. The piezoelectric behavior of ferroelectrets is not of inherent dipolar origin but results from injection of charges [31].

Property	Units	PZT	BaTiO$_3$	Quartz (SiO$_2$)	PVDF
Density	kg/m^3	7500	5700	2650	1780
Relative permittivity	ϵ/ϵ_0	1200	1700	4.5	12
d_{31}	10^{-12}C/N	110	78	2.3	23
k_{31}	at 1 kHz	0.30	0.21	0.14	0.12
Young's modulus	GPa	60	110	70	3
Acoustic impedance	10^6kg/m^{2}s	30	30	13	2.7
Curie temperature	°C	190	120	573	100

Table 3.1: Properties of different piezoelectric materials [32]

The ferroelectricity in PVDF arises from its particular structure at the molecular, crystalline, and morphological scales [29]. To be ferroelectric, a polymer must have the following characteristics:

1. The repeating unit of the polymer chain should be strongly polar so that a large

40

permanent dipole moment is associated with the unit. In PVDF the repeating unit is $-CH_2 - CF_2-$, which has a net dipole moment of about 2 Debye, due to the highly polar bonds between electronegative fluorine and carbon.

2. The conformation of the polymer chain should enhance the dipole moment of repeating units by aligning dipoles along the same direction. In the case of PVDF, the all-*trans* (β-phase) is the most highly polar conformation because of the alignment of all its dipoles in the same direction normal to the chain axis. The tg^+tg^- conformation (α-phase) is also polar, but because of the inclination of dipoles to the molecular axis, it has components of the net moment both perpendicular and parallel to the chain (figure 3-2).
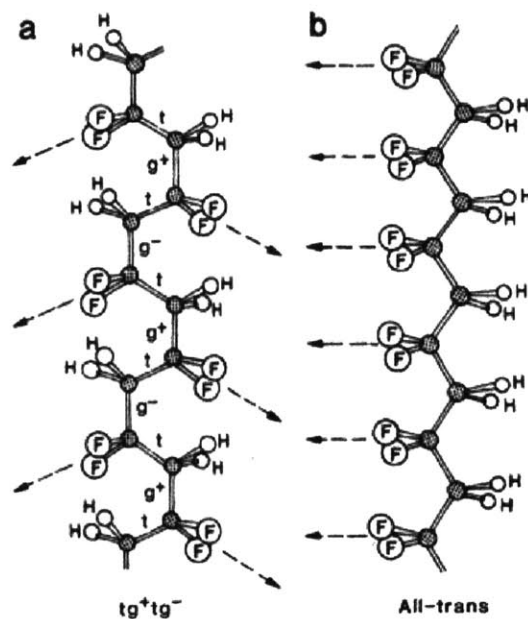
Figure 3-2: Schematic description of the (a) tg^+tg^- and (b) all-*trans* conformations of PVDF [29]. The arrows indicate projections of the -CF$_2$ dipole directions on planes defined by the carbon back-bone.

3. The polymer chains should be packed into a crystal structure in which the dipole moments of different polymer chains are aligned. This explains why PVDF in the β-phase is ferroelectric while the α-phase is paraelectric. The unit cell of the lattice of α-PVDF consists of two chains in the tg^+tg^- conformation whose dipole components normal to the chain axis are antiparallel, thus neutralizing each other. In the β-phase, the all-*trans* chains are arranged in a quasi-hexagonal close-packed structure with their dipoles pointing in the same direction (fig. 3-3).

(a)   (b)
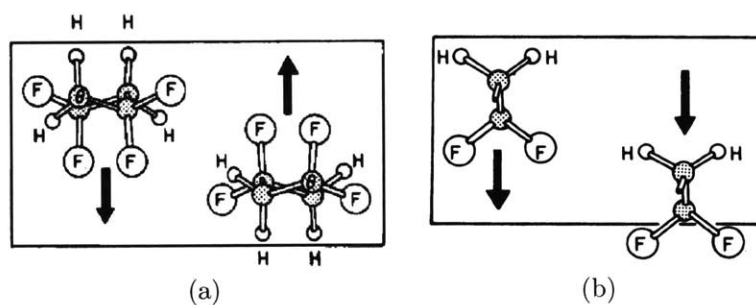
Figure 3-3: Unit cells of the α- and β-phases shown in projection parallel to the chain axes [29]. Arrows indicate dipole directions normal to the molecular axes.

PVDF seems to be a good candidate for a piezoelectric material in a thermally drawn fiber, since it is the most widely used piezopolymer and has already found a number of applications. Furthermore, its relatively low melting temperature ($T_M = 177°C$) makes it compatible with a wide range of thermoplastics. However, PVDF when cooled from the melt is in the dielectric α-phase, its thermodynamically most stable form. The application of a high mechanical stress is required to induce a phase transformation into the ferroelectric β-phase, as shown in figure 3-4. The film is subsequently poled to obtain macroscopic polarization.
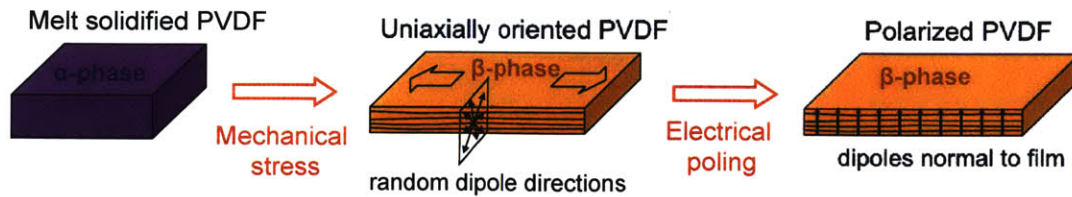
Figure 3-4: Processes commonly employed to obtain piezoelectric PVDF films

At first, one could think that the mechanical extension step could be achieved during the fiber draw itself, since the draw is performed under high stress conditions. But in reality this mechanical extension must be performed at high stress and low temperature (below 90°C) to effectively induce a transformation of the individual polymers chains from the tg^+tg^- to the all-*trans* conformation. Because thermal drawing requires the temperature to be higher than the melting temperature of PVDF (177°C), PVDF during the draw extends by rearrangement of the individual polymers chains, without undergoing a phase transformation. To overcome this limitation and achieve the desired ferroelectric phase in the fiber, we use a copolymer of PVDF with trifluoroethylene (P(VDF-TrFE)) with 70% VDF molar fraction (Solvay). Due to steric hindrance by the bulky fluorine atoms, this copolymer assumes the ferroelectric β-phase spontaneously upon solidification from the melt without necessitating any mechanical stress, making it particularly suitable for the thermal fiber drawing process (figure 3-5). Furthermore, although P(VDF-TrFE) has a slightly reduced spontaneous polarization compared to PVDF, it can be annealed to nearly 100% crystallinity (whereas pure PVDF is typically limited to 50% crystallinity) and therefore exhibit a stronger piezoelectric response.
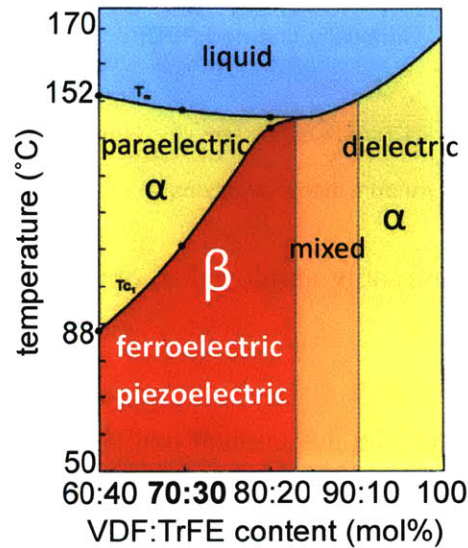
Figure 3-5: Phase diagram of P(VDF-TrFE) copolymers [33]. The copolymer with 70% VDF molar fraction spontaneously assumes the ferroelectric β-phase.

3.2 Maintaining the fiber geometry

3.2.1 The challenge: capillary instability

During the fiber draw, the different materials that constitute the preform are heated and flow in the state of viscous liquids along a complex path in the cone reduction region, until they reach a cooler zone and solidify again. Intuitively, it seems likely that the initial preform geometry will not be maintained during this complex process and the structure will be subject to deformations. Indeed, even a simple cylinder of viscous liquid is subject to instabilities as it flows, as was observed by Lord Rayleigh as early as 1878 [34]. The reason for this phenomenon is capillary forces: viscous liquids, by virtue of their surface tension, seek to adopt a geometry that minimizes their surface energy. One implication of capillary forces for fiber draws is that large

aspect-ratio geometries such as thin cylindrical shells tend to break-up into filaments during the draw process [35]. The linear theory of capillary instability states that the time constant of capillary instability growth $\tau_{\text{capillary}}$ is proportional to the feature size r and viscosity η, and inversely proportional to the surface tension γ [34, 36]:

$$\tau_{\text{capillary}} \propto \frac{r\eta}{\gamma} \tag{3.1}$$

The draw process decreases the feature size and viscosity, thereby naturally facilitating capillary break-up. Conversely, designing fibers with larger features or higher viscosity materials will slow the break-up process. The stability criterion for thermal drawing can be expressed as $\tau_{\text{capillary}} > \tau_{\text{dwelling}}$, where $\tau_{\text{dwelling}} \approx 100$ sec is the period during which the materials are in a viscous state before exiting the hot furnace [37].

3.2.2 Cladding material selection: PC

Previous studies established the use of the stability criterion to theoretically guide the selection of material sets that are potentially compatible for co-drawing and identified polycarbonate (PC) as a suitable cladding material for PVDF [38]. To confirm this, dynamic and steady-shear rheology measurements were performed on PC and P(VDF-TrFE) at different temperatures, to obtain the material viscosities as a function of temperature. These viscosities were fitted to an Arrhenius equation:

$$\eta(T) = \eta(T_{ref}) \exp\left(\frac{E_A}{R}\left(\frac{1}{T} - \frac{1}{T_{ref}}\right)\right) \tag{3.2}$$

45

where E_A is an activation energy, R is the universal gas constant, and T_{ref} is the reference temperature at which the steady-shear measurement is performed. The retrieved values for PC and P(VDF-TrFE) are shown in table 3.2. Plotting these viscosities as a function of temperature (figure 3-6) shows that between 210 °C and 230 °C, the viscosities of PC and P(VDF-TrFE) are comprised between 2.5 10^4 Pa.s and 1.1 10^5 Pa.s, which is a range suitable for thermal drawing.

	T_{ref}	$\eta(T_{ref})$	E_A	r^2
PC	250 °C	13,000 Pa.s	111.73 kJ/mol	0.9995
P(VDF-TrFE)	240 °C	18,500 Pa.s	73.562 kJ/mol	0.9999

Table 3.2: Results of the Arrhenius fit for the temperature dependance of PC and P(VDF-TrFE) viscosities.
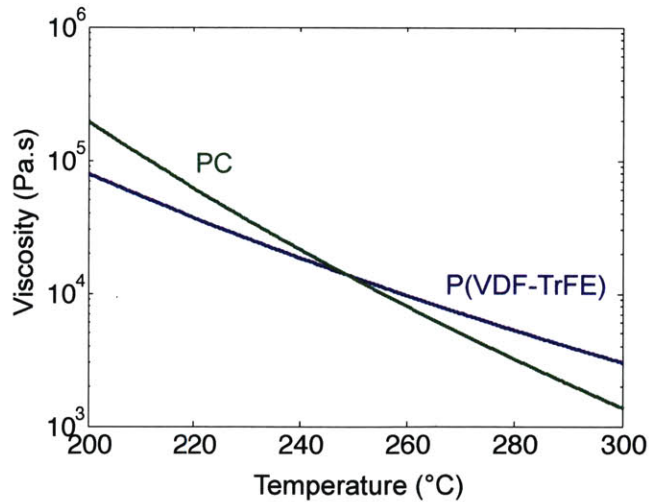
Figure 3-6: Viscosities of PC and P(VDF-TrFE) as a function of temperature

3.2.3 Electrode material selection: CPE

Most piezoelectric devices are designed as parallel-plate capacitors, with the piezo-electric material sandwiched between two electrodes. Therefore, it seems intuitive to initially design a fiber device similar to the one shown in figure 3-7a. This design, unfortunately, would not survive the draw process. Due to the very low viscosity of molten metals (< 1 Pa.s), a structure consisting of a cylindrical shell of metal encapsulated in a polymer cladding breaks up when it is drawn, according to the capillary instability mechanism described in section 3.2.1. Figure 3-7b shows an example of such a break-up. Traditionally, the incorporation in polymer fibers of low
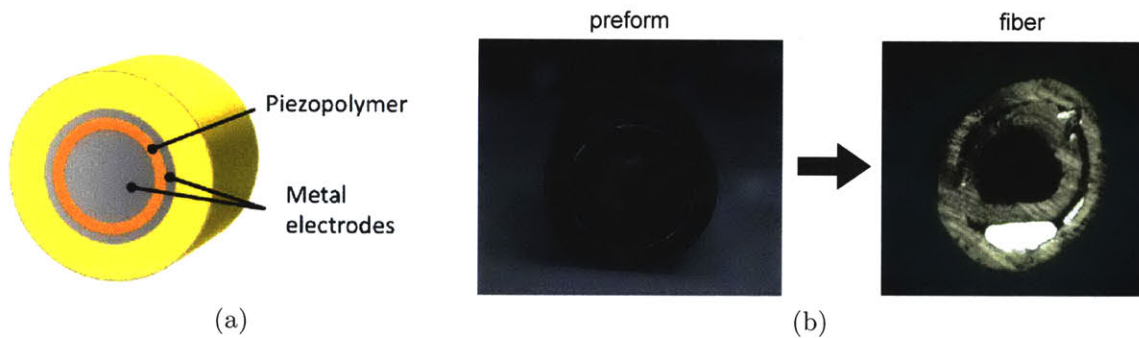
Figure 3-7: a) Intuituive design of a piezoelectric fiber. b) Example of capillary break-up of a metallic shell.

viscosity materials, such as metallic electrodes, is achieved by restricting them to small regions and small aspect-ratio cross-sectional geometries, like squares, to limit their surface area and avoid capillary break-up. However, in the case of piezoelectric fibers, limiting the surface area of the electrodes would effectively limit the active area of the piezoelectric layer and would be detrimental to the power and sensitivity of the device. Furthermore, due to the crystalline nature of the piezoelectric ma-

terial, the piezoelectric layer contacted by electrical conductors would lead to the formation of multiple adjacent low viscosity domains of high aspect ratio, thereby worsening capillary breakup and mixing due to flow instabilities. The introduction of a high-viscosity spacer material between the piezoelectric layer and the electrode may prevent capillary break-up, however it would also preclude effective poling of the piezoelectric layer by blocking charge injection.

The strategy to overcome this challenge is to identify a non-metallic electrode material that would have a viscosity between $10^4 - 10^5$ Poise at the draw temperature, enabling it to be co-drawn with P(VDF-TrFE) and PC in a high aspect-ratio geometry while resisting capillary break-up. Conductive polymer composites are good candidates for such a material. Conductive composites composed of a polymer matrix embedded with conductive fillers, such as carbon-black particles, graphite fibers, carbon nano-tubes, and metallic fillers have been developed since the 1970s and used in a variety of applications from electromagnetic interference shielding and dissipation of electrostatic charges to semiconductor materials and positive temperature coefficient (PTC) materials [39]. Two commercially available carbon-black filled polymer composites were studied as potential electrode materials: carbon-loaded polycarbonate (CPC) and carbon-loaded polyethylene (CPE). Studies of the electrical properties of these carbon-black composites using percolation theory suggest that the main mechanism of conduction is through electron tunneling between carbon black particles [40, 41]. Differential scanning calorimetry (DSC) measurements showed that their glass transition temperatures are $T_g(\text{CPE}) = 123°C$ and $T_g(\text{CPC}) = 149°C$, therefore
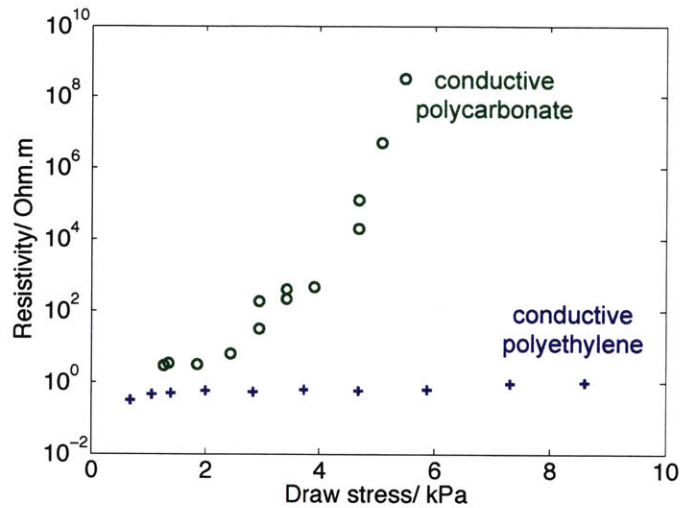
Figure 3-8: Resistivity of CPE and CPC as a function of draw stress

both are compatible for co-drawing with a PC cladding ($T_g(\text{PC}) = 148°\text{C}$). However, their electrical behavior as a function of the draw conditions differs greatly, as shown in figure 3-8. Rheology measurements revealed that CPC also has a viscosity that is two to three orders of magnitude higher than that of PC during the draw. Two viscosity-related mechanisms can explain the stress-induced drop in conductivity of CPC. The first is that if the viscosity of a carbon-loaded polymer during the draw is too high, the carbon-black aggregates can undergo a high degree of breakdown resulting in a much-reduced conductivity [42]. Preliminary SEM studies of drawn CPC suggest a second mechanism: thermal draw of the high-viscosity matrix would result in a stress-induced redistribution of the carbon-black particles in a non-random way, thereby decreasing the conductivity. The large resistivity of CPC has already been successfully exploited in fiber materials [43]. A better understanding of the

49

influence of the draw process on the properties of CPC would enable its use as a tunable resistivity material.

CPE has a viscosity that is low enough to maintain a conductivity that is independent of the draw conditions, specifically the level of stress experienced by the fiber, while remaining high enough to avert capillary break-up, and was therefore chosen as the electrode material. CPE layers have adequate conductivity ($\sim 1\,\Omega.$m) over the frequency range from DC to tens of MHz, thus facilitating short range (hundreds of microns) charge transport on length scales associated with the fiber cross section. Conductivity over larger distances (cm $\sim$ m) along the length of the fiber was ensured by the incorporation of thin metallic buses.

3.3 Piezoelectric fiber fabrication results

3.3.1 Piezoelectric fiber fabrication method

Having identified the constituent materials, we design two piezoelectric fiber architectures shown in figure 3-9. The first step of fabrication is to assemble the different materials selected to constitute the piezoelectric fiber into a preform. P(VDF-TrFE) (70:30 molar ratio, Solvey) is melt-pressed from pellets at 180°C and 100 bars to form a 500 μm-thick film. CPE is purchased is the form of 100 μm-thick films, which are then pressed together for 10 minutes at 95°C and 50 bars to form 300 μm-thick films. PC is purchased in the form of films and slabs (McMaster) of various thicknesses. For the metallic electrodes, the eutectic alloy $Bi_{58}Sn_{42}$ ($T_M = 138$°C, Indium
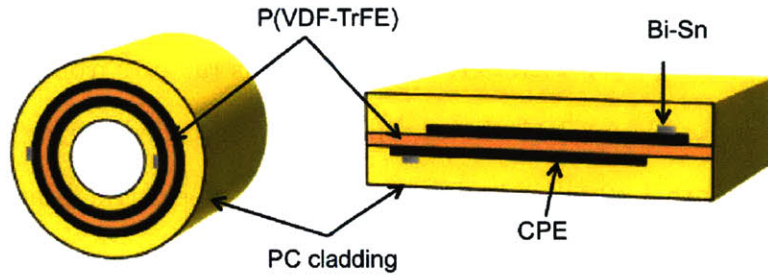
Figure 3-9: Designs of piezoelectric fibers with cylindrical and rectangular cross-sections.

Corporation) is selected. The assembly technique depends on the fiber geometry. For cylindrical fibers, the different materials are assembled as concentric shells using a rolling technique, as shown in figure 3-10a. For rectangular fibers, milling is used to assemble the layers as shown in figure 3-10b. In both cases, the structure is consolidated in a vacuum oven at 185°C for 20 minutes to remove trapped gas and form high quality interfaces. The preform is then thermally drawn in a three-zone vertical tube furnace with the top-zone temperature at 150°C, the middle-zone temperature

(a)   (b)
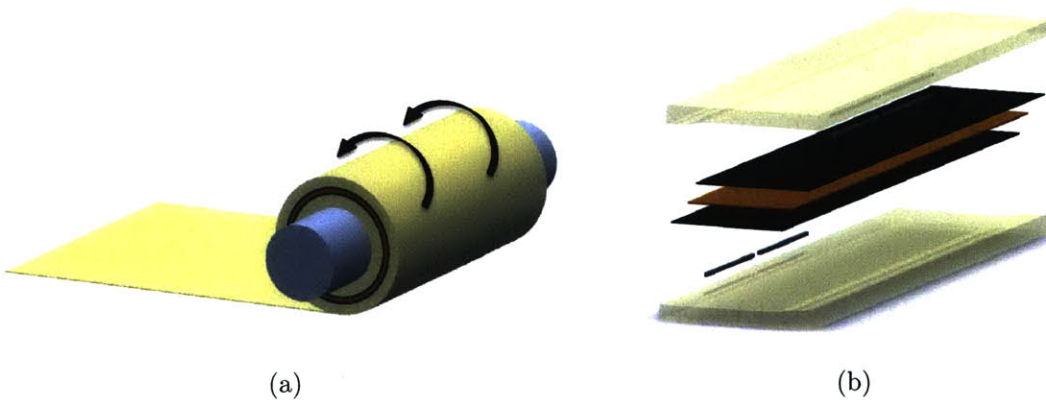
Figure 3-10: a) Cylindrical preform assembly. b) Rectangular preform assembly.

at 230°C, and the bottom-zone temperature at 110°C. This procedure yields tens of meters of piezoelectric fiber with external dimensions ranging from few hundreds of microns to 1.5 mm. Figure 3-11 shows typical data recorded during a piezoelectric fiber draw, and figure 3-12 features photographs of piezoelectric fiber preforms after the draw.

3.3.2 Fiber inspection

Since uniformity of the external geometry of the fiber does not ensure that of the internal structure, Scanning Electron Microscopy (SEM) is used to image the cross-sections of the fiber and verify that the structure of the device was well maintained from preform to fiber. To this effect, fiber samples are selected from various points along the fiber and are polished by mechanical polishing or ion-beam polishing. Figure 3-13 shows SEM micrographs of the cross-sections of cylindrical and rectangular piezoelectric fibers, revealing very well maintained structures in the fibers.

From these SEM micrographs, we can estimate the uniformity of the piezoelectric polymer layer thickness across its width. We find a standard deviation of 3% in the samples studied. To investigate the uniformity of the structure along the length of the fiber, we cut a one meter long portion of fiber into 3 cm-long segments, on which we measure the capacitance. Fluctuation in the averaged thickness of the piezoelectric P(VDF-TrFE) layer should result in a proportional fluctuation in the capacitance. We find a standard deviation of 4%.

52
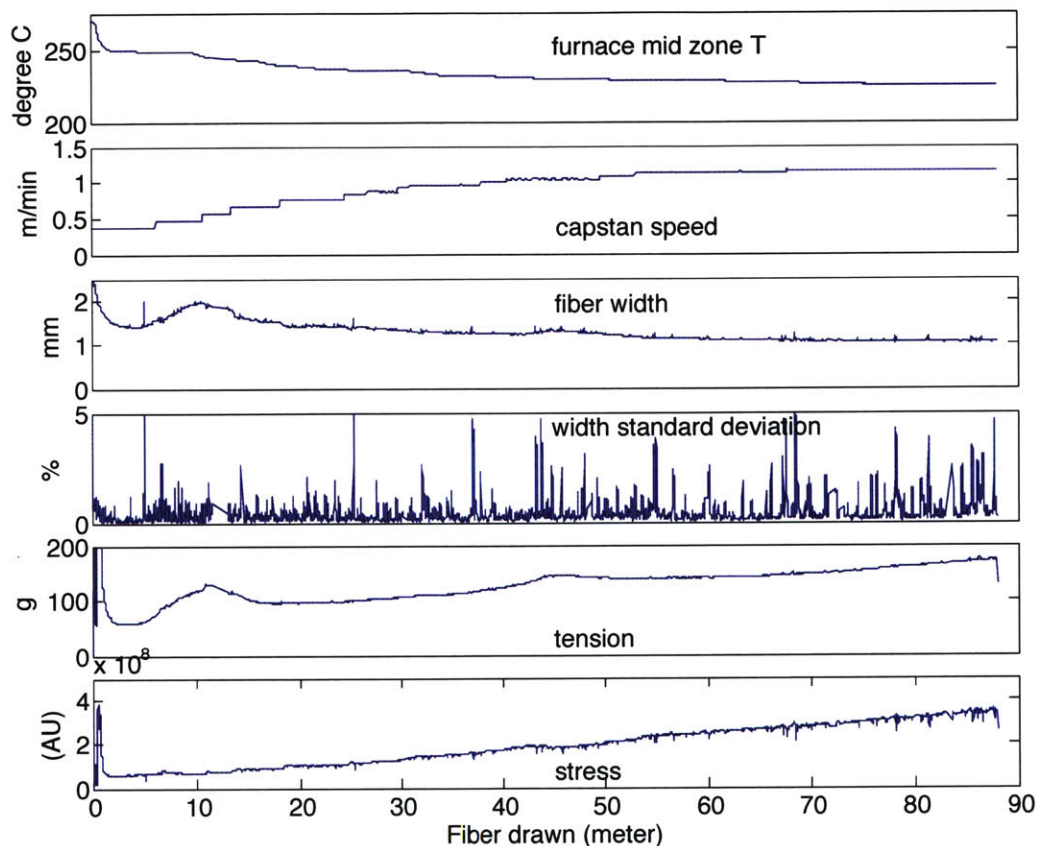
Figure 3-11: Typical data recorded during a piezoelectric fiber draw. The bait-off is done at a mid-zone temperature of 270°C. During the draw, the furnace temperature is progressively lowered to 230°C. At the same time, the capstan speed is increased so that the fiber reaches the target dimensions (in this case, a rectangular fiber with a width of 1 mm and a thickness of 300 μm). The draw stress also increases during the draw to counter surface tension driven deformations. We notice two "bumps" in the fiber thickness around 11 m and 45 m which reveal the arrival of metallic electrodes in the reduction zone.
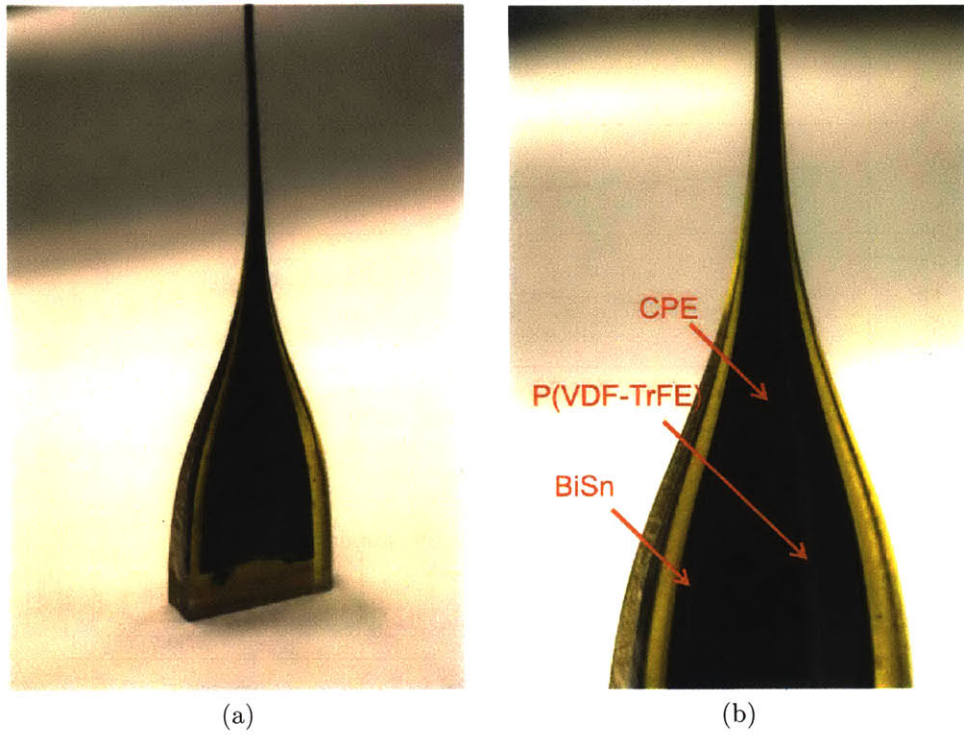
Figure 3-12: Photographs of piezoelectric fiber preforms after the draw.
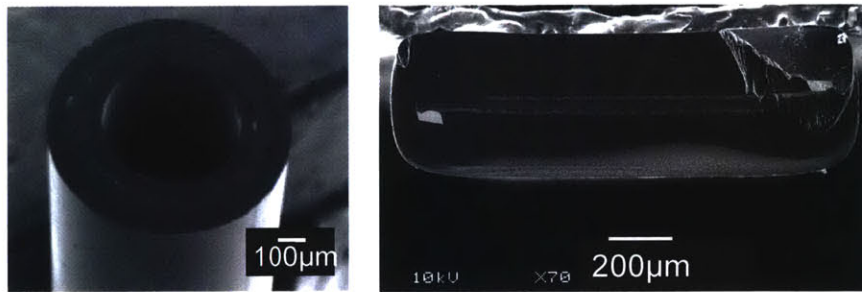
Figure 3-13: SEM micrographs of the cross-sections of a cylindrical (left) and rectangular (right) piezoelectric fiber.

54

Cross-sectional images along the fiber can also help to reconstruct a "film" of the draw process as shown in figure 3-14. This is an important step both to get a better understanding of what happened during the draw, and to select the best portions for testing from the more than 100-meter long fiber.

(a)

(b)

(c)
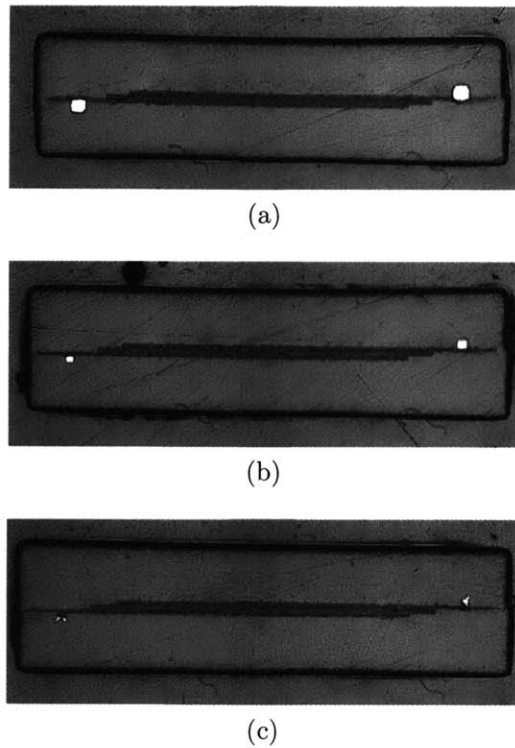
Figure 3-14: Fiber inspection under the optical microscope. a) Beginning of the draw: the metal electrodes are big and round, indicating a high temperature and low stress. b) Middle of the draw: the metal electrodes are square and the overall features of the fiber are very well maintained. c) End of the draw: the metal electrodes are almost gone.

3.3.3 XRD measurements

To verify that P(VDF-TrFE) in the fibers is indeed in the ferroelectric phase, wide angle X-ray diffraction (XRD) measurements are performed on P(VDF-TrFE) copolymer domains harvested from the drawn fibers and are compared to the material used for the preforms (figure 3-15). Both specimen exhibit identical peaks at 2θ = 19.9°, 35.2°, and 40.7°, which correspond to (200)/(110), (001) and (310)/(020), (111)/(201) and (400)/(220) peaks of the β-phase respectively [44], thus establishing that the drawn copolymer solidifies in its β-phase. The crystallinity fraction as calculated from these XRD patterns is over 90 percent.
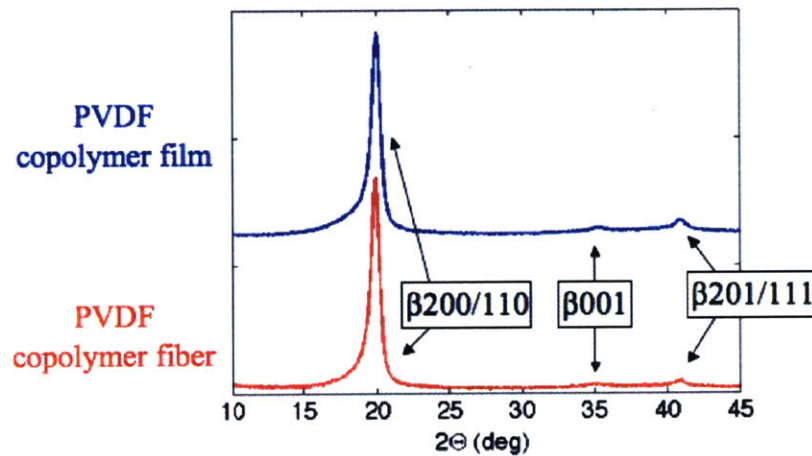
Figure 3-15: XRD measurements of P(VDF-TrFE) copolymer in the preform and the fibers

3.4 Poling

3.4.1 Contacting and poling protocol

We have established that P(VDF-TrFE) in the fiber is in the ferroelectric phase, however due to the random orientation of ferroelectric micro-domains, it is not piezo-electric. A poling step is necessary, during which a strong applied electric field ($>$ 60 MV/m) forces the individual dipoles into alignment (figure 3-16a). Before it is

(a) (b)
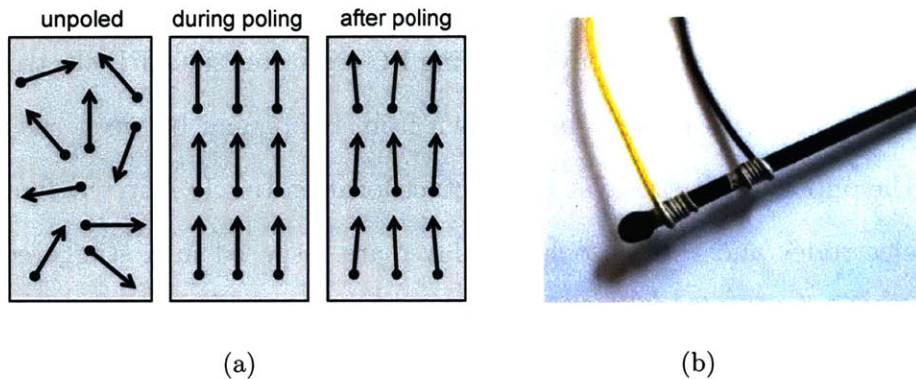
Figure 3-16: a) Schematic of the poling process of a ferroelectric material. b) Photo-graph of a contacted piezoelectric fiber sample. The end of the fiber is covered with liquid electrical tape.

poled, a fiber sample needs to be contacted so that its internal electrodes can be connected to an external electric circuit. This is done by shaving off the cladding layer using a microtome blade under a stereomicroscope until a CPE electrode is exposed. Flash-dry silver paint (SPI supplies) is applied on the exposed electrode and an electric wire is connected to it by wire-wrap. This is then repeated for the second electrode. Figure 3-16b shows a photograph of a contacted piezoelectric fiber sample. Once the fiber samples are contacted, they are poled at room temperature

using a DC high power supply by applying an electric field of 60 - 100 MV/m for a few minutes.

3.4.2 The challenge: dielectric break-down

What makes poling a particularly challenging step is the risk of dielectric break-down due to the very high applied electric field. Once a fiber breaks down, it is shorted and cannot be used as a piezoelectric device anymore. The design of the piezoelectric fiber incorporates improvements intended to prevent dielectric break-down, as shown in figure 3-17. A thick buffer layer of cladding PC separates the CPE electrodes from the edge of the fiber, to prevent breakdown from happening between the wrapped wire and the opposing electrode at the contact location (circle A in the figure). The polymer electrodes and the piezoelectric layer are disposed in a staggered fashion to avoid dielectric breakdown through the PC cladding, which has a lower dielectric strength than P(VDF-TrFE) (circle B in the figure). In addition, liquid electrical tape is painted on the end facets of the fiber, to avoid dielectric breakdown through air (figure 3-16b).
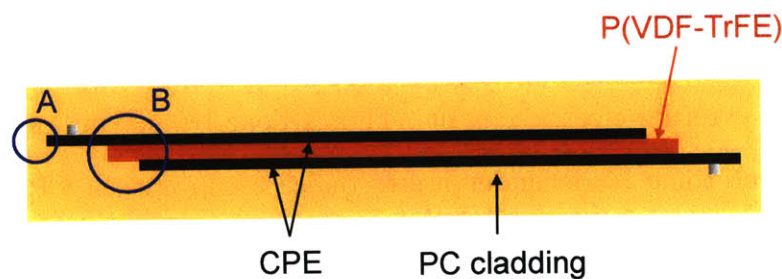
Figure 3-17: Design of the piezoelectric fiber to avoid dielectric breakdown

The poling process renders piezoelectric fibers particularly vulnerable to structural

imperfections along their length. Layer thickness variations either in the lateral or in the longitudinal directions can preclude the formation of the coercive field needed for poling. Given that the threshold of poling is close to the dielectric strength [45], fluctuations in the ferroelectric layer thickness will reduce the average poling fields, because the applied poling voltage is limited by the thinnest portions where the onset of dielectric break-down begins. Thicker portions experience incomplete poling which leads to an overall sub-optimal piezoelectric response, an effect further aggravated by the nonlinear relation between the remnant polarization and the external electric fields as shown in figure 3-18 [46].
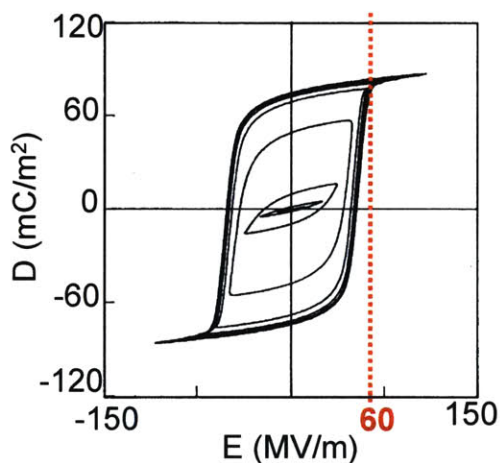
Figure 3-18: Hysteresis loop for P(VDF-TrFE) [46].

3.4.3 Depolarization

Piezoelectric materials can lose their piezoelectric properties over time due to a drop in remnant polarization (figure 3-19a). This phenomenon is called *depolarization* or

59

retention loss and has been studied extensively on ferroelectric materials for memory devices, such as ferroelectric random access memories (FRAMs). While the mechanisms responsible for retention loss are not fully resolved, it is generally understood that retention loss results from the presence of depolarization fields in the ferroelectric layer [47]. These fields always exist to a certain extent, and arise naturally from the incomplete screening of polarization at the electrode-film interface. As shown in figure 3-19b, there exists a finite separation between the polarization charge Q_p and the compensating free charge in the electrodes Q_e [48]. This results in the presence of a depolarization field $\mathbf{E}_{\text{dep}}$, whose direction is opposite to that of the bulk polarization. If the magnitude of $\mathbf{E}_{\text{dep}}$ exceeds that of the coercive field $\mathbf{E}_c$, partial reversal of the polarization may occur.
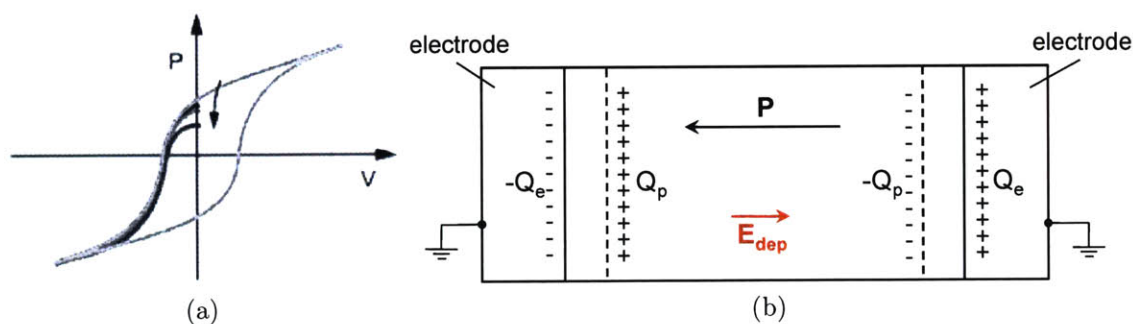
Figure 3-19: Depolarization in ferroelectric films. a) Polarization drop due to retention loss [49]. b) Depolarization field arising from incomplete cancellation of the space charge and polarization charge at the electrode-ferroelectric interface (adapted from [48]).

Depolarization has been observed on a number of piezoelectric fiber samples. Figure 3-20 shows an example of the decay in piezoelectric performance of a fiber sample after poling: the signal strength decreases by a factor of 2 to 3 in a period of 52 hours

before reaching a plateau value. Interestingly, depolarization was not observed in all fiber samples, and occurred at very different rates in different samples, with some samples depolarizing in just a few hours while others decayed over several weeks.
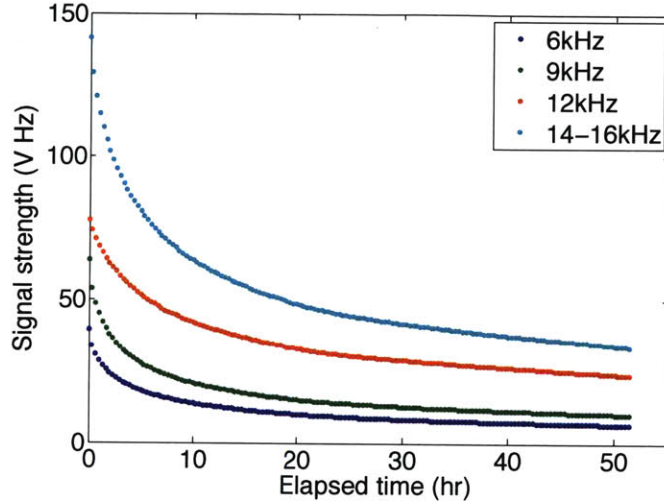
Figure 3-20: Depolarization in a piezoelectric fiber sample over 52 hours (data courtesy of Dr. Zheng Wang).

Several factors could affect depolarization in fibers and explain these variations: poling conditions, post-draw delamination phenomena, residual stress distribution, and fiber materials (for the cladding and the electrodes). Several studies in the literature have shown that polarization retention in P(VDF-TrFE) films is influenced by poling conditions, specifically pulse width and amplitude [50, 51]. These studies demonstrate that pulse widths longer than a few ms are preferable, with a pulse amplitude exceeding the poling threshold. Another study has established that pulsed poling is preferable to DC poling, because it allows deformations and space charges to relax, resulting in a more homogeneous electric field [52]. The efficiency of DC and pulsed poling were compared on piezoelectric fiber samples, however no sig-

nificant difference was observed on the retention behavior. This is consistent with observations that poling conditions have a significant effect on polarization retention for ferroelectric films below a critical thickness (less than 60nm), which is orders of magnitude smaller than the piezoelectric film thickness in the fibers [51].

Post-draw delamination between the piezoelectric layer and CPE is regularly observed in SEM micrographs of fiber cross-sections and could be considered a potential source of loss of performance of the fiber devices. The delamination, if it grew over time, would result in a gradual loss of electrical contact between the P(VDF-TrFE) layer and the electrodes, and consequently a decrease in the device response. However, microscope examinations of a piezoelectric fiber samples polished at different depths revealed that the delamination is solely a result of the fiber cut, and does not extend over more than 3-5mm into the fiber. Therefore it can not be accounted for the observed drop in fiber response.

Residual stresses are an inevitable by-product of the thermal drawing process, and can affect the polarization retention of fiber devices. Prior studies have shown that polarization is sensitive to mechanical stresses, and that ferroelectric materials under tensile stress can show a preferred orientation for polarization [53]. The presence of residual stresses in drawn fibers is most obvious when fiber samples are heated after the draw: residual tensile stresses cause them to shrink, sometimes dramatically (over 50%). Wide-angle X-ray scattering (WAXS) measurements on drawn P(VDF-TrFE) have also revealed a slight orientation of the polymer chains due to the draw

stress. The amplitude of the residual stress in the P(VDF-TrFE) layer is affected by draw conditions, especially temperature and draw stress (defined by the draw tension divided by the fiber cross-sectional area), however no significant difference in depolarization behavior could be observed for fiber samples drawn at various temperatures and stresses. A possible explanation is that it is the distribution rather than the amplitude of residual stresses that influences depolarization. Residual stresses may not be uniform across the fiber width and length, and could lead to inhomogeneous polarization of the piezoelectric layer, which could in turn favor depolarization.

To study the influence of fiber materials on depolarization, piezoelectric fibers were prepared using two sets of cladding/electrode materials: PC/CPE and PSU/CPC. Furthermore, the PC/CPE fiber samples were divided in two groups depending on whether they had additional metallic buses or not. The results showed no difference between the PC/CPE and PSU/CPC samples, however they revealed a determining influence of the presence of metallic buses: 100% of the non-depolarizing samples had metallic electrodes. Of the samples with metallic electrodes, around 20% showed no sign of depolarization. These results suggest that the incorporation of small metallic buses can prevent depolarization, at least in a statistical way if not in 100 % of the devices. One can think of two hypothesis to explain the mechanism by which metallic electrodes influence polarization retention. One is that they reduce polarization inhomogeneity along the length of the fiber. Inhomogeneous polarization of P(VDF-TrFE) films has been reported in a number of studies [54, 55]. As we have already mentioned, polarization inhomogeneity may result from non-uniform resid-

ual stress distribution across the piezoelectric layer. Structural phase inhomogeneity may also be a cause of polarization inhomogeneity in ferroelectric polymers from the PVDF family. It has been demonstrated that the non-ferroelectric phases in PVDF, including the amorphous phase and the α-phase, play an important role in the polarization and depolarization processes [56]. The presence of these phases results in the accumulation of interfacial charges at the boundaries between different phases and therefore contribute to depolarization fields. By contributing to reduce the polarization inhomogeneity, metallic buses may reduce depolarization. These studies also suggest that PVDF-based polymers are particularly prone to depolarization, which may explain why 80% of the samples with metallic electrodes still depolarized.

A second hypothesis to explain the influence of metallic buses is that they affect the CPE electrode carrier density. Many studies point to the importance of the electrode-film interface and the electrode carrier density on depolarizing fields [47, 54, 57]. It can be expected that the use of carbon-loaded polymer instead of metal as the electrode material will significantly affect the polarization behavior. The relatively smaller carrier density in CPE compared to metal should lead to a longer screening length, and therefore a stronger depolarizing field even in micrometer-thick piezoelectric films, as has been observed in studies with semiconducting electrodes [47, 57]. The influence of the presence of metallic buses on the polarization retention in some fiber samples may therefore be explained by the injection of additional carriers in the CPE electrodes, and therefore a weakening of the depolarization field. Given that the metallic buses are located near the edge of the fiber and cover a very small

64

surface, this effect is likely to be small. However, modified fibers integrating a larger number of electrodes could be designed to further investigate this issue and prevent depolarization in a bigger fraction of devices.

Chapter 4

Piezoelectric fiber devices for acoustic sensing and emission

4.1 Motivation

Monolithic processing of piezoelectric transducers in fiber form presents opportunities in a variety of applications across a wide range of acoustic frequencies. Piezoelectric PVDF transducers have been demonstrated at frequencies up to 24 GHz [58] and have also been used commercially at a few Hz (Measurement Specialties Inc.). Figure 4-1 shows examples of applications of acoustic waves across this frequency range. Of particular interest are a number of applications that are well matched to the fibers geometry. The large aspect ratio of the piezoelectric fiber devices could form the basis for an active catheter capable of accurate pressure and flow measurements in inaccessible regions of the body. Specific interest exists for intravascular ultrasound

67

Medical imaging

←———→

←——————— Acoustic sensors ———————→

Accelerometer   Guided waves   Acoustic microscopy

←———→   ←———→   ←——————————→

←— Speaker →   ←—— Cavitation ——→←—— NDT ——→←— SAW —→

10²   10³   10⁴   10⁵   10⁶   10⁷   10⁸   10⁹   10¹⁰

Frequency (Hz)
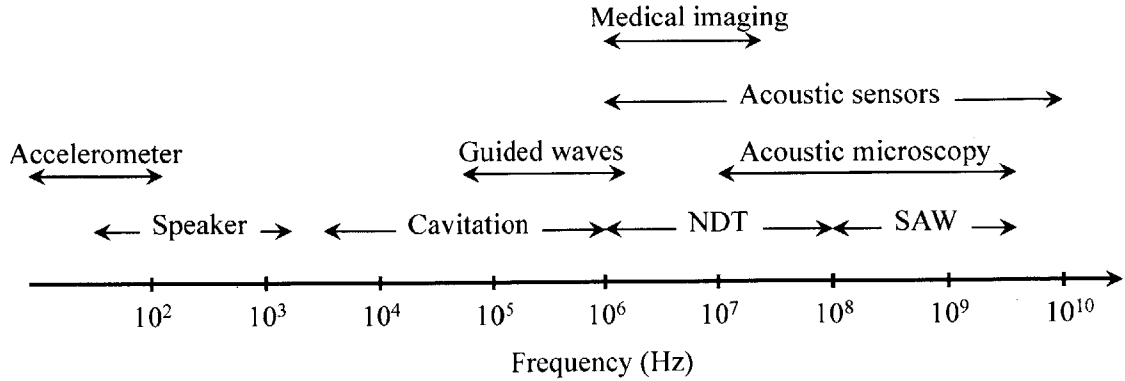
Figure 4-1: Applications of acoustic waves (adapted from [59]).

(IVUS) to image arterial walls, inter-cranial pressure monitoring for hydrocephalus patients, implantable dynamic pressure sensors for urodynamic studies, and acoustic microscopy inside acoustically-opaque organs [60–63]. In addition to these diagnostic and monitoring applications, ultrasound transducers have found use in many therapeutic applications, including controlled drug delivery triggered by ultrasound waves [64]. Uniform piezoelectric fibers over tens of meters are also ideal for distributed sensing [4]: their sensitivity to stress and strain combined with their low profile make them ideal for constructing minimally-perturbative (sparse) sensor meshes for studying large-area distributions of the pressure and velocity fields in myriads of fluid flow applications including oceanic current monitoring [65].

In this section, we start with a careful characterization of piezoelectric fibers as acoustic wave sensors and emitters. Three distinct characterization methods are used to establish their acoustic and electrical properties from kHz to MHz frequencies. We then highlight some of the unique properties of piezoelectric fiber devices

by describing acoustic wave shaping applications enabled by the mechanical flexibility of fiber devices and control over the fiber cross-sectional geometry. Finally, limitations of piezoelectric fiber devices are identified and strategies to improve their performance are discussed through the use of alternate materials and architectures.

4.2   Piezoelectric fiber device characterization

4.2.1   Acoustic characterization

The most direct way to establish the piezoelectric response of the fiber and characterize its performance is to perform acoustic measurements, using the fibers alternately as an acoustic sensor and actuator. The measurement was done in a water tank and at a frequency of 1 MHz. A schematic of the setup is shown in figure 4-2a. A water-immersion ultrasonic transducer (Olympus Panametrics-NDT, 1.0 MHz-centered) is coupled to a fiber sample across a water tank to match the acoustic impedance. At MHz frequencies, capacitive electromagnetic coupling between the transducer circuit and the receiver charge amplifier can be significant even with careful shielding and grounding [66]. To separate the acoustic signals from the electromagnetic interference, we use a pulsed excitation and time-gate the received signals, exploiting the 5 orders of magnitude difference in the propagation speed between acoustic and electromagnetic pulses. The temporal traces of the amplified voltages under a pulsed excitation are measured with a carrier frequency at 600 kHz and a 52 μs temporal envelope at a 6.5 kHz repetition rate. The time delay of the received pulses is consistent with acoustic propagation in water at 1470 $\pm$ 30 m/s. The fibers were shielded
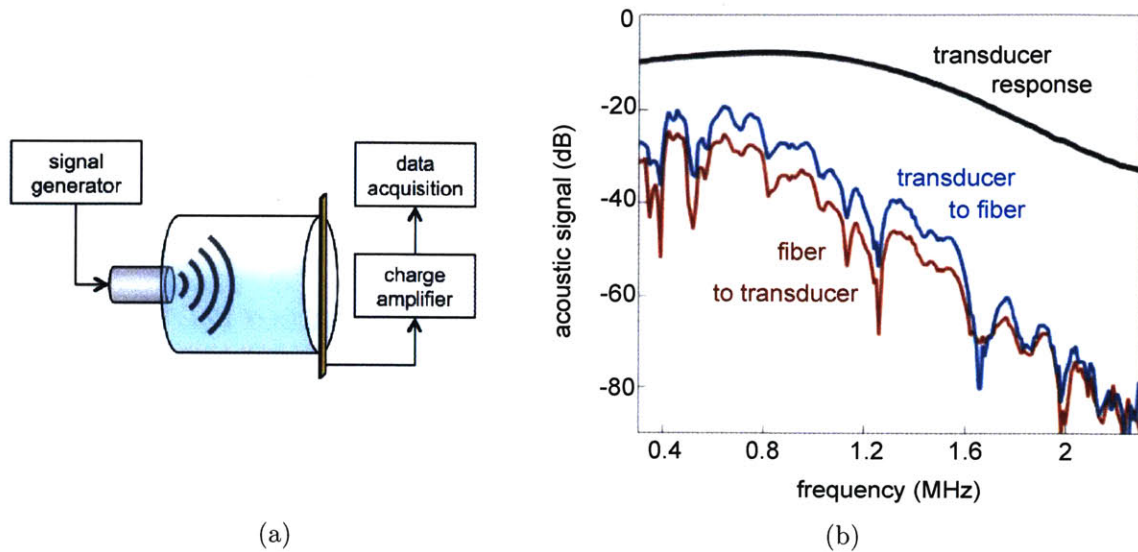
Figure 4-2: a) Experimental set-up for acoustic characterization of piezoelectric fibers. An acoustic wave travels across a water-tank from a water-immersion acoustic transducer to a fiber sample, and vice-versa. b) Acoustic signal detected (blue curve) and emitted (red curve) by a piezoelectric rectangular fiber around 1MHz. The black line is the power spectrum of the 1 MHz-centered commercial transducer used.

by applying conductive silver paint on their entire surface and connecting it to the shield of a coaxial cable.

Frequency domain characterizations of the flat rectangular piezoelectric fibers are performed with a fixed transducer-to-fiber distance of 97 mm (approximately 70 acoustic wavelengths at 1 MHz), with the pulsed excitation and the time-gated signal processing (figure 4-2b). We note that there is excellent agreement between the spectral features of the measured piezoelectric response in the fiber-to-transducer and the transducer-to-fiber configurations. The slowly-varying contour of the fre-

70

quency response is the frequency response of the commercial transducer made of piezoelectric ceramic (PZT). Due to the limited bandwidth of the PZT transducer (shown as the black line in figure 4-2b), its output power and sensitivity vary by about 25 dB in the frequency range of the measurement. Signals measured from the fiber samples therefore carry an identical contour. Although the frequency range is limited here by the bandwidth of the commercial transducer, polymeric piezoelectric elements are in principle broadband and the piezoelectric fibers could operate at a far broader range of frequencies. For example, similar fibers were used to generate audible sound between 7 kHz and 15 kHz with a driving voltage of 5V.

The acoustic response of the fiber shown in figure 4-2b also contains more rapidly-varying ripples. Since the thickness of the fiber is around 300 μm, the thickness modes of the fiber would be at MHz frequencies, and these features must therefore come from sources outside the fiber. We determine that they actually are from reflections from the sidewalls of the water-tank: the geometry of the water tanks creates several series of resonances with free spectral range between 10kHz and 300kHz. Similar features were reproduced when performing the same measurements using a broadband commercial film transducer. Finally, due to the finite conductance of the CPE electrodes, the RC delay of the fiber reduces its efficiency above 1 MHz and causes the increasing gap between the fiber response and the transducer profile.

4.2.2 Optical characterization

An alternate way to establish the acoustic properties of the fiber is to show that the internal piezoelectric modulation indeed translates to a motion of the fiber's surface. This optical characterization of the piezoelectric fiber vibrations is based on heterodyne optical interferometry [67]. A frequency-swept laser (1530-1570 nm at 80 nm/s) is coupled to a fiber-optic Michelson interferometer (figure 4-3). The top arm serves as the reference and the bottom one as the signal, with a delay between the two.
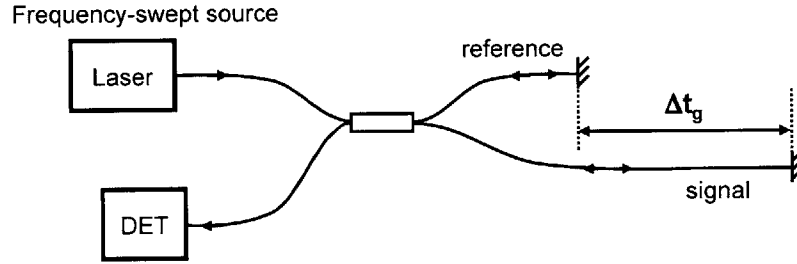
Figure 4-3: Schematic of a heterodyne optical interferometer.

When these signals are mixed, the intensity is of the following form:

$$I(t) = \underbrace{\frac{E_{sig}^2 + E_{ref}^2}{2}}_{\text{constant component}} + E_{sig}E_{ref}\cos((\underbrace{\omega_{sig} - \omega_{ref}}_{\text{beat frequency}})t + \phi)$$

$$+ \underbrace{\frac{E_{sig}^2}{2}\cos(2\omega_{sig}t + 2\phi) + \frac{E_{ref}^2}{2}\cos(2\omega_{ref}t) + E_{sig}E_{ref}\cos((\omega_{sig} + \omega_{ref})t + \phi)}_{\text{high-frequency components}}$$

The high frequency components can be filtered out, leaving the beat frequency, which depends on the delay Δt_g and the frequency sweep rate. In Fourier domain, this translates into a single beat tone as shown in figure 4-4.

72
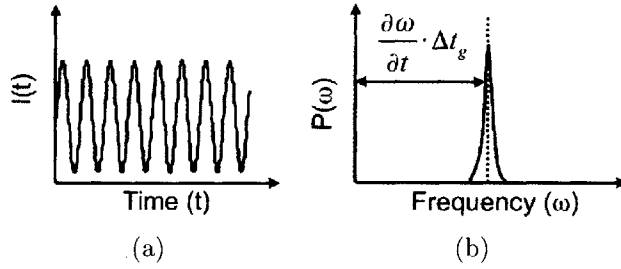
Figure 4-4: (a) Time-domain and (b) Fourier-domain representations of the hetero-dyne signal.

When the mirror in the bottom branch is replaced by the vibrating fiber surface, the frequency of the reflected light is Doppler-shifted. The result is a frequency modulated signal, with the beat frequency as the carrier frequency and the Doppler shift as the modulation frequency. In Fourier domain, this translates as a main beat tone with frequency-modulation spectral side bands spaced at the modulation frequency ω_D on either side of it (figure 4-5).
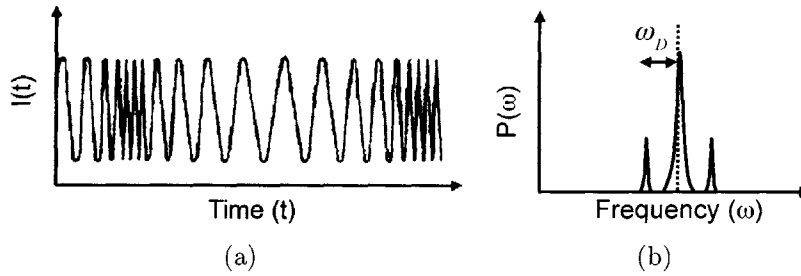
Figure 4-5: a) Time-domain and b) Fourier domain representations of the heterodyne signal modulated by the Doppler shift.

The inherent low noise and high dynamic range (~ 100 dB) in the heterodyne scheme is further improved through real-time frequency calibration with an external Fabry-Perot interferometer (figure 4-6) [68].
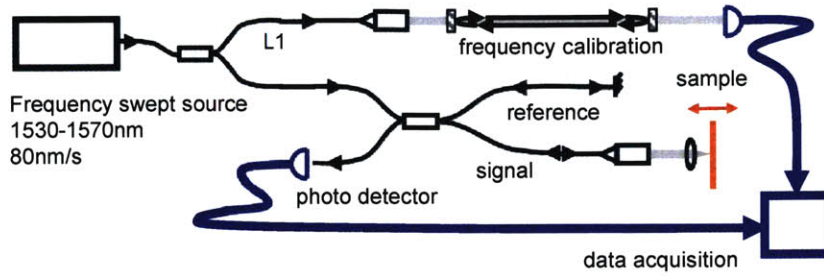
Figure 4-6: Schematic of the optical measurement set-up.

This measurement is carried out on cylindrical and rectangular piezoelectric fibers driven by a sine wave of amplitude 10V at kHz frequencies. The surface of the fibers is coated with silver paint to increase their reflectivity. The left panel of figure 4-7 shows the observed side bands from a cylindrical piezoelectric fiber driven at frequencies from 1.3 to 1.9 kHz. The side band amplitude modulation response is found at $\sim$ -60 dB below the main beat tone around these frequencies. The right panel of figure 4-7 shows the same frequency-modulation side bands for a rectangular piezoelectric fiber. The rectangular geometry couples more efficiently to the optical beam leading to a marked improvement in the signal measured in the side bands compared to the immediate background. It also leads to a 20 dB increase in the side band amplitude with respect to the heterodyne sub-carrier. This ability to optimize the external fiber geometry with respect to the measurement system and application is a compelling property of the multimaterial fiber approach, and will be more extensively discussed in section 4.3.1.

Figure 6-16 shows the frequency dependence of the side band shift and amplitude measured with the rectangular fiber. We see that the frequency dependence of the

74
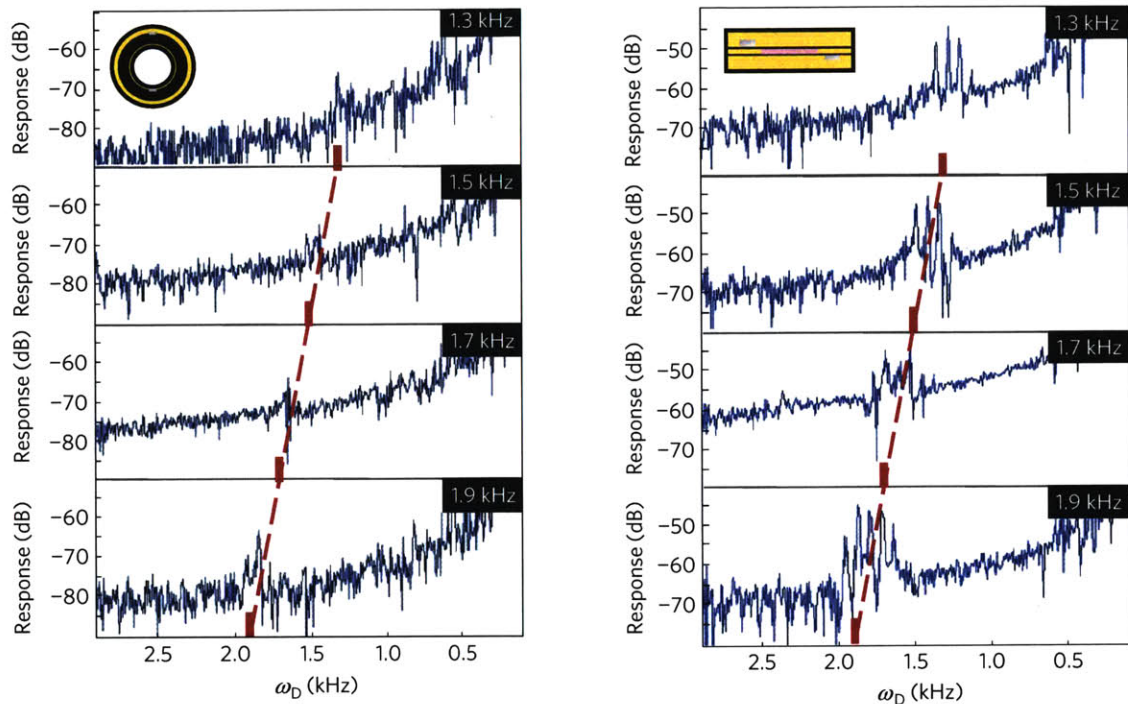
Figure 4-7: Measured frequency-modulation side bands as a function of ω_D for piezo-electric fibers with cylindrical (left) and rectangular (right) cross-sections.

side band shift is linear, as expected. In theory, the amplitudes of the side bands are proportional to the velocity amplitude of the vibration. Figure 4-8b suggests vibrations enhanced or dampened by underlying mechanical resonances of the fiber segment.

4.2.3 Electrical characterization

Another important property of a piezoelectric device is its electrical impedance at various frequencies: not only is its knowledge necessary in designing interface circuits to deliver optimal power-efficiency and sensitivity, but it is also useful in determining
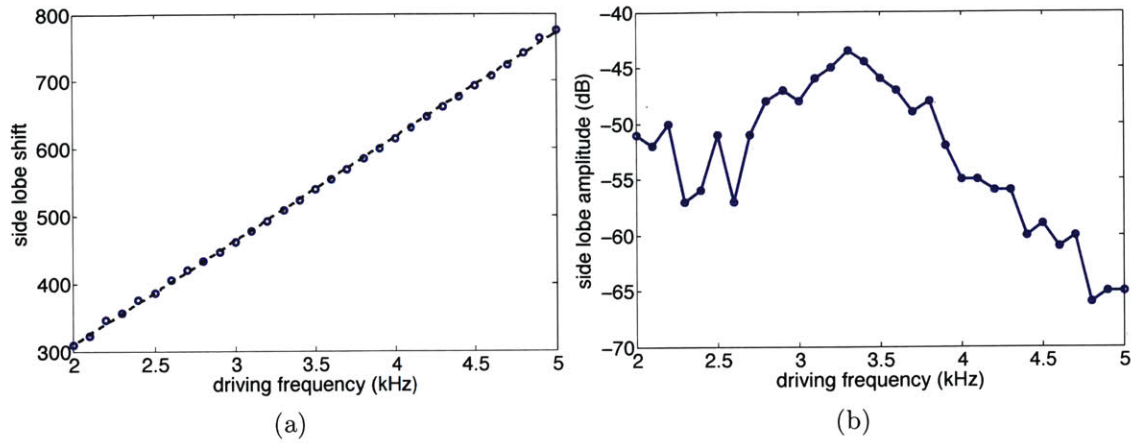
Figure 4-8: a) Frequency dependence of the side band shift. The dotted line shows the linear fit. b) Frequency dependence of the side band amplitude.

the upper limit for the operational frequency, beyond which the transducer sensitivity rolls off rapidly. We use a Hioki 3532-50 LCR HiTester impedance analyzer to measure the frequency response of the fiber impedance from 42Hz to 5MHz . Figure 4-9 displays the equivalent circuit of a fiber under test connected to the impedance analyzer.
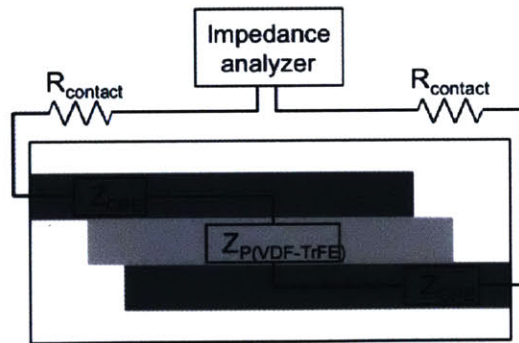
Figure 4-9: Equivalent circuit model of a piezoelectric fiber connected to an impedance analyzer.

In this simplified approach, the different parts of the fiber along the path of the cur-

rent are connected in series and characterized by their electrical impedance: Z_{CPE} for the conductive electrodes, $Z_{P(VDF-TrFE)}$ for the piezoelectric layer and a purely resistive term $R_{contact}$ to take into account losses at the connection with the setup. It has been reported that the otherwise constant resistivity of CPE decreases at frequencies f above a critical frequency f_0 whose value highly depends on the polymer preparation [69]. We have repeatedly witnessed this effect in these fibers — with f_0 in the 0.5 - 10 MHz range — and have included it by considering the following frequency dependence of $Z_{CPE}(f)$:

$$Z_{CPE}(f) = \frac{R_{CPE}}{1 + j\frac{f}{f_0}} \tag{4.1}$$

where R_{CPE} is the low frequency resistance of the electrode. The impedance of the P(VDF-TrFE) layer is calculated as that of a parallel plate capacitor, so that:

$$Z_{P(VDF-TrFE)}(f) = \frac{1}{j\frac{\epsilon_p S_p}{t_p}2\pi f} \quad \text{with} \quad \epsilon_p = \epsilon_p' + j\epsilon_p'' \tag{4.2}$$

where S_p, t_p and ϵ_p are resp. the surface of ferroelectric polymer in contact with the electrodes, its thickness and its dielectric permittivity. ϵ_p has a real and imaginary part that are both considered as independent of the frequency in our approach. The overall impedance of the system is thus modeled as a function of the driving frequency f by adding its components:

$$Z_0(f) = 2R_{contact} + 2Z_{CPE}(f) + Z_{P(VDF-TrFE)}(f) \tag{4.3}$$

77

Figure 4-10 displays the real and imaginary parts (resp. blue and red dots) of the measured impedance spectrum for a 3-cm long piezoelectric fiber.
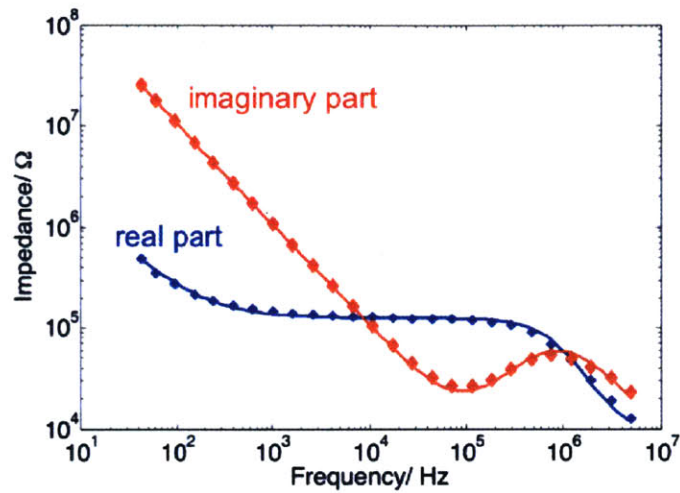
Figure 4-10: Measured (diamonds) and simulated (solid line) electrical impedance real and imaginary parts for a piezoelectric fiber.

Fitting the model derived from the equivalent circuit to these measurements leads to a set of retrieved values $[R_{contact}, R_{CPE}, f_0, \epsilon_p', \epsilon_p''] = [4 \text{ k}\Omega, 58 \text{ k}\Omega, 890 \text{ kHz}, 8.4\epsilon_0, -0.12\epsilon_0]$ for which the theoretical $\Re(Z_0(f))$ and $\Im(Z_0(f))$ (solid lines in figure 4-10)) closely match the experimental data. Furthermore, the values to which our model leads for ϵ_p' and ϵ_p'' are consistent with the literature [70]. When connected to a controlling circuit such as the one used in chapter 5, the fiber can therefore be replaced by its equivalent circuit for all predicting purposes regarding its electrical behavior in this broad range of frequencies.

78

4.3 Acoustic field shaping using single piezoelectric fibers

4.3.1 Acoustic radiation pattern

One of the compelling properties of the multimaterial fiber approach is the ability to optimize the external fiber geometry with respect to the measurement system and application. Because the fiber draw is realized in a stress and temperature regime dominated by viscous forces (as opposed to surface tension), a wide range of non-equilibrium geometries can be realized. Controlling the precise shape of the fiber allows one in principle to tailor the acoustic wave front and its associated radiation pattern in the high-frequency limit where the acoustic wavelength is smaller than the lateral dimension of the fiber. Figure 4-11 illustrates the result of simulations of the acoustic wave front emanating from two distinct fiber geometries. These calculations were performed with the finite-element simulation package COMSOL Multiphysics (version 4.2), using the Acoustics module. As shown the fiber structure and its associated acoustic wave front share the same symmetry elements.
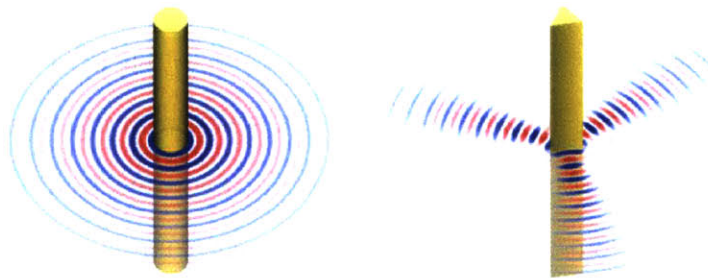
Figure 4-11: Near-field pressure patterns of the acoustic emission at 1.3 MHz from a circular fiber and a triangular fiber with cross-sectional dimensions about 2 mm.

79

We performed such acoustic radiation pattern measurements on piezoelectric fibers with a rectangular cross-section. The measurements were done in water, with a commercial piezoceramic transducer and the fiber transducer in immersion.
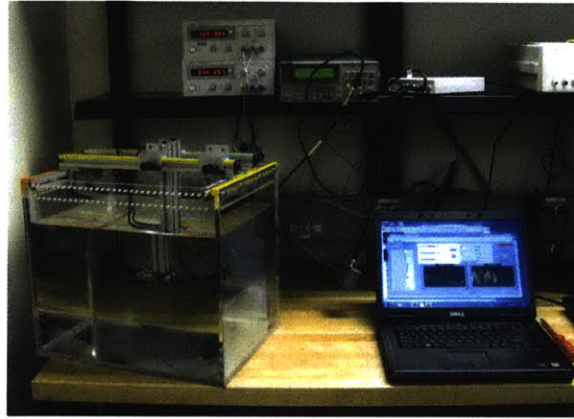
Figure 4-12: Photograph of the acoustic measurement set-up using a water-tank.

We used an Olympus immersion transducer V303-SU centered at 1 MHz and mounted on a linear motorized stage (Velmex Xslide with VXM stepping motor controller). A large water-tank (43cm x 33cm x 38cm) and time-gated signal processing were employed to minimize the interferences both from acoustic reflections on the walls of the water tank and electromagnetic coupling between the fiber and the transducer. The fiber device was mounted on a motorized rotational stage (Thorlabs CR1-Z7 with APT-dc servo controller). To measure the angular emission pattern of the fiber, we fixed the distance between the fiber and the ceramic transducer, and rotated the fiber sample a few degrees along its long axis between each measurement. Figure 4-13a shows the far-field acoustic radiation pattern of the fiber transducer at 900kHz. The observed clover-like pattern with four lobes displays a good fit with the simulations

performed using COMSOL Multiphysics (Figure 4-13b). This pattern depends on the ratio of the outer dimensions to the acoustic wavelength, and on the design of the fiber transducer. Notice how the angular widths of the lobes are inversely related to the length of the corresponding edge: the emission's directivity could thus be controlled by changing the fiber geometry.
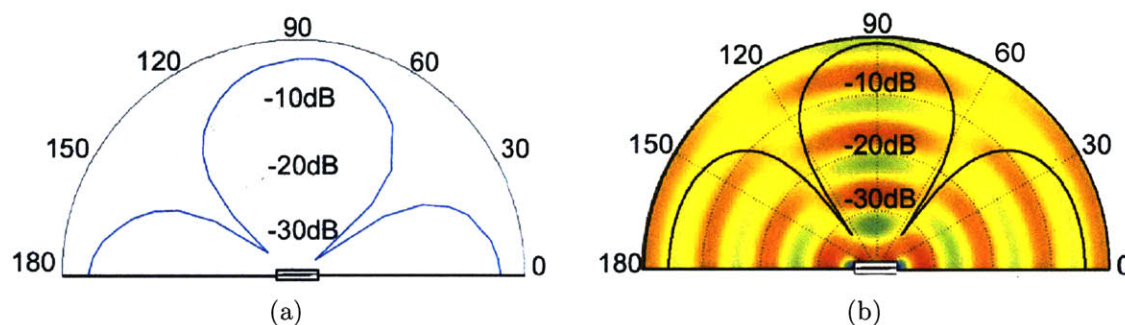
Figure 4-13: a) Acoustic radiation pattern of the piezoelectric fiber measured in water at 900kHz. b) Simulation of the far-field acoustic radiation pattern of a piezoelectric fiber in water at 900kHz.

4.3.2   Fiber bending

Another appealing and unique property of fibers is their great mechanical flexibility. While acoustic beam focusing is usually done by applying a parabolic phase difference between transducers along a linear phased array, the mechanical flexibility of the piezoelectric fibers permits an alternative approach to beam focusing using a single fiber. Indeed, by controlling the bending radius of a piezoelectric fiber, one can focus the acoustic beam at a designated distance from the fiber center. As presented in figure 4-14, the emission profile of a bent fiber transducer differs radically from that

of a straight fiber.
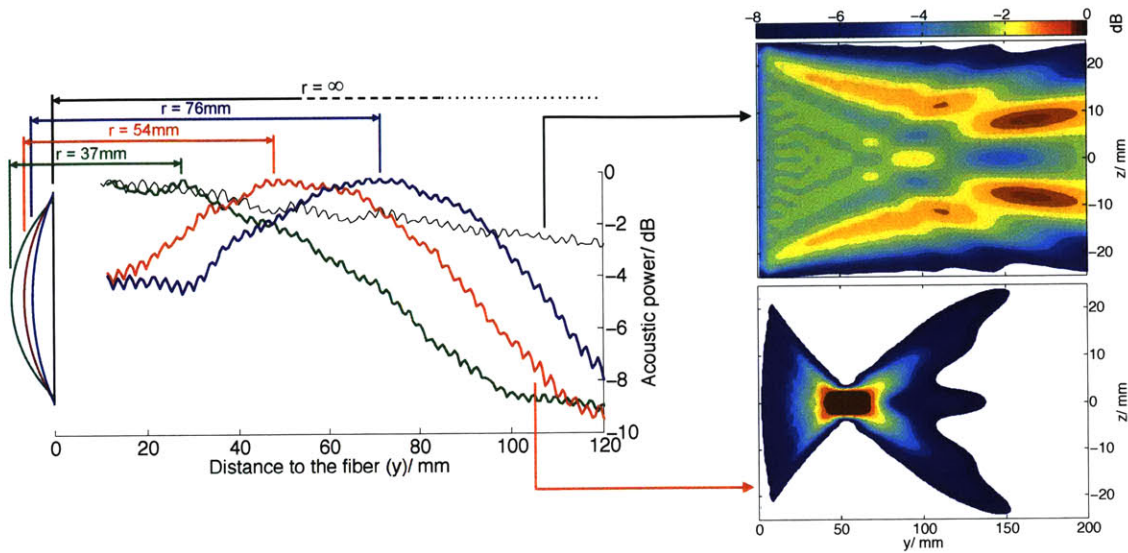
Figure 4-14: Measured acoustic power along the y-axis for different bending radii and simulations of the acoustic pressure field in the x=0 plane for a flat fiber (top) and for a fiber with bending radius equal to 54mm (bottom).

Simulations done for 5-cm long fibers emitting at 600kHz show that when the fiber is straight, the near-field region extends beyond 200mm from the fiber (top right panel). In contrast, with a bent fiber, the acoustic power is concentrated close to the fiber and is focused at a distance approximately equal to the bending radius (bottom right panel). Measurements were performed using the same underwater set-up as described in section 4.3.1, but with the piezoceramic transducer mounted on a linear stage and varying its distance to the emitting fiber. The results are shown in figure 4-14 for bending radii ranging from 37 to 76mm on a 5-cm long fiber, and compared to the emission profile of a straight fiber. These results demonstrate a clear effect of the fiber bending on the presence and location of the focal point, and

82

illustrate the potential to construct flexible acoustic devices that have capabilities beyond those of their rigid counterparts.

4.4 Improving the performance of piezoelectric fibers

4.4.1 Improving the poling process

The main difficulty in achieving high-performing piezoelectric fibers is to successfully pole them. A large fraction of piezoelectric fiber samples break-down at electric fields lower than the coercive field needed for poling. Other samples successfully support the high electric field during the poling step but subsequently depolarize over a period of a few hours to a few days (see section 3.4.3). The total fraction of fibers that short, break-down, or depolarize represents over 90% of the total number of fiber samples tested.

Several strategies can be imagined to overcome this issue. Studies on P(VDF-TrFE) have suggested that step-wise poling methods consisting of a series of pulses of electric field separated by short-circuit conditions could lead to better poling results [52]. This method would allow deformations and space charges to be relaxed, thus resulting in more homogeneous field distributions and a decreased risk for electric break-down.

Another strategy is to improve the conductivity of the viscous electrodes. While CPE has desirable properties for preform fabrication and drawing, its conductivity is only $\sim 1 \, \text{S.m}^{-1}$. As explained in section 3.4.3, this is one of the most probable

origins of the depolarization phenomenon. Moreover, as COMSOL simulation results presented in figure 4-15a show, for frequencies above 100kHz, the low conductivity of CPE causes a significant voltage drop across the width of the fiber, even though the distances involved are only on the order of hundreds of microns. Consequently, the effective electric field across the piezoelectric layer also drops (figure 4-15b). As the driving frequency further increases above 1 MHz, the electric field becomes more and more inhomogeneous across the width of the fiber. The electric field is larger at the edges of the piezoelectric layer and smaller in the center, and as a consequence the fiber effectively acts as though there were two piezoelectric devices.
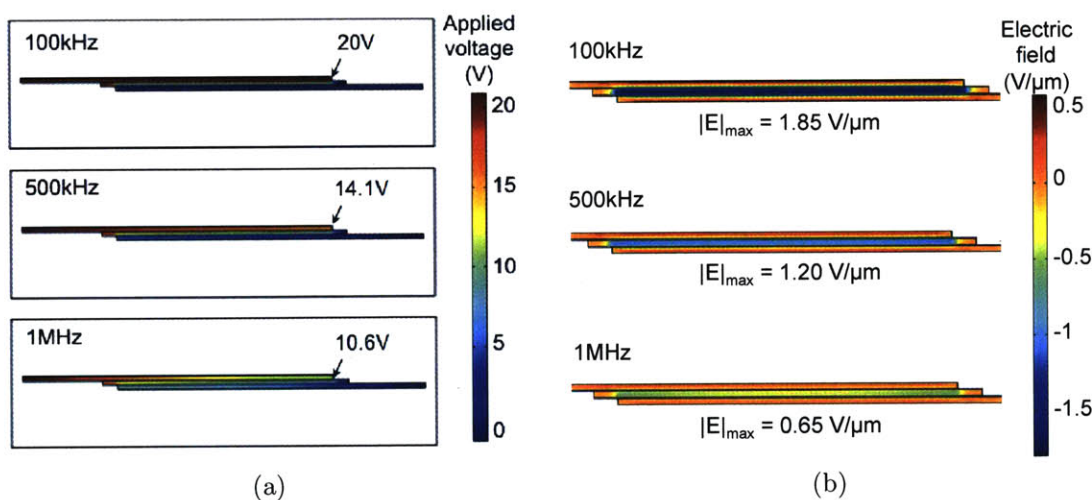
Figure 4-15: Effect of the finite conductivity of CPE as a function of frequency a) on the effective applied voltage across the electrodes and b) on the effective electric field in the piezoelectric layer.

Finally, one could improve the uniformity of the P(VDF-TrFE) layer. As explained earlier, the way to do this would be by increasing the viscosity of P(VDF-TrFE)

during the draw, i.e. by lowering the draw temperature. To achieve this, one would need to identify another cladding material with a lower glass transition temperature. A possible choice would be PMMA (acrylic), which has a glass transition temperature of 105 °C (for the homopolymer) and has been shown to be compatible with the fiber drawing process. One could also improve the uniformity of the P(VDF-TrFE) layer in the fiber by improving the uniformity of the film in the preform. Alternate film fabrication techniques such as solution casting or spin casting could lead to better film thickness uniformity and would allow a filtering step that may decrease the amount of impurities in the film.

4.4.2   Imagining a large active area architecture

While the small cross-sectional area of piezoelectric fibers enables both miniaturization and flexibility, it seemingly involves an equally small *active* area that potentially limits the fiber performance. In this section we introduce a new large-active-area fiber design that addresses a fundamental tradeoff between the requirement of maximizing the surface area of the acoustic device, and the inherent energy penalty associated with generating large area interfaces. When the transducer operates as a receiver, internal electrodes with a large surface area are desirable as they lead to a higher number of charges generated, and thus a better device sensitivity. As a transmitter, the fiber reaches maximal strain when the electric field is maximal, while remaining below the breakdown voltage. In these two regimes, the large-effective-area fiber

design introduced in this section enhances the transducer performance. Indeed, for a given cross-sectional area, a folded structure enables a several-fold increase in the electrode area and allows high electric fields without a high applied voltage since the piezoelectric layer is thinned down. This approach was developed for piezoceramic actuator stacks, and is of particular interest for use with the thermal drawing process. One of the appeals of this method is that the assembly of piezoelectric P(VDF- TrFE) layers and conductive polymer electrodes is done at the macroscopic level of the pre-form, which then yields tens of meters of fibers in a single draw. Therefore, the added cost and complexity of having multiple folded piezoelectric layers is minimal when compared to traditional layer-by-layer deposition techniques. Moreover, we expect the superior compliance and malleability of polymers over ceramics to reduce the risk of brittle failure and enable its use in tensile mode without preloading the device [71].

The structure of the large-active-area piezoelectric fibers combines sharp corners and turns, numerous interfaces between materials, and large aspect-ratio geome-tries. Therefore, part of the challenge is to slow down the kinetics of surface energy driven phenomena during the draw, so as to prevent the fiber structure from evolv-ing towards a more thermodynamically favorable geometry and to maintain a good structural integrity. Piezoelectric fibers with up to seven stacked piezoelectric layers were successfully fabricated, as shown in figures 4-16 and 4-17, proving the feasibil-ity of this approach. However, due to very large variations in power and sensitivity between fiber samples, it has not yet been possible to quantify the increase in per-formance due to an increase in number of layers.
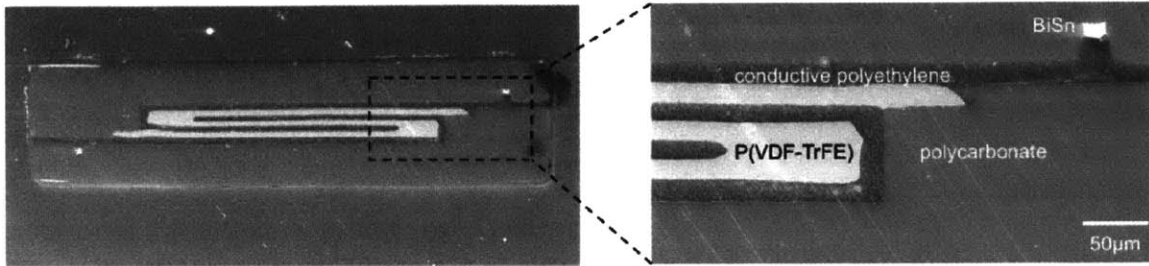
Figure 4-16: SEM micrograph of the cross-section of a 3-layer piezoelectric fiber.

Figure 4-17: Optical microscope image of the cross-section of a 7-layer piezoelectric fiber.

Chapter 5

Piezoelectric fiber arrays

5.1 Motivation

Of all the applications of piezoelectric transducers, one that has had a particularly broad impact is the development of medical ultrasonography in the 1950s. Ultrasonic imaging is one of the most important and still growing diagnostic tools in use today, and accounts for about one in four of all imaging procedures worldwide [72]. Since 1980, it has benefited from major advances in technology and has become an indispensable imaging modality, due to its flexibility and non-invasive character. It also has the advantage of being relatively cheap compared to other imaging modalities such as magnetic resonance imaging (MRI), nuclear imaging, and X-ray computed tomography (CT) [73].

Most contemporary ultrasonic scanning systems have hand-held probes comprising a

one-dimensional array of transducers. This array is electronically scanned to sweep the ultrasound beam over the volume under examination to produce an image in real-time. These systems present two major limitations. The first is related to their geometry and size. Hand-held probes require the uninterrupted presence of a physician by the patient's side, and therefore cannot be used for patient monitoring over extended periods of time. This can be a source of delay in medical decision making for critical patients. There is therefore a need for low-cost, large-area, portable ultrasound imaging systems that could provide continuous patient monitoring, identify critical conditions earlier, and thus accelerate treatment interventions. A particularly promising area of application is chest ultrasound, which has been shown in numerous studies to have exciting potential in the diagnosis of pneumothorax and in the evaluation of pulmonary edema, and which would greatly benefit from the development of a large-area flexible transducer array [74, 75].

The second limitation of traditional ultrasound systems is the one-dimensional nature of their transducer arrays, which can only produce 2D images. Yet 2D viewing of 3D anatomy presents serious limitations. The operator has to mentally combine 2D images to form a subjective impression of the 3D anatomy and pathology, which sometimes leads to incorrect decisions and inaccurate estimations of organ or tumor volume [76]. One way of producing 3D images is to have a 2D array of transducers, however the development of such 2D arrays has so far been limited by the high cost of piezoceramic transducer arrays.

In addition to medical ultrasonography, new uses of ultrasound transducers have emerged in recent years that also require large-area and addressable transducer arrays, where the amplitude and phase of each individual device can be independently controlled. These applications include photoacoustic imaging of the brain [77], bone healing [78], focused ultrasound surgery [79], and ocean observation [80].

Several approaches have been pursued to address this challenge. A specially active area of research has been electroactive polymers, which have been widely investigated as an alternative to piezoceramics [81]. In particular, the large values of piezoelectric constants for poly(vinylidene fluoride) (PVDF) and copolymers such as poly(vinylidene fluoride trifluoroethylene) (P(VDF-TrFE)), coupled with their mechanical compliance and processability make them particularly suited for large-area flexible applications. Furthermore, their large bandwidth and low acoustic impedance are an advantage for many medical uses. Another promising path involves capacitive micromachined ultrasonic transducers (CMUTs) [82]. These approaches, however, leave some key challenges unresolved: device reliability issues do to charge trapping, constraints on the device area due to wafer-based processes, acoustic cross-talk, and complex electronic integration [83].

Multimaterial piezoelectric fibers present a number of attractive properties that can address these issues. The preform-based thermal drawing process offers a scalable means of producing kilometer-long fiber devices with submillimetric cross-sectional dimensions. These long and flexible fibers can easily be assembled into large-scale

constructs, such as fabrics and sparse meshes. Their small cross-sectional dimensions also make it possible to weave them into an existing fabric to create wearable ultrasonic devices. Furthermore, monolithic integration of electrodes into the fiber enables straightforward electrical connection of the device to an external electrical circuit. In this chapter, we start by a brief review of the theory of acoustic phased arrays and its implications for the design of piezoelectric fiber arrays. We then demonstrate how piezoelectric fibers can be assembled into phased arrays and analyze collective effects in multiple fiber systems.

5.2 Theory of phased arrays

A phased array is a set of two or more transducers in which the relative phase and amplitude of each element can be independently controlled. This allows for the effective radiation pattern of the array to be electronically directed and focused in the desired direction. For example by applying a constant relative phase delay between adjacent fibers, a pattern of constructive interference is set up that results in a single wave front traveling at a set angle (figure 5-1a). This steering angle θ_s is related to the applied phase difference $\Delta\phi_s$ by the following equation:

$$\Delta\phi_s = \frac{2\pi f}{c} d \sin\theta_s \qquad (5.1)$$

where f is the frequency, d the pitch (i.e. the distance between the centers of two consecutive fibers), and c the speed of sound in water.

(a)   (b)
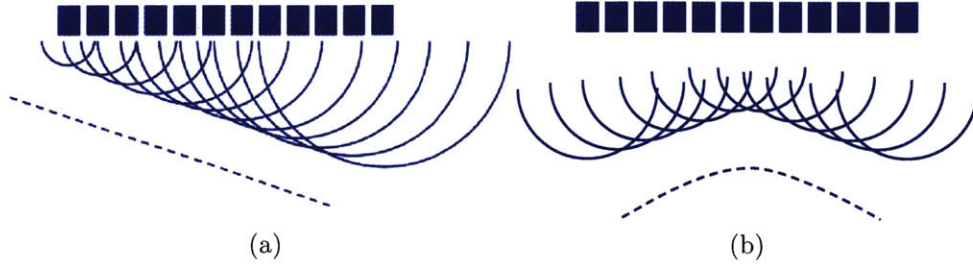
Figure 5-1: Principle of operation of a phased array. The dotted line represents the acoustic wave front. a) Beam steering: the elements are pulsed starting from the right, with a delay between each, resulting in an angled wave front. b) Beam focusing: a parabolic phase difference is applied to the array elements.

The beam can also be focused at a given distance from the array by applying a parabolic phase difference $\Delta\phi_f$ between the elements of the array (figure 5-1b):

$$\Delta\phi_f = \angle\exp\left(-j\frac{k}{2focal}x^2\right) \tag{5.2}$$

5.2.1   Radiation pattern of a single fiber

To examine the behavior of a phased array of piezoelectric fibers, it is useful to start with the radiation pattern of a single fiber. This radiation pattern can be modeled using the Huygens-Fresnel diffraction principle for a rectangular slit. This principle states that every point of the slit acts as a source of secondary wavelets and that the sum of these secondary waves determines the form of the wavefront. The superposition can be written as the following integral:

$$\Psi(r) = \frac{iA}{\lambda}\iint_{slit}\frac{\exp(-ikr)}{r}dxdy \tag{5.3}$$

93

where $\Psi(r)$ is the wave function at a distance r from the slit, (xy) is the plane of the slit, and A is the amplitude of the plane wave in the plane of the slit. In general this integral is numerically calculated, but it can be analytically solved in the far field when the Fraunhofer approximation is valid, i.e. when the following condition is satisfied:

$$r \gg \frac{a^2}{\lambda} \tag{5.4}$$

where a is the aperture dimension. A sound wave of frequency 1MHz propagating in water has a wavelength $\lambda \approx 1.5$ mm and a typical piezoelectric fiber has a width $w = $ 1mm along x and a length $L = 3$ cm along y. Therefore the Fraunhofer approximation is valid for distances greater than 60cm from the fiber. Under these conditions, after integrating and squaring equation 5.3 we obtain the following expression for the acoustic intensity:

$$I = I_0 \operatorname{sinc}^2 \left(\frac{\pi w}{\lambda} \sin \theta_x \right) \operatorname{sinc}^2 \left(\frac{\pi L}{\lambda} \sin \theta_y \right) \tag{5.5}$$

where θ_x and θ_y are the angle from the center of the fiber along x and y. The ratios w/λ and L/λ of the fiber dimensions to the wavelength determine the width of the central lobe. Since $L \gg w$, the acoustic intensity decays rapidly along y and is concentrated around the x-axis.

5.2.2 Radiation pattern of a N-fiber array

For an array of N fibers emitting in phase with a center to center separation of d along the x-axis, it can be shown that the intensity profile as a function of offset

angle from the center of the array is the following:

$$I = I_0 \, \text{sinc}^2 \left(\frac{\pi w}{\lambda} \sin \theta_x \right) \text{sinc}^2 \left(\frac{\pi L}{\lambda} \sin \theta_y \right) \left(\frac{\sin \left(\frac{N \pi d}{\lambda} \sin \theta_x \right)}{\sin \left(\frac{\pi d}{\lambda} \sin \theta_x \right)} \right)^2 \qquad (5.6)$$

It is helpful to plot this expression as a function of θ_x for different values of the parameters N, d, and λ to understand how they impact the array characteristics. Figure 5-2a shows that increasing the frequency of operation improves the focusing factor of the array. Similarly, increasing the number of elements in the array focuses the beam (figure 5-2b). This is because both increasing the frequency and increasing the number of elements in the array effectively increase the array size relative to the wavelength. Figure 5-2c shows that increasing the spacing between elements also focuses the main beam but creates undesirable side lobes.

5.3 Results and discussion

5.3.1 Experimental set-up

The phased array designed and built to drive the piezoelectric fibers combines digital and analog signal processing. Digital waveforms used to control the fiber transducers are generated in MATLAB and, using LabView, are loaded into a GP-24100 (Byte Paradigm) digital signal generator delivering a square wave. The GP-24100 is a USB device that is capable of outputting arbitrary 16-bit digital patterns at up to 100 MHz clock frequency. Each bit represents an element in the array, therefore it can theoretically be used to drive up to 16 fibers. The digital square waves are
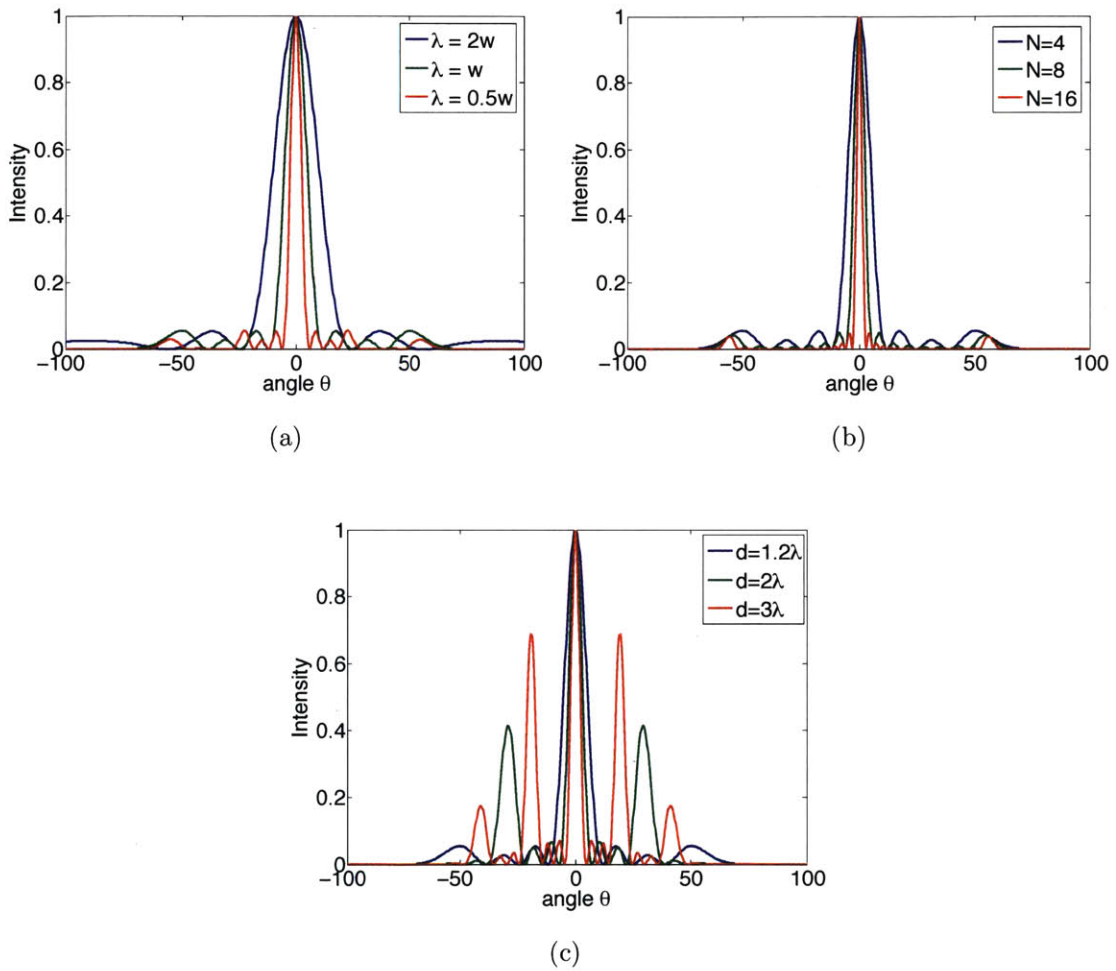
Figure 5-2: Intensity profiles as a function of angle θ for a) varying λ ($N = 4$ and $d = 1.2w$), b) varying N ($\lambda = w$ and $d = 1.2\lambda$), and c) varying d ($\lambda = w$ and $N = 4$).

then filtered by an analog chip in order to remove unwanted higher order harmonics, leaving only the desired fundamental frequency. The low pass filter chosen for this purpose is the LTC6603 (Linear Technologies), which provides a 9th order low pass filter with an adjustable cut-off frequency and gain. The analog chip was designed so that the cut-off frequency could be set to 48 kHz, 193 kHz, or 772 kHz. This cut-off frequency sets the maximum operating frequency of the array. The filtered waveforms are then amplified and applied to the fiber transducers forming the array. The amplifier has a fixed gain of 8 and a maximum operating frequency of 18 MHz. For the measurements, a driving frequency of 600kHz was selected because it laid in the overlapping region of the operational bandwidths of the commercial transducer and the analog chips.

The hardware chip comprising the low pass filter and amplifier was designed by Dan Rodgers; the schematics of the low pass filter integrated circuit and transducer driving amplifier are shown in figure 5-3 [84].

Figure 5-4 shows the experimental setup for the phased array measurement. This set-up is similar to the one described in section 4.3.1. Fibers held parallel along a vertical (Z) axis and facing the same (Y) direction are driven at 600kHz with an adjustable phase difference between consecutive fibers. The acoustic power pattern in the XZ plane is then measured with a commercial transducer at a fixed distance of 20 cm from the fibers.
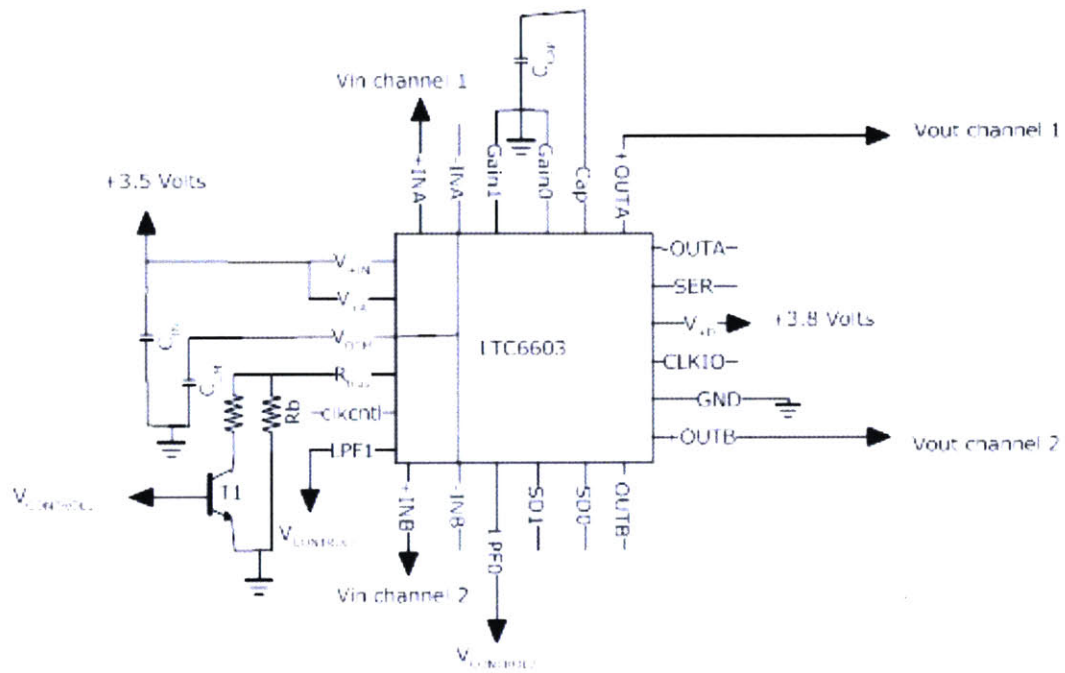
(a)
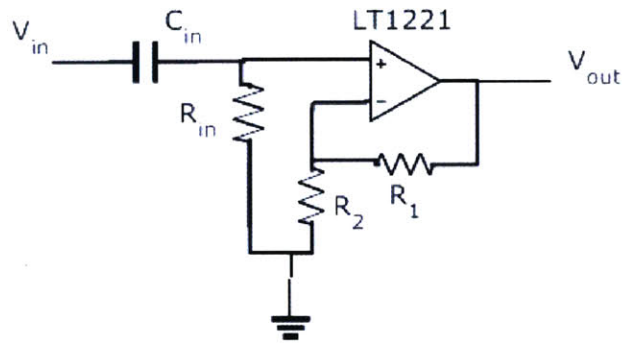
(b)

Figure 5-3: Schematics of a) the low pass filter integrated circuit and b) transducer driving amplifier.
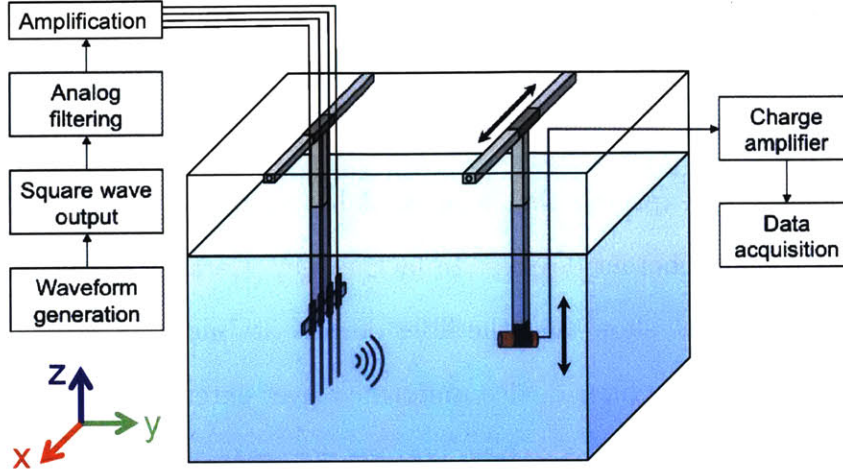
Figure 5-4: Schematic of the phased array measurement set-up.

5.3.2 Beam steering results

Figure 5-5a shows a simulated 2D map of the acoustic power generated by the inter-ference between two piezoelectric fibers driven in phase. This pattern is numerically calculated but can be analytically described for small x and z by the following diffrac-tion equation [85]:

$$P \propto \text{sinc}^2 \left(\frac{\pi w x}{\lambda y} \right) \text{sinc}^2 \left(\frac{\pi L z}{\lambda y} \right) \left(1 + \cos \left(\frac{2\pi}{\lambda} \frac{d x}{y} \right) \right) \tag{5.7}$$

where the width w and the length L of the fiber determine the slowly varying enve-lope of the radiation pattern in the X and Z directions respectively. The extended length of the fiber transducers (40 mm for the tested device) results in a rapid decay of the acoustic power along Z, and a radiation pattern that is focused around the

99

X-axis. Figure 5-5b compares the measurements with the theory for this two-fiber array in the cases where the fibers are in phase ($\Delta\phi = 0$) and out of phase ($\Delta\phi = \pi$). Since the acoustic fibers are essentially one dimensional devices and are excited from their edge, it may be expected that a phase delay would develop along their length limiting their use as coherent devices. In fact, the interference patterns between the two fibers in figure 5-5b show that the fiber devices are indeed coherent in the axial dimension, a proof of the fiber device uniformity over extended lengths.
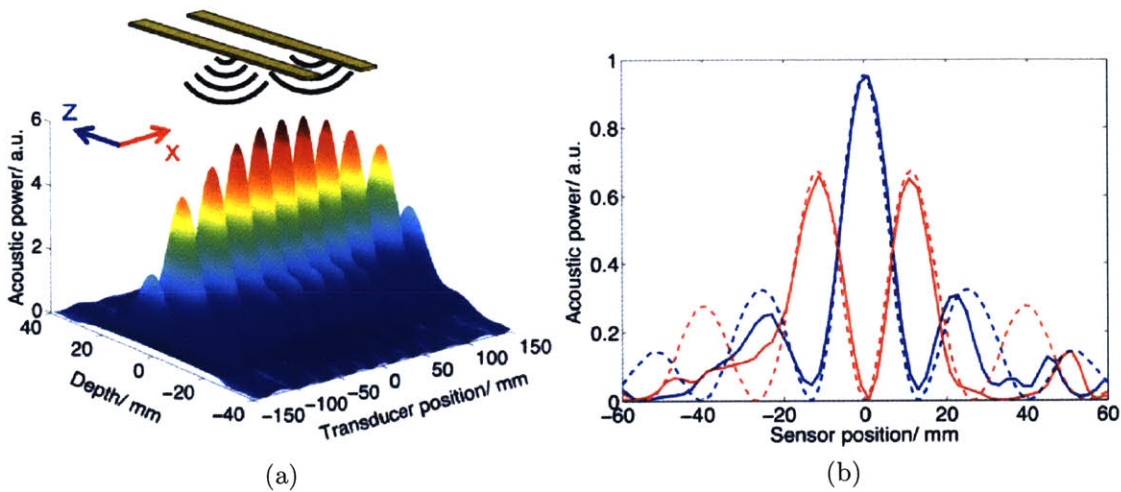
Figure 5-5: Diffraction pattern of a two-fiber array a) 3D representation of the acoustic pressure field of a two fiber array emitting in phase. b) Two fiber array: measured (solid line) and simulated (dotted line) acoustic power along x at a distance of y=20mm from the array.

The ability to control and focus acoustic energy is further improved by increasing the number of fibers being independently driven in the phased array. For example, with a four-fiber array, acoustic beam steering measurements were performed (fig-

ure 5-6). This measurement was carried out with four fibers of width 1.5 mm, a center-to-center separation (pitch) of 5 mm, for steering angles ranging from 0° to 5°. The inset shows that there is a very good fit between the expected and measured positions of the central lobe over this range of angles.
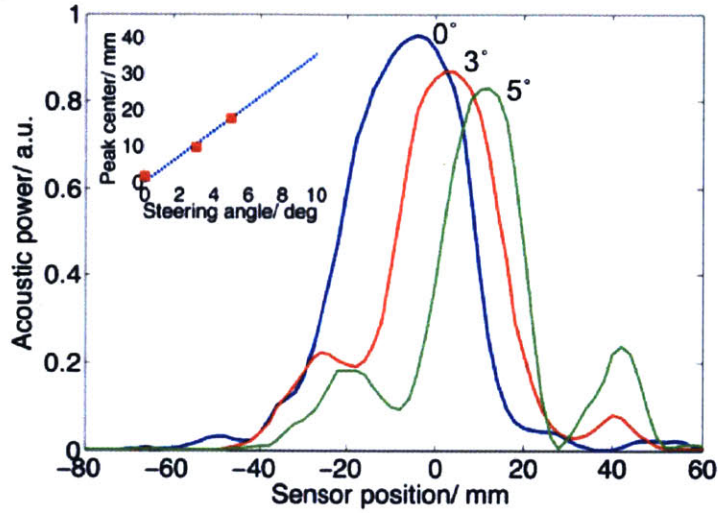
Figure 5-6: Four fiber array: measured acoustic power along x at a distance of y = 20mm from the array. Inset : main peak position as a function of the steering angle from the measurements (rectangles) and the theory (dotted line).

5.3.3 Discussion

While encouraging results were obtained at small steering angles (section 5.3.2), it has proven difficult to achieve larger steering angles. Measurements showed that as the beam was steered to angles greater than 5°, the position of the central lobe would deviate from the predicted position and its amplitude would deteriorate. This can be attributed to three sources of variations from one fiber to the other: variations

101

in emitted power, variations in pitch, and variations in orientation. Results from MATLAB calculations taking these variations into account are presented in figure 5-7) and show consequences of these variations both on the position and amplitude of the lobes.
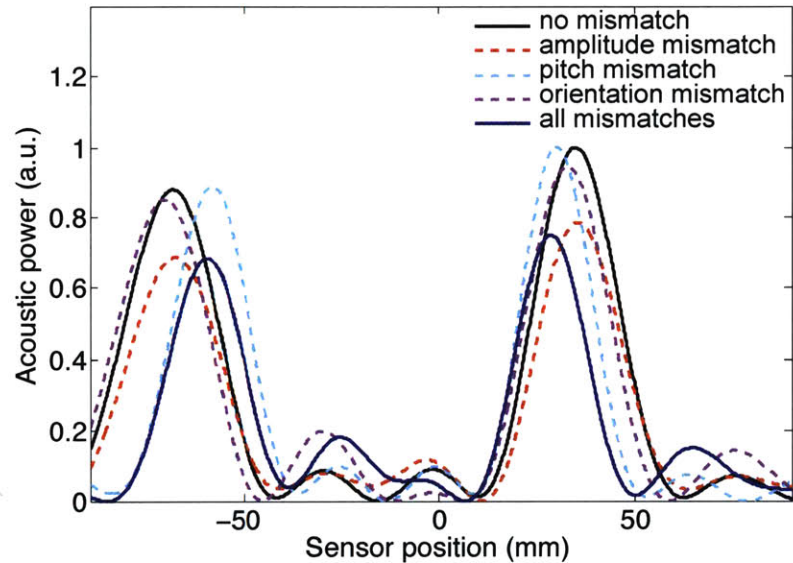
Figure 5-7: Effect on beam steering of fiber-to-fiber variations in emitted amplitude of 30% (dotted red curve), variations in pitch of 20% (dotted blue curve), and variations in fiber orientation of 15° (dotted pink curve) for a 4-fiber array operating at 600kHz and steered at 10°.

Variations in emitted power come from variations in the fiber structure and poling efficiency, and are quite large. Indeed, for the fibers used in this measurement, the individual emitting power varied by 30%. More generally, the large variations in power from one fiber sample to another and the difficulty of assembling multiple fiber samples with similar characteristics is one of the biggest limitations in realizing

larger arrays. One way to compensate for these variations in power would be to change the hardware and have an adjustable gain amplifier for each fiber. Variations in pitch and orientation are due to the difficulty in precisely positioning and clamping the fibers on the fiber holder. In the 4-fiber arrays assembled for this measurement, the pitch was equal to 5 mm, meaning that a 1 mm shift would represent a 20% deviation. Likewise, a 15° variation in fiber orientation due to loose clamping seems probable.

Another important limitation to scaling up the arrays is the electronic interface. Having a larger number of fibers in the array would enable sharper focusing and steering over a larger range of angles, but it would require a more complex hardware interface to the fibers. The current phased array system is capable of controlling up to 16 transducers in theory. However, due to the very fragile nature of the hand-soldered circuit boards, in practice only 4 transducers could be controlled. Moreover, its effective maximum operating frequency was 600 kHz, which is lower than required for most ultrasonic applications. Further work on piezoelectric phased arrays would entail building a new phased array system capable of controlling a larger number of fibers at MHz frequencies.

Chapter 6

Toward fiber electromechanical systems (FEMS)

6.1 Motivation

Although the potential for miniature machines was appreciated as early as the 1960s, most famously in Richard Feynman's seminal lecture *"There is plenty of room at the bottom"* [86], the key enabler for the realization of microelectromechanical systems (MEMS) proved to be the vast knowledge on silicon material and processing technologies developed for the integrated circuit industry in the 1970s and 1980s [87]. Applying silicon micromachining technology to mechanical devices such as cantilevers and membranes, researchers have been able to fabricate increasingly sophisticated miniaturized electromechanical transducers. Today, MEMS have extended the applications of electromechanical transduction well beyond traditional actuation and

105

motion sensing into new fields such as inkjet printing, accelerometers, drug delivery, and projection displays [88]. Thermal drawing of multimaterial fibers presents a new way of embedding devices in fibers, where fibers are not used as simple longitudinal conduits but as transverse devices that operate radially from their surface [4]. This approach opens a unique opportunity to realize electromechanical devices in a novel form. Just as their miniaturization allowed the deployment of MEMS for use in new applications, the realization of long, thin, and flexible fibers with electromechanical transduction capabilities would enable new sensing and actuating applications in inaccessible regions or over extended lengths. The recent demonstration of a piezoelectric device in fiber-form has shown the unique opportunities that could arise from the realization of fibers with electromechanical transduction capabilities [89]. The extended length, structural robustness, and flexibility of fibers lends them particularly well to coupling with the mechanical energy domain over large non-planar surfaces [12, 90], in applications such as energy harvesting or haptic displays. Furthermore, the thermal drawing process with monolithic integration of electrodes into the fiber enables straightforward connection with external electrical circuits [7].

The demonstration of a thermally drawn piezoelectric device in fiber-form was an important milestone in the development of electromechanical devices in fibers [89]. Yet, although piezoelectric materials have found uses in multiple applications ranging from hydrophones to medical imaging, typical piezoelectric strains on the order of ∼0.1% fundamentally restrict the range of mechanical strain they can undergo and limit their usefulness as actuators. While electrostriction was long considered a

higher-order nonlinear effect requiring stronger fields in most materials than typical fields used in piezoelectric materials, the emergence of a new class of highly electrostrictive materials, known as relaxor ferroelectrics, has opened the way for the use of electrostriction as an alternative to piezoelectricity for large-strain actuation applications [23]. In addition to strain capabilities of several percent, a major advantage of electrostriction over ferroelectric mechanisms is that it enables a reproducible, non-hysteretic response, with high temperature stability and absence of aging [23]. Furthermore, electrostrictors do not require high-field electrical poling, unlike ferroelectric piezoelectrics, and are more stable over time. Finally, electrostrictive materials can be used at high frequencies using their DC field-induced piezoelectric properties, and their electromechanical coefficients can be adjusted by changing the DC biasing field [25].

Here we report a novel thermally drawn fiber device with electromechanical transduction capabilities based on the integration of a highly electrostrictive relaxor ferroelectric polymer. Electromechanical actuation capabilities of this fiber device are established using high voltage atomic force microscopy (HVAFM) and a strain of 0.78% is achieved under an applied electric field of 72MV/m. The potential of this approach to realize integrated fiber electromechanical systems (FEMS) is illustrated by the fabrication of a hybrid fiber comprising an electrostrictive device and a Fabry-Perot optical filter. Amplitude modulation of the light reflected from the Fabry-Perot cavity is demonstrated at frequencies up to 10kHz through electric field induced tuning of the cavity resonance, and a modulation depth of 6.0% is reported..

6.2 Electrostrictive fiber for high strain applications

6.2.1 Materials selection

The study of relaxor ferroelectrics originated from work on perovskite structure electroceramics and has experienced an explosive growth of interest with the discovery of large, stable electrostrictive strains in lead magnesium niobate (PMN) [24]. Recently, relaxor ferroelectric behavior was discovered in a thermoplastic compatible with the thermal drawing process, poly(vinylidene fluoride trifluoroethylene) (P(VDF-TrFE)), with electrostrictive strains of more than 7% for applied electric fields of 160MV/m [91]. The theoretical value for the electric field required to achieve the same strain in piezoelectric polymers would be above 2000MV/m, a value well beyond the dielectric breakdown strengths of these materials. The large strains achievable in ferrorelaxor P(VDF-TrFE) are a result of molecular orientational changes from the all-*trans* ferroelectric phase to the paraelectric phase, which has a mixture of *trans* and *gauche* conformations.

In regular P(VDF-TrFE), this first-order phase transition occurs at temperatures above 100 °C and is accompanied by a large hysteresis, which limits its practical use [92]. By introducing defects into the polymer chains, it is possible to break the long-range polar regions into microdomains, which results in a broadening of the ferroelectric transition. This can be achieved by high-energy electrons and gamma irradiation [91] or by introducing a small amount of ternary monomer with bulky

groups such as chlorotrifluoroethylene (CTFE) and 1,1-chlorofluoroethylene (CFE) [93, 94]. The resultant modified P(VDF-TrFE) polymers are ferrorelaxors, which exhibit large electromechanical strains at room temperature with minimal hysteresis. The advantage of the terpolymer approach is that it simplifies the process, since the resultant terpolymer is inherently electrostrictive without the need for any additional step such as irradiation. Furthermore, it removes undesirable side effects caused by irradiation, such as the formation of radicals, chain scission, and cross-linking. Of all the P(VDF-TrFE)-based terpolymers, P(VDF-TrFE-CFE) has been shown to exhibit the largest electromechanical strain (table 6.1) and its use has been explored for various electromechanical applications [95]. The melting temperature of P(VDF-TrFE-CFE) is 125 °C, which is about 25° lower than the melting temperature of P(VDF-TrFE). This enables co-drawing of P(VDF-TrFE-CFE) with the same material set as P(VDF-TrFE), i.e. PC, CPE, and $Bi_{58}Sn_{42}$.

Polymer	S_M (%)	Y (GPa)
Piezo P(VDF-TrFE)	0.2	3.3
Irradiated P(VDF-TrFE)	-5	0.5
P(VDF-TrFE-CFE)	-7	0.3
P(VDF-TrFE-CTFE)	-4	0.4

Table 6.1: Electromechanical properties of modified P(VDF-TrFE) polymers [94, 96]. S_M is the maximum strain and Y is the elastic modulus.

6.2.2 Electrostrictive fiber fabrication

The P(VDF-TrFE-CFE) terpolymer was purchased in powder form from Piezotech S.A.S. (France). It has been shown that the mode of preparation of P(VDF-TrFE-CFE) films can greatly impact the microstructure and phase composition of the terpolymer [97]. The most common film formation methods are solvent casting and spin-coating, however the use of a hot press is also possible and was favored here because of its availability and ease of use. Terpolymer films were therefore prepared at $155\,^{\circ}\mathrm{C}$ under 110 bars to form 300 μm-thick films. X-ray diffraction measurements show that P(VDF-TrFE-CFE) films prepared using the hot press exhibit one narrow peak at $2\theta = 27.03\,^{\circ}$ with a lattice parameter $d = 4.89\mathring{A}$ (figure 6-1). This diffraction pattern is very different from the diffraction pattern of ferroelectric P(VDF-TrFE) (figure 3-15) and is consistent with the terpolymer being in the disordered paraelec-
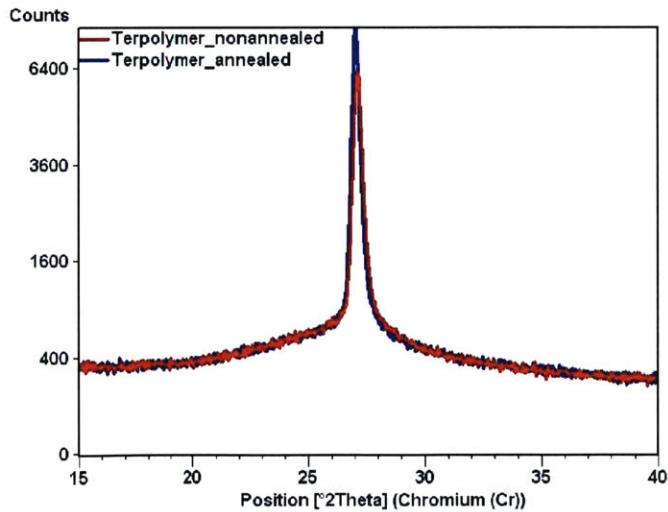
Figure 6-1: XRD measurement of P(VDF-TrFE-CFE) films before and after annealing.

tric phase [97]. We observe that annealing the terpolymer at $110\,^{\circ}$C in a vacuum for a few days slightly favors this paraelectric phase.

The terpolymer film was then assembled into a preform with 300 μm-thick CPE films, eutectic $Bi_{58}Sn_{42}$ electrodes, and PC bar cladding, and drawn into extended lengths of fiber using the procedure described section 3.3.1. SEM micrographs of the cross-section of a multimaterial electrostrictive fiber show that the device structure is well conserved during the draw (figure 6-2). The materials show good adhesion and the sharp angles in the device architecture are maintained.
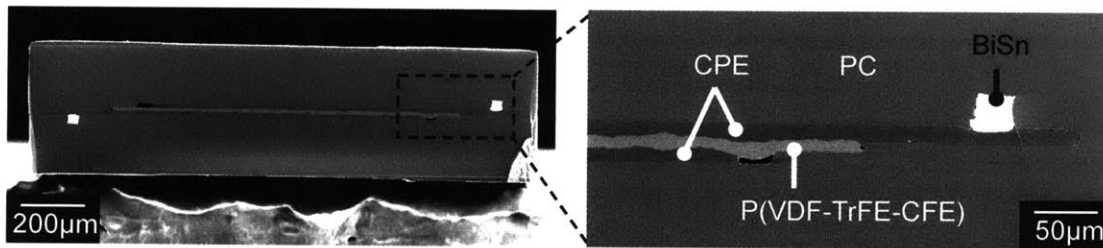
Figure 6-2: SEM micrograph of the overall structure and close-up of an electrostrictive fiber device.

6.2.3 AFM characterization

The amount of electrostrictive strain achievable in these fibers was measured using a technique based on high voltage atomic force microscopy (HVAFM). Compared to traditional techniques where the voltage is applied via the AFM tip, HVAFM has the advantage of enabling higher and more uniform applied electric fields, and its use has been demonstrated for piezoelectric coefficient measurements [98]. Compared to

traditional AFM techniques where the voltage is applied via the AFM tip, HVAFM has the advantage of enabling higher and more uniform applied electric fields. The experimental set-up is shown in figure 6-3. The fiber sample is connected to an external DC high voltage power source, and placed under an AFM (NanoScope Dimension 3000) in tapping mode. The AFM tip scans a 500 nm line on the fiber surface at a frequency on 1 Hz, with the slow-axis scan disabled. As increasing voltages are applied to the fiber through the external power source, the vertical deflection of the AFM tip is measured.
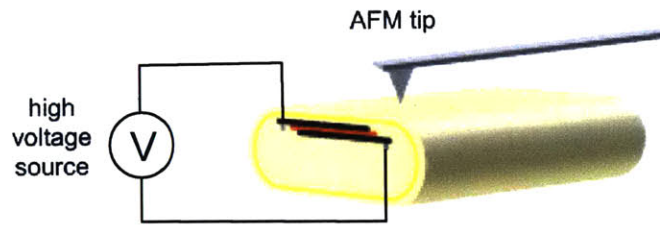
Figure 6-3: Schematic of the HVAFM set-up.

Figure 6-4 shows the AFM tip displacement at the surface of the electrostrictive fiber as increasing voltage steps are applied to the fiber through the external power source. The observed tip displacement is consistent with electric field-induced contraction of the electrostrictive layer. Relaxation phenomena in the fiber result in a different step height when the voltage is turned on and off. This measurement was performed on fibers with the electrostrictive terpolymer P(VDF-TrFE-CFE) and on poled fibers with the piezoelectric copolymer P(VDF-TrFE). The observed step heights were then plotted against the applied voltage, both normalized by the layer thickness (figure 6-5). As expected, the observed strain in the piezoelectric polymer layer is linear with the applied electric field, and their coefficient of proportionality is close to the
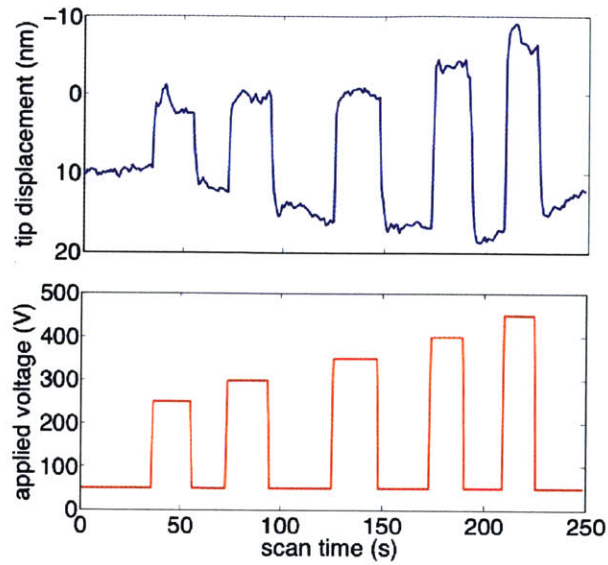
Figure 6-4: AFM tip displacement at the surface of an electrostrictive fiber under increasing applied voltage steps.
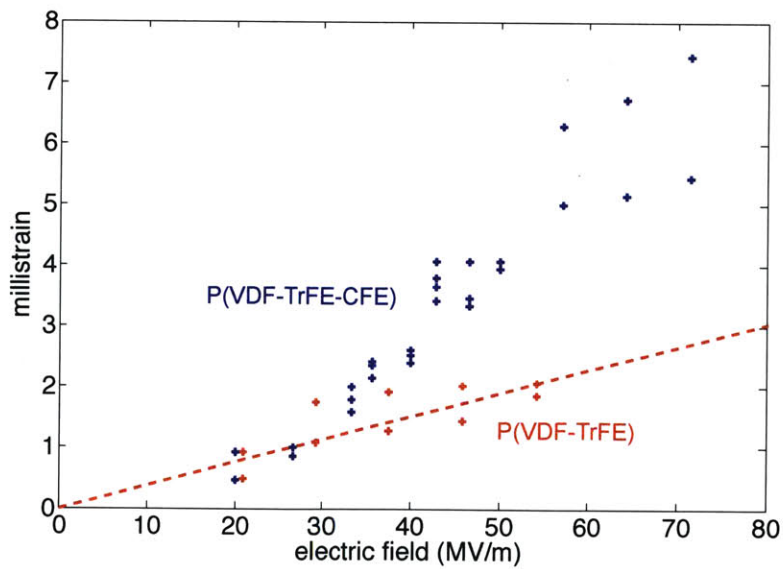
Figure 6-5: Comparison of the measured strain as a function of the applied electric field for the piezoelectric (red crosses) and electrostrictive (blue crosses) fibers. The dotted red line represents the theoretical piezoelectric strain.

113

theoretical value $d_{33} = 38\,\mathrm{pC/N}$ [32]. The strain in the electrostrictive terpolymer layer shows a non-linear dependence on the electric field. Specifically, it follows a quadratic relation for low fields and tapers off at higher fields due to polarization saturation, as is typical for thickness strain plots for P(VDF-TrFE-CFE) [94, 96]. The highest strains achieved are between 0.5% and 0.75% for electric fields between 57 MV/m and 72 MV/m (this corresponded to actual thickness changes between 35nm and 52nm on a 7μm-thick terpolymer layer).

This is considerably larger than strains achievable with piezoelectric polymers, which are on the order of 0.1%. While higher values of longitudinal strain have been reported for free-standing P(VDF-TrFE-CFE) films [96], the electrostrictive layer in the fiber is constrained in the lateral direction by the PC cladding, therefore the amount of contraction it can undergo This limits the amount of contraction possible in the thickness direction through the Poisson effect. is limited by the Poisson effect. The experimental values obtained for the fibers match very well with literature values for field-induced longitudinal strains of P(VDF-TrFE-CFE) under clamped conditions [99]. We expect higher strain rates to be achievable by changing the fiber design such that the P(VDF-TrFE-CFE) layer would be constrained in the lateral direction by a softer material, for example low density polyethylene which has a Young's modulus one order of magnitude smaller than PC. The driving voltage required to achieve a given strain can also be lowered by adopting a stacked-layer geometry [90].

6.3 Hybrid electrostrictive Fabry-Perot fiber

6.3.1 Hybrid electrostrictive Fabry-Perot fiber design

Having established the capacity of the electrostrictive layer to produce a significant amount of strain, we illustrate the potential of our approach to construct integrated MEMS in fibers by designing a hybrid fiber device that uses the electrostrictive strain to perform amplitude modulation of an optical signal. Taking advantage of the great freedom allowed by the thermal drawing method in the device materials and geometry, we construct a hybrid fiber combining a Fabry-Perot optical cavity and an electrostrictive device based on P(VDF-TrFE-CFE). The Fabry-Perot filter is based on alternating high refractive index chalcogenide glass and low refractive index polymer layers [100]. While a periodic multilayer structure leads to the formation of photonic bandgaps, i.e. ranges of frequencies with high reflectivity, the introduction of intentional deviations from periodicity allows for the creation of optical cavities [101]. Fabrication of a Fabry-Perot cavity structure in a multimaterial photonic bandgap fiber has been demonstrated by introducing an extra polymer layer in the middle of a polymer/glass multilayer structure [100]. This results in a half-wave layer surrounded by two quarter-wave stacks, and produces a Fabry-Perot resonant mode in the middle of the photonic bandgap.

Because of their sharp spectral features, Fabry-Perot filters are the basis for numerous tunable optical devices. The resonance wavelength λ_{res} is directly related to

the thickness d_{cavity} of the central polymer layer by the following equation:

$$d_{cavity} = \frac{\lambda_{res}}{2n_l} \tag{6.1}$$

As a consequence, Fabry-Perot structures are very sensitive to strain. Based on this phenomenon, a hybrid electrostrictive Fabry-Perot fiber is designed (figure 6-6).
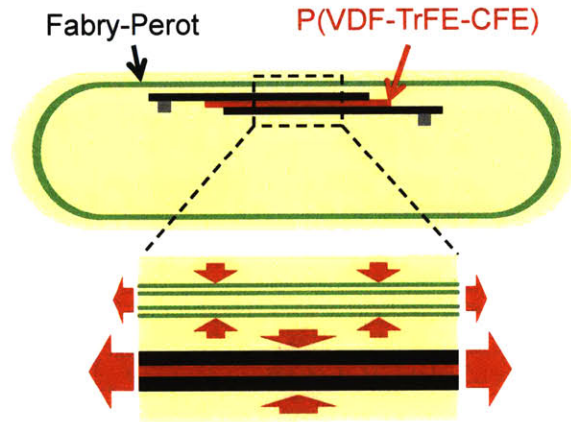
Figure 6-6: Schematic of the principle of operation of the hybrid electrostrictive Fabry-Perot fiber.

This fiber features a multilayer Fabry-Perot cavity adjacent to an electrostrictive P(VDF-TrFE-CFE) layer contacted by CPE electrodes. When a voltage is applied across the CPE electrodes, the P(VDF-TrFE-CFE) layer contracts in the thickness direction and expands in the lateral direction through the Poisson effect. This lateral strain should translate to the adjacent Fabry-Perot structure and change the thickness of the cavity, resulting in a shift of the resonance frequency (figure 6-7). At frequencies close to the resonance frequency, this shift can be used to perform amplitude modulation of the light reflected from the structure.
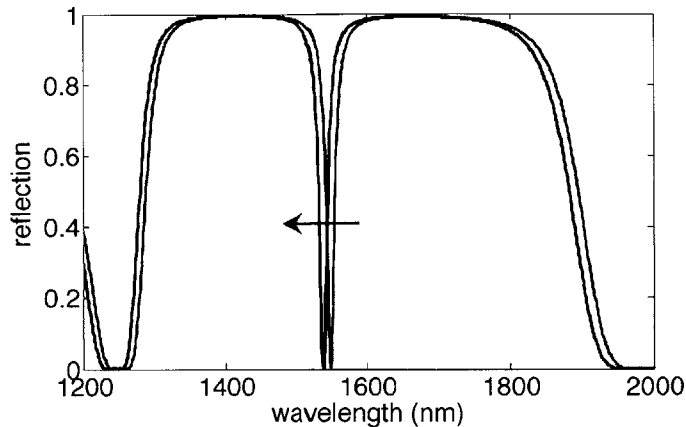
Figure 6-7: Schematic of the expected shift in Fabry-Perot resonance frequency due to a change is cavity thickness.

6.3.2 Hybrid electrostrictive Fabry-Perot fiber fabrication

Materials selection for the optical device

Previous works have investigated the optical properties of multilayer structures consisting of alternating layers of high and low refractive index materials [102, 103] and have demonstrated the possibility of incorporating them into fibers [5]. The key to successfully drawing a multilayer structure is to find a pair of materials with similar thermomechanical properties and different refractive indexes. Combinations of low-index thermoplastics and high-index amorphous semiconductors, particularly charlcogenide glasses, have been shown to successfully co-draw. Optical fibers for wavelengths from less than $1\mu m$ to over $10\mu m$ have been demonstrated with polyethylene and tellurium [104], polyethersulfone (PES) and arsenic triselenide (As_2Se_3) [6], and polyetherimide (PEI) and As_2Se_3 [105] or arsenic trisulfide (As_2S_3) [9]. More recent work has shown that while polycarbonate is incompatible to co-draw with com-

117

mercial chalcogenide glasses such as As_2S_3, increasing the sulfur content to $As_{25}S_{75}$ reduces the T_g of the glass sufficiently to co-draw with polycarbonate [106]. Since polycarbonate is the chosen cladding material for P(VDF-TrFE-CFE), we select the following materials system for the optical device: PC as the low-index material ($n_l = 1.53$ at $\lambda = 1550$nm) and $As_{25}S_{75}$ as the high-index material ($n_h = 2.27$ at $\lambda = 1550$nm).

Preform fabrication and drawing

Multilayer structures are particularly adapted to a cylindrical fiber geometry, since rolling a single polymer/glass bilayer film naturally produces a periodic stack. Electrostrictive structures, on the other hand, are more adapted to a rectangular fiber geometry. Indeed, due to its relatively low viscosity at the draw temperature, P(VDF-TrFE-CFE) cannot sustain a ring geometry. Furthermore, such a geometry would reduce the amount of deformation possible in the thickness direction by making it impossible for the polymer to expand in the other direction. The challenge is to combine these two structures in a single fiber.

There are several ways in which one could fabricate a preform with a flat multilayer structure. One approach is to simply stack bilayer films in a rectangular socket and consolidate the whole structure in the vacuum oven. This technique may seem quite straightforward, but it has in fact proven difficult to obtain a satisfactory multilayer structure in this manner, without any wrinkles or air pockets. Another approach is to pre-consolidate the multilayer stack using the hot press. The disadvantage of

this approach is that it produces residual strain in the multilayer structure, which then tends to deform when it is heated during the draw (figure 6-8). Multiple failed attempts at fabricating flat multilayer structures using these two methods revealed some of the essential qualities of the rolling method. First, it allows one to apply tension to the film while rolling, thus ensuring that the layers are tightly pressed against each other and that there is no trapped air or wrinkle. Second, it prevents the multilayer structure from deforming during the draw. Unfortunately the rolling method cannot be directly applied to a rectangular fiber because of the sharp angles. However, a slight modification of the preform edges enables a transposition of this technique to rectangular preforms.

(a) (b)
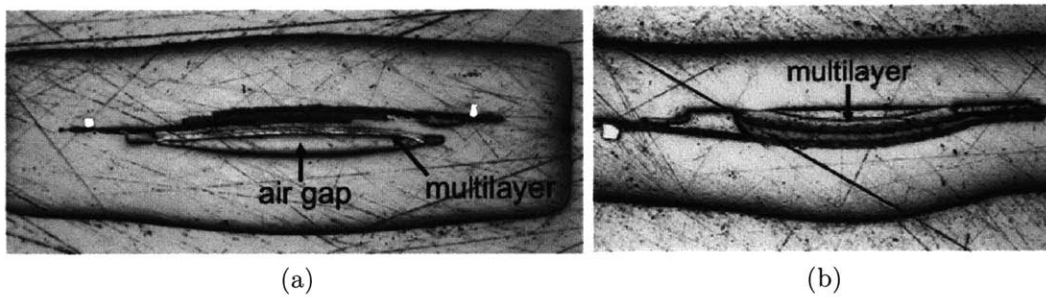
Figure 6-8: Optical micrographs of fibers with pre-pressed flat multilayer structures. The pre-pressed multilayer structure tries to shrink during the draw and causes major deformations in the fiber.

A PC/As$_{25}$S$_{75}$ bilayer film was therefore prepared using a rotating drum evaporator (figure 6-9a). As$_{25}$S$_{75}$ was synthesized in a rocking furnace using the melt-quench technique [106] and evaporated onto 10 μm-thick polycarbonate films (Lexan 104 resin) to obtain uniform glass/polymer bilayers . The thickness of the evaporated

$As_{25}S_{75}$ glass was chosen so that the quarter-wave stack condition would be met [101]:

$$\frac{d_h}{d_l} = \frac{n_l}{n_h} \qquad (6.2)$$

where d_h and d_l are the thicknesses of the glass and polymer respectively, and n_h and n_l are their index of refraction. For a PC film of thickness $d_l = 10\mu m$, the evaporated glass thickness was therefore $d_h = 10\mu m * 1.53/2.27 = 6.8\mu m$.

The preform was prepared by milling a rectangular PC slab so as to smooth its edges and obtain a rounded rectangular cross-section. The resulting slab was assembled with 300 μm-thick CPE layers, a 300 μm-thick P(VDF-TrFE-CFE) layer, small BiSn electrodes, and a 300 μm-thick CP layer at the top (figure 6-9b). The PC/glass bilayer film was then rolled around the preform (figure 6-9c). Half-way through, the film was flipped so that the central PC layer have double the thickness. The preform was then consolidated in a vacuum oven for 20 minutes at 185°C, and drawn at 230°C. During the draw, regular FTIR (Fourier-transform infrared) measurements were performed to monitor the position of the resonant wavelength of the Fabry-Perot structure. The desired thickness of the bilayer thicknesses can be calculated from the quarter-wave condition [101]:

$$d = \frac{\lambda_{res}}{4n} \qquad (6.3)$$

For $\lambda_{res} = 1550$ nm, the desired thicknesses are $d_l = 253$ nm for the PC layers and $d_h = 170$ nm for the glass layers. The expected drawdown ratio is therefore ~40.

(a)

(b)

(c)

(d)
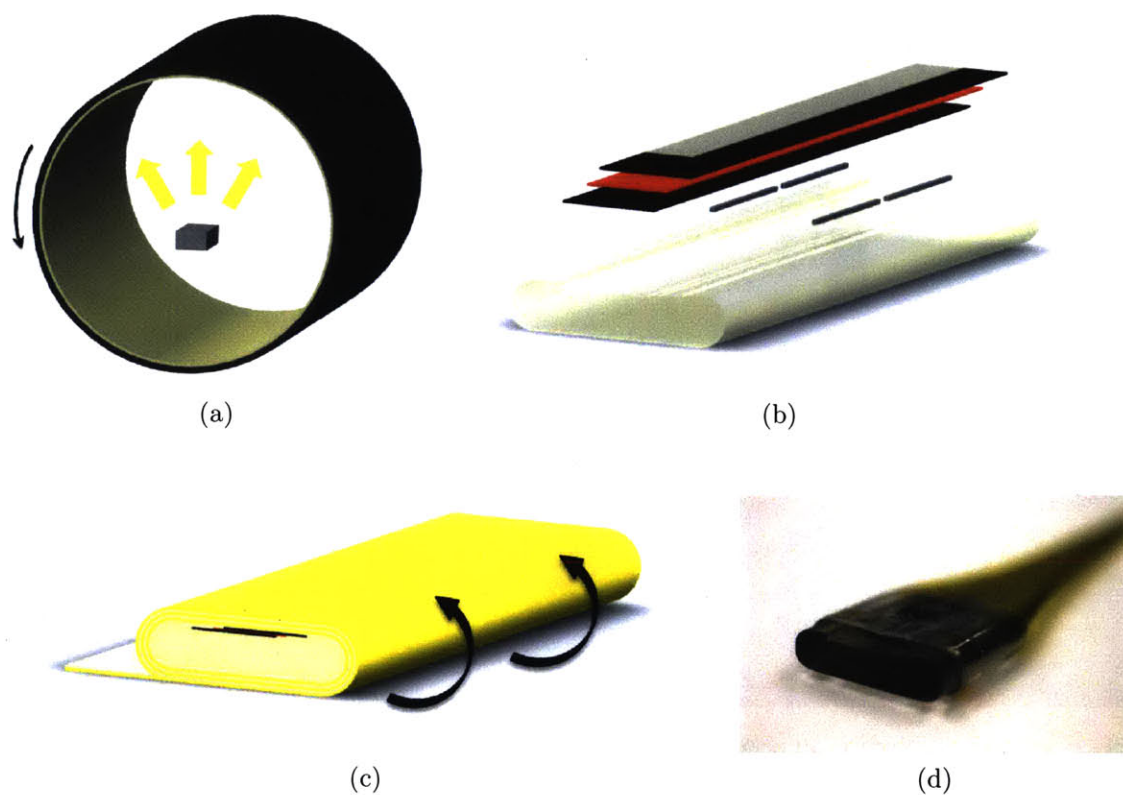
Figure 6-9: Schematic of the fabrication process of an integrated electrostrictive Fabry-Prot fiber. a) $As_{25}S_{75}$ glass is evaporated on a PC film using a rotating drum evaporator. b) The electrostrictive layer of P(VDF-TrFE-CFE) is embedded in a rounded-edge preform with CPE electrodes and metallic buses. c) The PC/$As_{25}S_{75}$ bilayer film is rolled around the preform to form a Fabry-Perot optical cavity. d) Photograph of a hybrid electrostrictive Fabry-Perot fiber preform after the draw.

SEM microscopy

SEM micrographs of the cross-section of a hybrid electrostrictive Fabry-Perot fiber show that the structure is well conserved during the draw (figure 6-10).
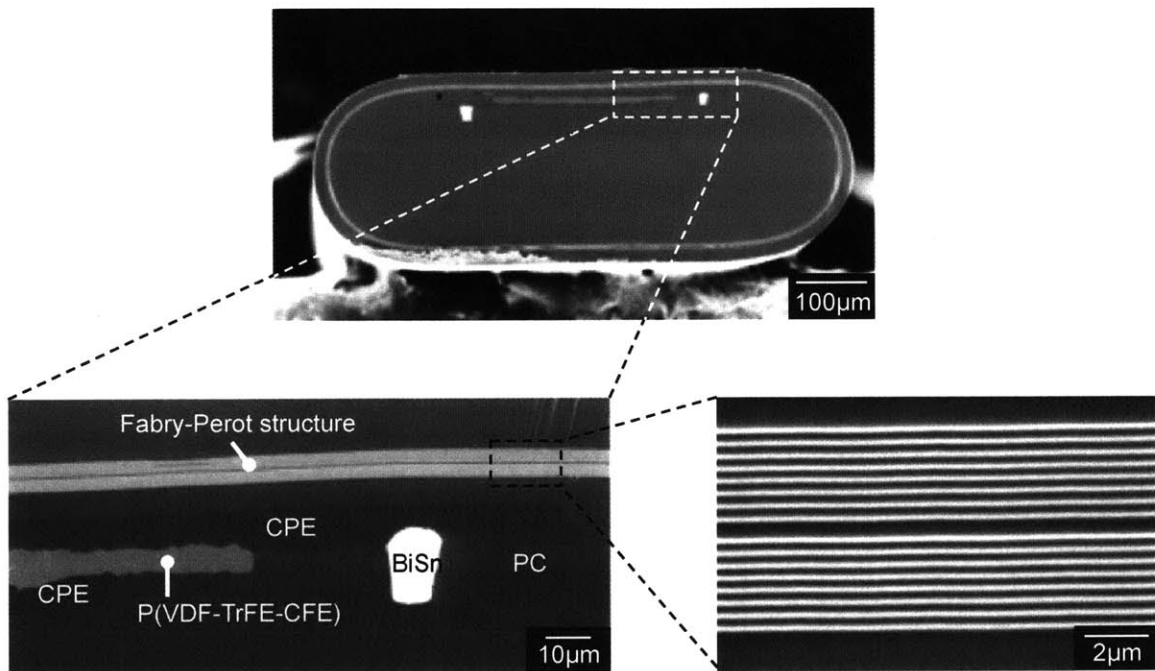
Figure 6-10: a) SEM micrograph and close-up of the cross-section of an integrated electrostrictive Fabry-Perot fiber. b) Structure of the Fabry-Perot cavity, with 8 PC/glass bilayers on each side of a PC cavity. The PC appears grey, and the $As_{25}S_{75}$ bright white.

The materials show good adhesion and the basic geometry is maintained, despite some fluctuations in the terpolymer layer thickness (see section 6.3.4). The bottom left panel of figure 6-10 shows the long-range layer uniformity of the Fabry-Perot structure and its proximity to the electrostrictive terpolymer device. The close-up in the bottom right panel reveals eight $PC/As_{25}S_{75}$ bilayers on either side of the

PC cavity. The PC layers (grey) have a thickness of $\sim$ 250 nm, and the $As_{25}S_{75}$ layers (bright) are $\sim$ 150 nm thick. A broadband fiber reflection spectrum was measured with a Fourier-transform infrared (FTIR) spectrometer (Bruker Tensor 37 spectrometer with Hyperion FTIR microscope). The result is shown in figure 6-11 and demonstrates the presence of a photonic bandgap with a resonance around 1550nm. Because the FTIR measurement uses incoherent source and contains an objective lens with a NA of 0.7, the measured spectrum is an average over a range of k-vectors, resulting in the broadening of the cavity lineshape. Transfer-matrix calculations suggest that the Fabry-Perot structures should provide a Q-factor around 800 for normal incidence.
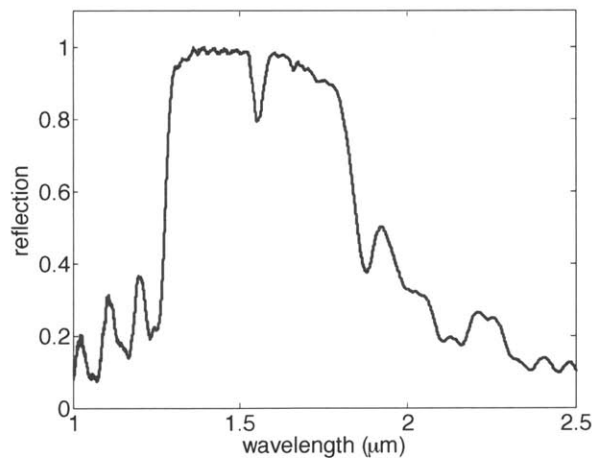
Figure 6-11: FTIR measurement of the reflection spectrum of the Fabry-Perot structure with a resonance frequency at 1558nm.

6.3.3 Simulations

Simulations of the electric-field induced strain distribution in the fiber structure were performed using the finite-element simulation package COMSOL Multiphysics (version 4.3). The results of the simulation for the static response show a complex deformation of the fiber structure (figure 6-12a). The reason for this is that while the Fabry-Perot cavity surrounds the entire fiber circumference, the electrostrictive device is restricted to the central portion of the fiber. From SEM micrographs, we determine that the active portion of the electrostrictive layer, i.e. the portion of the layer that is contacted on both sides by a CPE electrode, is ~ 200 μm wide for a total fiber width of ~ 800 μm. This central portion of the fiber (point A in figure 6-12a) behaves as expected, with a contraction of the electrostrictive layer resulting in a negative strain in the regions above and below it. However, this thickness contraction produces a lateral expansion of the electrostrictive layer due to the Poisson effect, which results in a positive strain in the lateral portions on either side of the terpolymer layer (point B in figure 6-12a). This leads to an inhomogeneous strain in the Fabry-Perot structure along the width of the fiber, with both negative and positive strain regions (figure 6-12b). Simulations of the time-harmonic response of the fiber were also performed and showed that the strain distribution is similar to the static case up to 100kHz.

These finite element simulations show that the thickness strains in the Fabry-Perot structure corresponding to an electrostrictive layer contraction of 0.5% are on the order of a few 10^{-4}. To estimate the effect of these electric-field induced strains on

124
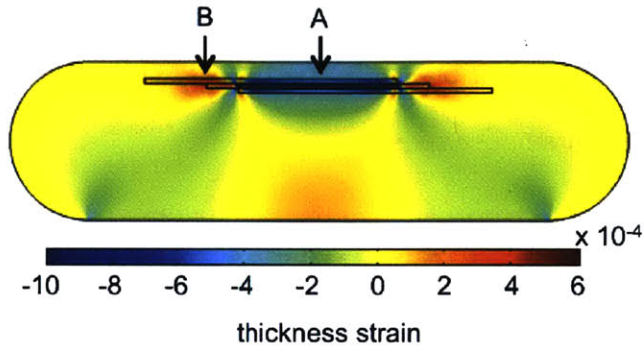
(a)
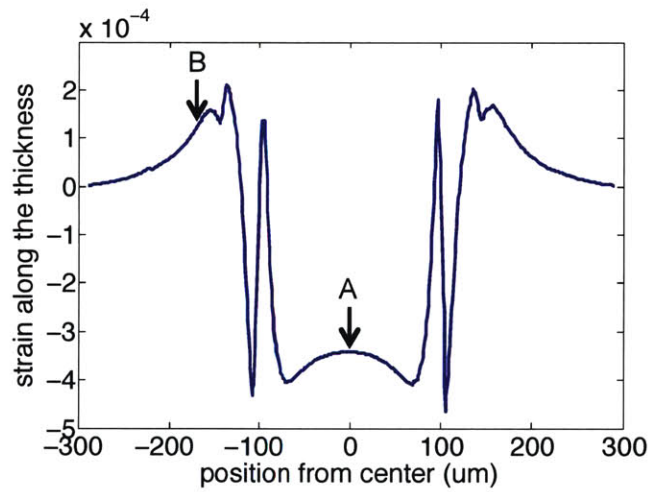
(b)

Figure 6-12: a) COMSOL simulation of the electric-field induced thickness strain in the hybrid electrostrictive Fabry-Perot fiber under an applied voltage of 300V. b) COMSOL calculation of the thickness strain in the Fabry-Perot cavity across the fiber width for a strain of 0.5% in the electrostrictive layer. The central part of the structure is under negative strain while the parts close to the fiber edges experience positive strain.

125

the resonance frequency, transfer-matrix calculations of the Fabry-Perot spectrum for points A and B were performed (MATLAB code courtesy of Dr. Alexander M. Stolyarov) [107]. The results show that the portion near the the center of the fiber (point A) should experience a blueshift of ~0.5nm, while the lateral portions (point B) should experience a smaller redshift.
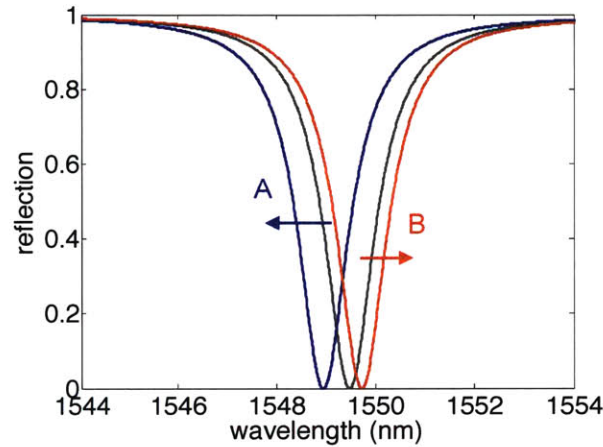
Figure 6-13: Simulation of the effect of the electric-field induced strain on the reflection spectrum of a Fabry-Perot cavity comprised of 8 PC/$As_{25}S_{75}$ bilayers on each side of a PC cavity.

6.3.4 Results and discussion

To measure these resonance shifts, an optical measurement set-up is built (figure 6-14). A tunable laser (ANDO AQ4321D 1520-1620nm) is directed onto the hybrid electrostrictive Fabry-Perot fiber, driven by an external high voltage power source. The signal reflected back from the Fabry-Perot structure is detected by a photodetector (Thorlabs PDA10CS amplified InGaAs photodetector 700-1800nm) and recorded

126

with an oscilloscope connected to a computer. A lens with focal length $f = 10$cm

was used, and the fiber and photodetector were placed at a distance $d = 20$cm from

the lens, so that the photodetector is in the image plane of the fiber. A 50μm pin-

hole was placed in front of the photodetector, restricting the recorded signal to an

illuminated area corresponding to a $\sim 50\mu$m diameter spot on the fiber surface. The

measurement is performed by sweeping the laser frequency and recording the pho-

todetector output with and without a DC applied electric field of 43 MV/m (which

corresponds to an applied voltage of 300V on a 7 μm-thick electrostrictive layer).
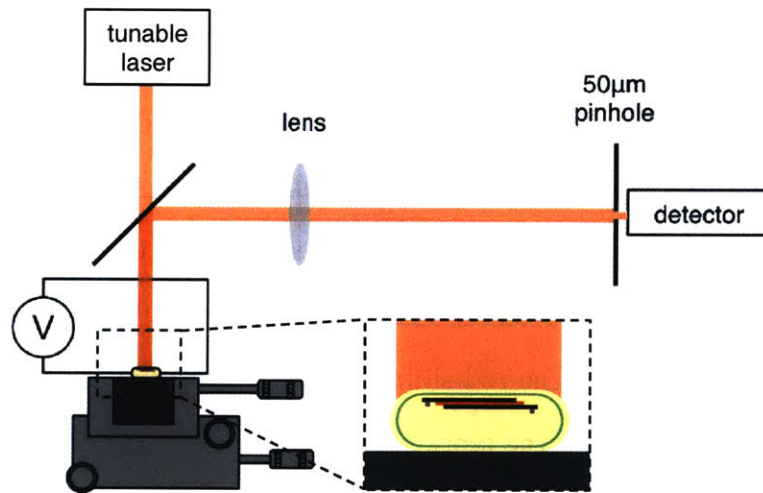
Figure 6-14: Experimental set-up for the amplitude modulation measurement.

The results are shown in figure 6-16 for two different locations on the fiber sur-

face. In both cases we observe a measurable effect of the applied electric field on the

reflection spectrum in the form of a frequency shift of the resonance. Figure 6-15a

shows a shift to shorter wavelengths, while figure 6-15b features a shift to longer

127
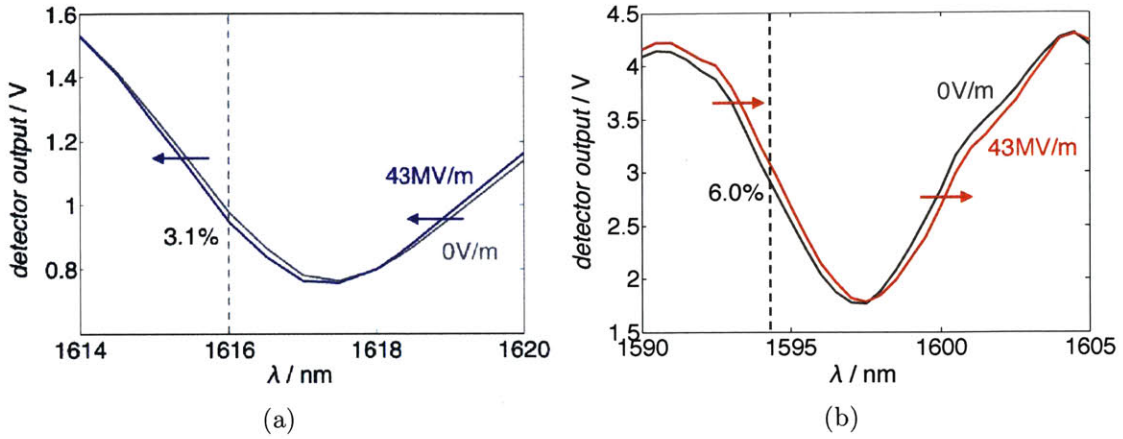
Figure 6-15: a) Electric-field induced blueshift of the Fabry-Perot resonance. b) Electric-field induced redshift of the Fabry-Perot resonance.

wavelengths, which is consistent with the simulations predicting regions of negative and positive strains in the Fabry-Perot structure. This results in a maximum modulation depth of 3.1% at 1616nm for the blue shift and 6.0% at 1594nm for the red shift. Given the simulation results, one would expect the blue shift at the center of the fiber to be larger than the red shift. However, the simulations do not take into account the non-idealities of the fabricated fiber device, in particular the fluctuations in the terpolymer layer thickness across the width of the fiber, which could explain the observed deviations from the simulated model. Further work is necessary to model the impact of these device non-idealities.

The previous measurement was repeated at a fixed location and illumination wavelength for varying driving frequencies. The results presented in figure 6-16a show the electric field-induced amplitude modulation of the reflected light for frequencies from
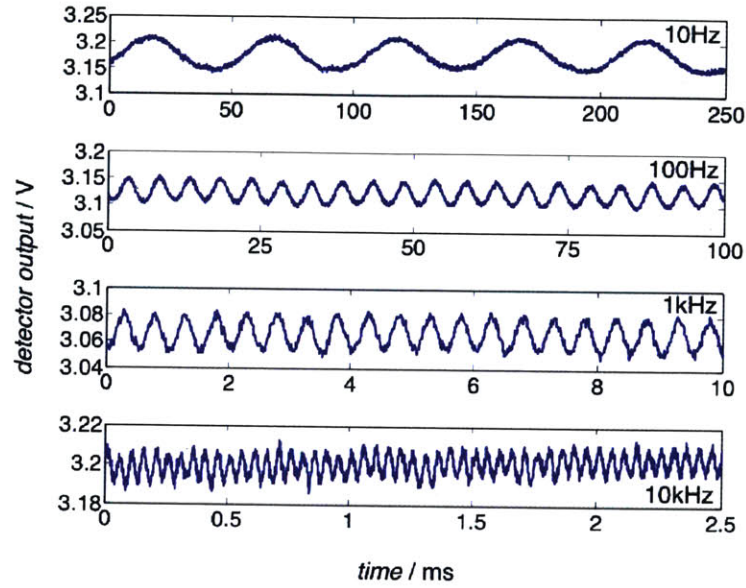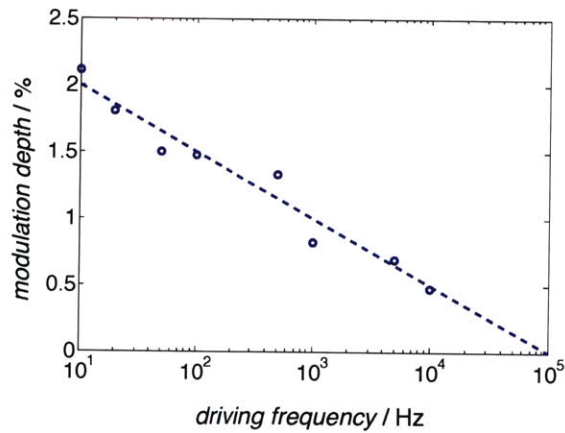
Figure 6-16: a) Measured amplitude modulation of the light reflected from the Fabry-Perot structure for different driving frequencies. b) Modulation depth as a function of the driving frequency.

10Hz to 10kHz. This establishes the capability of the hybrid fiber device to achieve amplitude modulation of an optical signal based on electromechanical transduction. As is expected in ferroelaxor polymers [108], the modulation depth decreases with frequency, corresponding to a decrease in strain response (figure 6-16b). Despite this decrease, measurable amplitude modulation is achieved at frequencies up to 10 kHz.

In addition to resonance frequency shifts, we sometimes observe overall amplitude shifts of the Fabry-Perot reflection spectrum (figure 6-17).
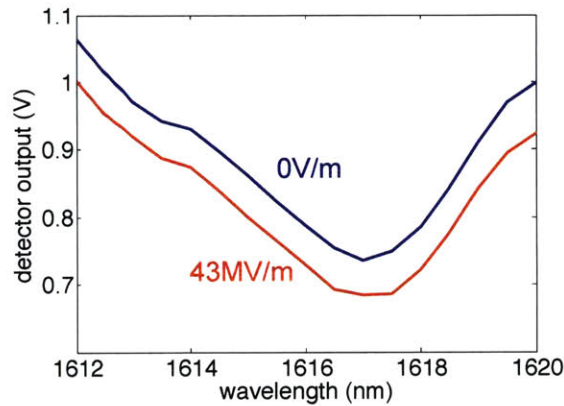
Figure 6-17: Electric-field induced overall shift in amplitude of the Fabry-Perot reflection spectrum.

A possible explanation for this amplitude shift is an electric-field induced tilt of the structure, due to non-uniform deformations of the electrostrictive layer along the fiber width. Indeed, examination of the SEM micrograph of the cross-section of the hybrid electrostrictive Fabry-Perot fiber reveals that the thickness of the terpolymer layer varies substantially across the fiber width (figure 6-18). This can be attributed to the low melting temperature and consequently low viscosity of the terpolymer

130

during the draw. Because of the non-linearity of the electrostrictive effect with respect to the electric field, such layer thickness variations will lead to non-uniform deformations of the terpolymer layer under applied voltage (figure 6-19). Thinner regions will experience a larger electric field for a given applied voltage, and therefore a larger electrostrictive coefficient leading to a larger contraction. These non-uniform contractions can then lead to local deformations and tilts of the structure.
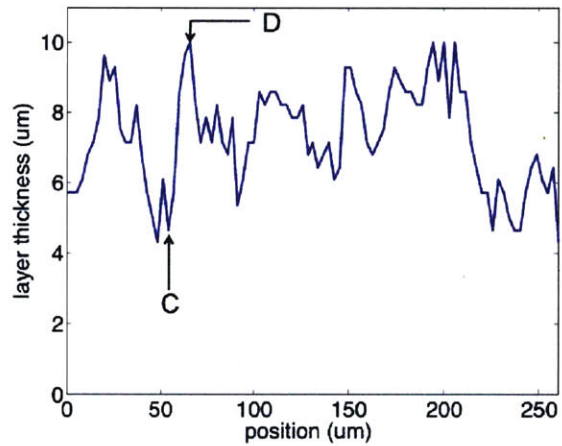
Figure 6-18: Variations of the electrostrictive terpolymer layer thickness along the width of the fiber.

Figure 6-19: Schematic of a modulation mechanism based on a change in angle of incidence.

131

Let us estimate the change in angle of incidence between points C and D in figure 6-18. The thickness at point C is 4.6 μm, which translates to an electric field of 65 V/μm under an applied voltage of 300V, and therefore an electrostrictive strain of $\sim$ 0.6% (from figure 6-5). This will result in a thickness contraction of 28 nm. The same reasoning for point D gives us a thickness of 10 μm, an electric field of 30 V/μm, a strain of $\sim$ 0.1%, and a contraction of 10 nm. Given that points C and D are $\sim$ 11.5 μm apart, this difference in thickness contraction of 17 nm will result in a change in angle of 0.08°. Transfer-matrix calculations show that a change in angle of incidence of this amplitude will not have a measurable effect on the Fabry-Perot resonance frequency. However, because the photodetector is at a distance of 40cm from the fiber, even a small change in angle of incidence can cause part of the reflected signal to not reach the detector, and therefore the output voltage to drop.

In the present case, this signal deflection is an unintended consequence of the terpolymer layer thickness non-uniformity. However, we can imagine electromechanical fiber devices designed to operate using this deflection mechanism, with controlled variations of the ferrorelaxor polymer layer thickness. By enabling electric-field induced strains and local deformation capabilities, the integration of highly electrostrictive polymers in multimaterial fibers paves the way to the realization of fiber electromechanical systems (FEMS).

6.3.5 Conclusion

We have demonstrated the first integration of a relaxor ferroelectric polymer in a fiber for electromechanical actuation. Strains up to 0.78% were achieved in the fiber device under an applied electric field of 72MV/m. The potential of this approach to realize integrated electromechanical systems in fiber form is illustrated by the fabrication of a hybrid electrostrictive Fabry-Perot fiber. Amplitude modulation of the light reflected from the Fabry-Perot cavity is demonstrated at frequencies up to 10kHz, and a maximum modulation depth of 6.0% is reported.

The integration of highly electrostrictive polymers in multimaterial fibers paves the way to the realization of fiber electromechanical systems (FEMS). Potential large surface-area applications include interactive haptic displays such as tactile Braille readers [109], color displays using tunable Fabry-Perot filters as pixel elements [110], and energy harvesting systems [111, 112]. Further applications could be enabled by integrating electrostrictive polymer devices with microfluidic channels in fibers [11], for example electrically controllable microfluidic pumps [113] and liquid-filled varifocal lenses [114].

Chapter 7

Suggested future work and conclusion

7.1 Suggested future work

There are many materials and device related studies building on this thesis work that would be of interest to carry out. The performance of the piezoelectric and electrostrictive devices described here could certainly be improved by widening the range of materials that are compatible with the thermal drawing process. One interesting direction would be to further investigate the use of composite materials. Piezoelectric fibers demonstrated for the first time the use of carbon-filled polymers as viscous electrodes in multimaterial fibers. Although graphite cannot be drawn, this has shown that graphite particles dispersed in a polymer matrix can be drawn. Many other composite materials could likewise be compatible with the draw process,

and this could be a very interesting route to incorporate high-temperature materials in polymer fibers. For example, piezoelectric composite materials have been developed, that combine a piezoceramic and a polymer matrix [115]. These composites feature both high electromechanical coupling and good acoustic impedance matching with water and are now widely used in medical ultrasound and in hydrophone systems. The incorporation of these piezoelectric composites could therefore be a way to increase the piezoelectric response of the fibers. Similarly, other composites should be explored for the viscous electrode material, for example composites combining a polymer matrix with metallic particles or carbon nano-tubes, which may have higher conductivities that carbon-loaded polymers.

The integration of ferroelectric polymers in fibers also present opportunities to study fundamental scientific questions. In particular, the subjects of polarization uniformity and depolarization in piezoelectric fibers would benefit from further exploration. An interesting tool to study these topics is piezoresponse force microscopy (PFM), a variant of atomic force microscopy which allows imaging and switching of ferroelectric domains on a sub-micrometer scale [116, 117]. This would enable a better understanding of the behavior of ferroelectric P(VDF-TrFE) in fibers and the role of polymer electrodes, and may open the way to the realization of other ferroelectric devices in fibers, such as ferroelectric-gate field effect transistors for nonvolatile data storage device applications (FRAMs).

Copolymers and terpolymers of the PVDF family have many other properties that

could be exploited to develop interesting devices in fibers. In particular, a large electrocaloric effect near room temperature has been demonstrated in P(VDF-TrFE) [118] and P(VDF-TrFE-CFE) [119]. The electrocaloric effect is a change in temperature of a material under applied electric field, and could provide a more efficient and environmentally friendly means to refrigeration compared to the traditional vapor-compression approach. The finding of large electrocaloric effects in relaxor ferroelectric polymers could therefore have potential applications in solid-state cooling and temperature regulation devices. Pyroelectricity is the physical inverse of the electrocaloric effect and is also a property of ferroelectric PVDF (ferroelectrics being a sub-class of pyroelectrics): it is the ability of a material to generate a temporary voltage upon a change in temperature. The pyroelectric properties of PVDF and its copolymers are widely used, for example in infrared detection, infrared spectroscopy, gas analysis, and thermal imaging [30], all of which are applications which could lead to interesting devices in fiber form. Due to their dielectric constants which are larger than that of most polymers, PVDF-based polymers have attracted a lot of interest for capacitors and energy storage systems [120]. Copolymers of PVDF with chlorotrifluoroethylene (CTFE) and hexafluoropropylene (HFP) in particular have shown energy densities higher than 25 J.cm^{-3} [120, 121]. These high energy densities combined with their light weight, fast discharge speed, low cost, and graceful failure make them particularly interesting materials for energy storage capacitors. In fact, the development of high energy density capacitive fibers using PVDF-based polymer films in a multi-stack design fiber is a current topic of investigation [122]. Finally, the use of PVDF copolymers and terpolymers for energy harvesting is also an active

area of research [111, 112]. Being able to fabricate a power-source in fiber form would be great step toward fully integrated functional fabrics.

Interesting applications can also be imagined by taking advantage of the integration capabilities of the multimaterial fiber approach. By combining a piezoelectric device with an optical device in a fiber, acousto-optic effects could be studied. Another interesting research direction is the integration of an electromechanical device with a porous membrane in a fiber, to achieve controlled drug release using acoustic waves through mechanisms such as phase changes, acoustic radiation pressure, acoustic streaming, or acoustic cavitation.

7.2   Conclusion

The heart of this thesis has been to establish the possibility of electromechanical transduction in fibers and to explore some of the applications of these new fiber devices. For the first time, thermal drawing of a piezoelectric device was achieved, resulting in tens of meters of multimaterial acoustic fiber. The challenges associated with the fabrication of a piezoelectric fiber were analyzed from a materials perspective, with particular attention to the relationship between the processing steps and the material properties. Careful characterization of the piezoelectric fiber device was performed using acoustic, optical, and electrical techniques, and establishing the piezoelectric response of the device over a wide range of frequencies, from kHz to MHz. Several unique features of fiber devices were explored, such as their great

mechanical flexibility and the ability to design them arbitrary cross-sectional geometries. Collective effects in multi-fiber constructs were also discussed. Finally, high strain actuation capabilities in a fiber were demonstrated based on the integration of a highly electrostrictive relaxor ferroelectric polymer. The possibility of integrating multiple devices in a single fiber was illustrated by the fabrication of a hybrid electrostrictive Fabry-Perot fiber and its use for optical amplitude modulation. This work paves the way to the realization of integrated fiber electromechanical devices (FEMS) and could have wide ranging applications in fields such as acoustics, acousto-optics, electromechanical systems, sensing technologies, and large-area flexible systems.

Bibliography

[1] Kvavadze, E. *et al.* 30,000-year-old wild flax fibers. *Science* **325**, 1359 (2009).

[2] Russell, P. Photonic crystal fibers. *Science* **299**, 358–362 (2003).

[3] Knight, J. C. Photonic crystal fibres. *Nature* **424**, 847–851 (2003).

[4] Abouraddy, A. F. *et al.* Towards multimaterial multifunctional fibres that see, hear, sense and communicate. *Nature Materials* **6**, 336–347 (2007).

[5] Fink, Y. *et al.* Guiding optical light in air using an all-dielectric structure. *J. Lightwave Technol.* **17**, 2039–2041 (1999).

[6] Hart, S. D. *et al.* External reflection from omnidirectional dielectric mirror fibers. *Science* **296**, 510–513 (2002).

[7] Bayindir, M. *et al.* Metal-insulator-semiconductor optoelectronic fibres. *Nature* **431**, 826–829 (2004).

[8] Bayindir, M., Abouraddy, A., Arnold, J., Joannopoulos, J. & Fink, Y. Thermal-sensing fiber devices by multimaterial codrawing. *Advanced Materials* **18**, 845–+ (2006).

[9] Shapira, O. *et al.* Surface-emitting fiber lasers. *Optics Express* **14**, 3929–3935 (2006).

[10] Danto, S. *et al.* Fiber Field-Effect device via in situ channel crystallization RID b-9804-2009. *Advanced Materials* **22**, 4162–4166 (2010).

[11] Stolyarov, A. M. *et al.* Microfluidic directional emission control of an azimuthally polarized radial fibre laser. *Nature Photonics* **6**, 229–233 (2012).

[12] Abouraddy, A. *et al.* Large-scale optical-field measurements with geometric fibre constructs. *Nature Materials* **5**, 532–536 (2006).

[13] Sorin, F. *et al.* Exploiting collective effects of multiple optoelectronic devices integrated in a single fiber. *Nano Letters* **9**, 2630–2635 (2009).

[14] Danto, S., Ruff, Z., Wang, Z., Joannopoulos, J. D. & Fink, Y. Ovonic memory switching in multimaterial fibers RID b-9804-2009. *Advanced Functional Materials* **21**, 1095–1101 (2011).

[15] Bayindir, M. *et al.* Integrated fibres for self-monitored optical transport. *Nature Materials* **4**, 820–825 (2005).

[16] Newnham, R. E., Sundar, V., Yimnirun, R., Su, J. & Zhang, Q. M. Electrostriction: nonlinear electromechanical coupling in solid dielectrics. *The Journal of Physical Chemistry B* **101**, 10141–10150 (1997).

[17] Curie, J. & Curie, P. Développement par compression de l'électricité polaire dans les cristaux hemièdres à faces inclinées. *C. R. Acad. Sci. Paris* **91**, 294–295 (1880).

[18] Royer, D. & Dieulesaint, E. *Elastic Waves in Solids* (Springer-Verlag Berlin Heidelberg, 2000).

[19] Nye, J. F. *Physical Properties of Crystals: Their Representation by Tensors and Matrices* (Oxford University Press, 1985).

[20] Carpi, F. & Smela, E. *Biomedical Applications of Electroactive Polymer Actuators* (John Wiley and Sons, 2009).

[21] Kay, H. F. Electrostriction. *Reports on Progress in Physics* **18**, 230 (1955).

[22] Sundar, V. & Newnham, R. E. Electrostriction and polarization. *Ferroelectrics* **135**, 431 (1992).

[23] Cross, L. E., Jang, S. J., Newnham, R. E., Nomura, S. & Uchino, K. Large electrostrictive effects in relaxor ferroelectrics. *Ferroelectrics* **23**, 187–191 (1980).

[24] Smolensky, G. A. & Agranovskaya, A. I. Dielectric polarization of a number of complex compounds. *Sov. Phys. Solid State* **1**, 1429–1437 (1959).

[25] Chen, J., Shurland, A., Perry, J., Ossmann, B. & Gururaja, T. R. Electrostrictive transducers for medical ultrasonic applications. In *Proceedings of the Tenth IEEE International Symposium on Applications of Ferroelectrics, 1996. ISAF '96*, vol. 1, 27–30 (1996).

[26] Kawai, H. Piezoelectricity of poly (vinylidene fluoride). *Jpn. J. Appl. Phys.* **8**, 975–976 (1969).

[27] Bergman, J. G., McFee, J. H. & Crane, G. R. Pyroelectricity and optical second harmonic generation in polyvinylidene fluoride films. *Applied Physics Letters* **18**, 203 (1971).

[28] Nakamura, K. & Wada, Y. Piezoelectricity, pyroelectricity, and the electrostriction constant of poly(vinylidene fluoride). *Journal of Polymer Science Part A-2: Polymer Physics* **9**, 161–173 (1971).

[29] Lovinger, A. J. Ferroelectric polymers. *Science* **220**, 1115–1121 (1983).

[30] Lang, S. B. & Muensit, S. Review of some lesser-known applications of piezo-electric and pyroelectric polymers. *Applied Physics A* **85**, 125–134 (2006).

[31] Gerhard-Multhaupt, R. Less can be more: Holes in polymers lead to a new paradigm of piezoelectric materials for electret transducers. *IEEE Transactions on Dielectrics and Electrical Insulation* **9**, 850–859 (2002).

[32] Measurement Specialties, Inc., Norristown, PA. *Piezo Film Sensors Technical Manual.*

[33] Gregorio, R. & Botta, M. M. Effect of crystallization temperature on the phase transitions of p(vdf/trfe) copolymers. *JPS* **36** (1998).

[34] Rayleigh, L. On the instability of jets. *Proc. London. Math. Soc.* **10**, 4–13 (1878).

[35] Deng, D. S. *et al.* In-Fiber semiconductor filament arrays. *Nano Letters* **8**, 4265–4269 (2008).

[36] Tomotika, S. On the instability of a cylindrical thread of a viscous liquid surrounded by another viscous fluid. *Proc. R. Soc. London A* **150**, 322–337 (1935).

[37] Hart, S. D. *Multilayer composite photonic bandgap fibers.* Ph.D. thesis, MIT (2004).

[38] Deng, D. S., Nave, J. C., Liang, X., Johnson, S. G. & Fink, Y. Exploration of in-fiber nanostructures from capillary instability. *Optics Express* **19**, 16273–16290 (2011).

143

[39] Huang, J. Carbon black filled conducting polymers and polymer blends. *Advanced in Polymer Technology* **21**, 299–313 (2002).

[40] Xi, B. & Chen, G. The mechanism of electrical conduction in polyethylene/carbon black composite. In *Proceedings of the 6th International Conference on Properties and Applications of Dielectric Materials, 2000*, vol. 2, 1015–1018 (IEEE, 2000).

[41] Jaeger, K. M., McQueen, D. H., Tchmutin, I. A., Ryvkina, N. G. & Klüppel, M. Electron transport and ac electrical properties of carbon black polymer composites. *Journal of Physics D: Applied Physics* **34**, 2699–2707 (2001).

[42] Das, N., Chaki, T. & Khastgir, D. Effect of axial stretching on electrical resistivity of short carbon fibre and carbon black filled conductive rubber composites. *Polymer International* **51**, 156–163 (2002).

[43] Sorin, F., Lestoquoy, G., Danto, S., Joannopoulos, J. D. & Fink, Y. Resolving optical illumination distributions along an axially symmetric photodetecting fiber. *Optics Express* **18**, 24264–24275 (2010).

[44] Koga, K. & Ohigashi, H. Piezoelectricity and related properties of vinylidene fluoride and trifluoroethylene copolymers. *Journal of Applied Physics* **59**, 2142–2150 (1986).

[45] Giurgiutiu, V. & Lyshevski, S. E. *Micromechatronics: modeling, analysis, and design with MATLAB* (CRC Press, Taylor Francis Inc., United States, 2009).

[46] Furukawa, T. Ferroelectric properties of vinylidene fluoride copolymers. *Phase Transitions* **18**, 143–211 (1989).

[47] Mehta, R. R., Silverman, B. D. & Jacobs, J. T. Depolarization fields in thin ferroelectric films. *Journal of Applied Physics* **44**, 3379–3385 (1973).

[48] Benedetto, J. M., Moore, R. A. & McLean, F. B. Effects of operating conditions on the fast-decay component of the retained polarization in lead zirconate titanate thin films. *Journal of Applied Physics* **75**, 460–466 (1994).

[49] Waser, R., Boettger, U. & Tiedke, S. *Polar Oxides: Properties, Characterization, and Imaging* (John Wiley and Sons, 2006).

[50] Park, Y. J., Chang, J., Kang, S. J. & Park, C. Polarization retention of thin ferroelectric poly(vinylidene fluoride-co-trifluoroethylene) film capacitors. *Applied Physics Letters* **95**, 102902 (2009).

[51] Kim, W. Y. Retention performance of ferroelectric polymer film for nonvolatile memory devices. *IEEE Electron Device Letters* **30**, 822–824 (2009).

[52] IEEE (ed.). *Poling of VDF/TrFE copolymers using a step-wise method* (1996).

[53] Gruverman, A. *et al.* Spatial inhomogeneity of imprint and switching behavior in ferroelectric capacitors. *Applied Physics Letters* **82**, 3071–3073 (2003).

[54] Sussner, H. & Dransfeld, K. Importance of the metal-polymer interface for the piezoelectricity of polyvinylidene fluoride. *Journal of Polymer Science Part B: Polymer Physics* **16**, 529–543 (1978).

[55] Eisenmenger, W. & Haardt, M. Observation of charge compensated polarization zones in polyvinylidene fluoride (pvdf) films by piezoelectric acoustic step-wave response. *Solid State Communications* **41**, 917–920 (1982).

[56] von Seggern, H. & Fedosov, S. N. Conductivity-induced polarization buildup in poly(vinylidene fluoride). *Applied Physics Letters* **81**, 2830–2832 (2006).

[57] Wurfel, P. & Batra, I. P. Depolarization-field-induced instability in thin ferroelectric films: experiment and theory. *Physical Review B* **8**, 5126–5133 (1973).

[58] Ambrosy, A. & Holdik, K. Piezoelectric pvdf films as ultrasonic transducers. *J. Phys. E: Sci. Instrum.* **17**, 856 (1984).

[59] Cheeke, J. D. N. *Fundamentals and Applications of Ultrasonic Waves* (CRC Press, 2002).

[60] Nicholls, S. J. *et al.* Application of intravascular ultrasound in anti-atherosclerotic drug development. *Nature Reviews Drug Discovery* **5**, 485–492 (2006).

[61] Yoon, H. J., Jung, J. M., Jeong, J. S. & Yang, S. S. Micro devices for a cerebrospinal fluid shunt system. *Sensors and Actuators A* **110**, 68–76 (2004).

[62] Schaefer, W. *et al.* Good urodynamic practices: uroflowmetry, filling cystometry, and pressure-flow studies. *Neurourology and Urodynamics* **21**, 261–274 (2002).

[63] Pinet, E. Medical applications: Saving lives. *Nature Photonics* **2**, 150–152 (2008).

[64] Mitragotri, S. Healing sound: the use of ultrasound in drug delivery and other therapeutic applications. *Nature Reviews Drug Discovery* **4**, 255–260 (2005).

[65] Arnau, A. *Piezoelectric transducers and applications* (Springer, 2008).

[66] Morrison, R. *Grounding and Shielding: Circuits and Interference* (IEEE Press, 2007).

[67] Eberhardt, F. J. & Andrews, F. A. Laser heterodyne system for measurement and analysis of vibration. *J. Acoust. Soc. Am.* **48**, 603–609 (1970).

[68] Huber, R., Wojtkowski, M., Taira, K., Fujimoto, J. G. & Hsu, K. Amplified, frequency swept lasers for frequency domain reflectometry and oct imaging: Design and scaling principles. *Optics Express* **13**, 3513–3528 (2005).

[69] Kawamoto, H. *Carbon Black-Polymer Composites, The Physics of Electrically-Conducting Composites* (Marcel Dekker, New York, 1982).

[70] Gregorio, R. & Ueno, E. Effect of crystalline phase, orientation and temperature on the dielectric properties of poly (vinylidene fluoride) (pvdf). *J. Mater. Sci.* **34**, 4489–4500 (1999).

[71] Flint, E., Liang, C. & Rogers, C. A. Electromechanical analysis of piezoelectric stack active member power consumption. In *Proceedings of the Second International Conference on Intelligent Materials*, 534–545 (CRC Press, Colonial Williamsburg, Virginia, U.S.A., 1994).

[72] Wells, P. N. T. Ultrasound imaging. *Physics in Medicine and Biology* **51**, 83–98 (2006).

[73] Shung, K. K. & Zipparo, M. Ultrasonic transducers and arrays. *IEEE Engineering in Medicine and Biology* **15**, 20–30 (1996).

[74] Lichtenstein, D. A. & Menu, Y. A bedside ultrasound sign ruling out pneumothorax in the critically ill - lung sliding. *Chest* **108**, 1345–1348 (1995).

[75] Agricola, E. *et al.* "ultrasound comet-tail images": A marker of pulmonary edema - a comparative study with wedge pressure and extravascular lung water. *Chest* **127**, 1690–1695 (2005).

[76] Fenster, A., Downey, D. B. & Cardinal, H. N. Three-dimensional ultrasound imaging. *Physics in Medicine and Biology* **46**, 67–99 (2001).

[77] Gamelin, J. *et al.* Curved array photoacoustic tomographic system for small animal imaging. *Journal of Biomedical Optics* **13**, 024007 (2008).

[78] Cornejo, L. A., Jadidian, B., Winder, A. A. & Safari, A. Large-area flexible-array piezoelectric ceramic/polymer composite transducer for bone healing acceleration. In *Proceedings of the Eleventh IEEE International Symposium on Applications of Ferroelectrics*, 259–263 (IEEE, 1998).

[79] Clement, G. T., White, J. & Hynynen, K. Investigation of a large-area phased array for focused ultrasound surgery through the skull. *Physics in Medicine and Biology* **45**, 1071–1083 (2000).

[80] Howe, B. M. *et al.* A smart sensor web for ocean observation: fixed and mobile platforms, integrated acoustics, satellites, and predictive modeling. *IEEE Journal of Selected Topics in Earth Observations and Remote Sensing* **3**, 507–521 (2010).

[81] Fukada, E. History and recent progress in piezoelectric polymers. *IEEE transactions on ultrasonics, ferroelectrics, and frequency control* **47**, 1277–1290 (2000).

[82] Oralkan, O. *et al.* Capacitive micromachined ultrasonic transducers: next-generation arrays for acoustic imaging? *IEEE Transactions on Ultrasonics, Ferroelectrics and Frequency Control* **49**, 1596–1610 (2002).

[83] Chen, J. Capacitive micromachined ultrasonic transducer arrays for minimally invasive medical ultrasound. *J. Micromech. Microeng.* **20**, 023001 (2010).

[84] Rodgers, D. M. *Directing acoustic radiation using a phased array of piezoelectric transmitters*. Ph.D. thesis, Massachusetts Institute of Technology, Dept. of Electrical Engineering and Computer Science (2010).

[85] Ghatak, A. *Optics* (Tata McGraw-Hill Education, New Delhi, India, 2005).

[86] Feynman, R. P. There's plenty of room at the bottom. *Engineering and Science* **23**, 22–36 (1960).

[87] Petersen, K. Silicon as a mechanical material. *Proceedings of the IEEE* **70**, 420–457 (1982).

[88] Liu, C. *Foundations of MEMS (Second Edition)* (Prentice Hall, Upper Saddle River, NJ, 2012).

[89] Egusa, S. *et al.* Multimaterial piezoelectric fibres. *Nature Materials* **9**, 643–648 (2010).

[90] Chocat, N. *et al.* Piezoelectric fibers for conformal acoustics. *Advanced Materials* n/a–n/a (2012).

[91] Zhang, Q. M., Bharti, V. & Zhao, X. Giant electrostriction and relaxor ferroelectric behavior in Electron-Irradiated poly(vinylidene fluoride-trifluoroethylene) copolymer. *Science* **280**, 2101–2104 (1998).

[92] Tashiro, K. *Ferroelectric polymers* (Marcel Dekker, New York, 1995).

[93] Xu, H. S. *et al.* Ferroelectric and electromechanical properties of poly(vinylidene-fluoride–trifluoroethylene–chlorotrifluoroethylene) terpolymer. *Applied Physics Letters* **78**, 2360–2362 (2001).

[94] Xia, F. *et al.* High electromechanical responses in a poly(vinylidene fluoride-trifluoroethylene-chlorofluoroethylene) terpolymer. *Advanced Materials* **14**, 1574–1577 (2002).

[95] Bauer, F. Review on the properties of the ferrorelaxor polymers and some new recent developments. *Applied Physics A: Materials Science & Processing* **107**, 567–573 (2012).

[96] Bauer, F., Fousson, E. & Zhang, Q. M. Recent advances in highly electrostrictive p(vdf-trfe-cfe) terpolymers. *IEEE Transactions on Dielectrics and Electrical Insulation* **13**, 1149–1154 (2006).

[97] Bao, H. M. *et al.* Phase transitions and ferroelectric relaxor behavior in P(VDFTrFECFE) terpolymers. *Macromolecules* **40**, 2371–2379 (2007).

[98] Agronin, A., Rosenwaks, Y. & G.I, R. Piezoelectric coefficient measurements in ferroelectric single crystals using high voltage atomic force microscopy. *Nano Letters* **3**, 169–171 (2003).

[99] Jeong, D. Y., Ye, Y. H. & Zhang, Q. M. Electrical tunable fabry-perot interferometer using a poly(vinylidene fluoride-trifluoroethylene-chlorofluoroethylene) terpolymer. *Applied Physics Letters* **85**, 4857–4859 (2004).

[100] Benoit, G., Hart, S. D., Temelkuran, B., Joannopoulos, J. D. & Fink, Y. Static and dynamic properties of optical microcavities in photonic bandgap yarns. *Advanced Materials* **15**, 2053 (2003).

[101] Joannopoulos, J. D., Johnson, S. G., Winn, J. N. & Meade, R. D. *Photonic Crystals: Molding the Flow of Light (Second Edition)* (Princeton University Press, 2008).

[102] Yeh, P., Yariv, A. & Marom, E. Theory of bragg fiber. *J. Opt. Soc. Am.* **68**, 1196–1201 (1978).

[103] Fink, Y. *et al.* A dielectric omnidirectional reflector. *Science* **282**, 1679–1682 (1998).

[104] Temelkuran, B., Thomas, E. L., Joannopoulos, J. D. & Fink, Y. Low-loss infrared dielectric material system for broadband dual-range omnidirectional reflectivity. *Optics Letters* **26**, 1370–1372 (2001).

[105] Kuriki, K. *et al.* Hollow multilayer photonic bandgap fibers for nir applications. *Optics Express* **12**, 1510–1517 (2004).

[106] Ruff, Z. *et al.* Polymer-composite fibers for transmitting high peak power pulses at 1.55 microns. *Opt. Express* **18**, 15697–15703 (2010).

[107] Yeh, P. *Optical Waves in Layered Media*. Wiley Series in Pure and Applied Optics Series (Wiley, John & Sons, Inc., 2005).

[108] Cheng, Z. Y. *et al.* Electrostrictive poly(vinylidene fluoride-trifluoroethylene) copolymers. *Sensors and Actuators A* **90**, 138–147 (2001).

[109] Ren, K., Liu, S., Lin, M., Wang, Y. & Zhang, Q. M. A compact electroactive polymer actuator suitable for refreshable braille display. *Sensors and Actuators A* **143**, 335 (2008).

[110] Sun, Z. & Lin, Q. Study of a fabry–pérot-like microcavity with sandwiched metallic gratings for tunable filter arrays. *IEEE Photonics Technology Letters* **20**, 1157–1159 (2008).

[111] Zhu, H., Pruvost, S., Cottinet, P. J. & Guyomar, D. Energy harvesting by non-linear capacitance variation for a relaxor ferroelectric poly(vinylidene fluoride-trifluoroethylene-chlorofluoroethylene) terpolymer. *Applied Physics Letters* **98**, 222901 (2011).

[112] Lallart, M., Cottinet, P.-J., Guyomar, D. & Lebrun, L. Electrostrictive polymers for mechanical energy harvesting. *Journal of Polymer Science Part B: Polymer Physics* **50**, 523–535 (2012).

[113] Xia, F., Tadigadapa, S. & Zhang, Q. M. Electroactive polymer based microfluidic pump. *Sensors and Actuators A* **125**, 346–352 (2006).

[114] SPIE Photonics West. *Liquid-filled varifocal lens on a chip.*

[115] Akdogan, E. K., Allahverdi, M. & Safari, A. Piezoelectric composites for sensor and actuator applications. *IEEE Transactions on Ultrasonics, Ferroelectrics and Frequency Control* **52**, 746–775 (2005).

[116] Gruverman, A., Auciello, O. & Tokumoto, H. Scanning force microscopy for the study of domain structure in ferroelectric thin films. *Journal of vacuum science and technology B* **14**, 602–605 (1996).

[117] Rodriguez, B. J., Jesse, S., Kim, J., Ducharme, S. & Kalinin, S. V. Local probing of relaxation time distributions in ferroelectric polymer nanomesas: time-resolved piezoresponse force spectroscopy and spectroscopic imaging. *Applied Physics Letters* **92**, 232903 (2008).

[118] Neese, B. *et al.* Large electrocaloric effect in ferroelectric polymers near room temperature. *Science* **321**, 821 –823 (2008).

[119] Neese, B., Lu, S. G., Chu, B. & Zhang, Q. M. Electrocaloric effect of the relaxor ferroelectric poly(vinylidene fluoride-trifluoroethylene-chlorofluoroethylene) terpolymer. *Applied Physics Letters* **94**, 042910 (2009).

[120] Wang, Y., Zhou, X., Chen, Q., Chu, B. & Zhang, Q. Recent development of high energy density polymers for dielectric capacitors. *IEEE Transactions on Dielectrics and Electrical Insulation* **17**, 1036–1042 (2010).

[121] Chu, B. *et al.* A dielectric polymer with high electric energy density and fast discharge speed. *Science* **313**, 334–336 (2006).

[122] Gu, J. F., Gorgutsa, S. & Skorobogatiy, M. Soft capacitor fibers using conductive polymers for electronic textiles. *Smart Materials & Structures* **19** (2010).